TECHNISCHE UNIVERSITÄT WIEN
Vienna University of Technology

ATOMINSTITUT

Dissertation

Imaging with Ion Beams at MedAustron

Ausgeführt zum Zweck der Erlangung des akademischen Grades eines Doktors der technischen Wissenschaften (Dr. techn.)

unter der Leitung von

Assistant Prof. Dipl.-Ing. Dr.techn. Albert Hirtl
Atominstitut
Stadionallee 2, 1020 Wien, Österreich

durch

Dipl.-Ing. Alexander Burker
Mat.Nr.: 00826360

eingereicht an der TU Wien, Fakultät für Physik

Wien, 2022

Unterschrift Betreuer

Unterschrift Student

Acknowledgements

A significant proportion of my dissertation related to the newly formed research group for applied particle physics and detector technology at the MedAustron facility, which was started in 2017 as a collaboration between MedAustron, the Institute of High Energy Physics and the Vienna University of Technology. One of the group's major projects was the commissioning of a demonstrator for ion imaging at the site, to which I started to contribute early on. I would like to thank the other members – my supervisor Albert Hirtl, Thomas Bergauer, Christian Irmler, Stefanie Kaser, Florian Pitters and Felix Ulrich-Pur – of this research group for setting their minds to and working towards this goal.

The detector systems – sensors and their readout system – were not just provided by the Institute of High Energy Physics but detector modules were also assembled and tested by technicians from by the institute. I therefore want to acknowledge the people who made the measurements possible in the first place: Andreas Bauer, Thomas Bergauer, Klaus-Dieter Fischer, Christian Irmler, Stefan Schultschik, Helmut Steininger, Richard Thalmeier and Hao Yin.

I am deeply grateful to Christian Irmler, Felix Ulrich-Pur and Hao Yin for their unabated help in carrying out the beamtests either in person or through their remote availability.

At the beginning of this project the beam had a high rate unsuitable for single particle tracking without pile-up. It was necessary to work together with accelerator physicists to produce additional extraction parameters for a beam with a lower rate. I want to thank Andrea De Franco, Greta Guidoboni, Sebastian Nowak, Dale Prokopovich and Claus Schmitzer. I would like to extend my thanks to Matthias Kronberger and Thomas Schneider for managing the relationship between MedAustron and our research group, as well as Hermann Fuchs and Peter Kuess for helping around within the facility and its detectors.

Regarding Monte-Carlo simulations I would like to acknowledge the research group for discussing the system parameters and the presentation of results. I want to thank Florian Pitters in particular for his insightful comments and suggestions at every stage of development.

Zusammenfassung

Eine Forschungsgruppe für Bildgebung mit Ionenstrahlen wurde am MedAustron, Zentrum für Ionentherapie und Forschung, gegründet. Als Teil dieses Projektes wurde ein Demonstratorsystem zusammengesetzt um einen Arbeitsfluss für Messungen und Bildrekonstruktion aufzubauen. Diese Dissertation behandelt Messungen mit dem Demonstrator und begleitende Monte-Carlo-Simulationen um die technischen Voraussetzungen für ein vorklinisches System zu untersuchen.

Der Demonstrator wurde aus doppelseitigen Silizium-Streifendetektoren für Spurmessungen und einem Reichweitenteleskop zusammengesetzt. Er wurde für die Messung eines Datensatzes von Einzelteilchen, die ein metallisches Stufenphantom durchquerten, genutzt. Spurrekonstruktion, Justierung der Detektoren und eine vorläufige Bildrekonstruktion wurden durchgeführt. Insgesamt 79 verschiedene Phantomrotationen wurden mit Vielfachstreuung, Energieverlust und Intensitätsverlusten projiziert. Rekonstruktionen wurden mit Streuung und Energieverlust erzeugt, allerdings aufgrund von Artefakten nicht mit Intensitätsverlusten.

Monte-Carlo-Simulationen wurden durchgeführt um die Unbestimmtheit der wahrscheinlichsten Teilchenpfade durch ein Wasserphantom zu untersuchen, welche mit Detektormessungen ausserhalb des Phantoms modelliert wurden. Die intrinsische Bildauflösung innerhalb des Phantoms mit der Differenz aus einzelnen modellierten und korrekten Pfaden bestimmt. Simulationen wurden mit verschiedenen Systemparametern (z.B. Positionsauflösung, Strahlenergie oder Phantomdicke) wiederholt um den Einfluss der Parameter auf die Auflösung zu bestimmen. Außerdem wurde der Einfluss zusätzlicher (redundanter) Detektoren untersucht.

Eine Übersicht der Bildauflösung als Funktion der Systemparameter wurde mit Simulationen erstellt. Diese wurde genutzt um Intervalle von Detektordicke und Positionsauflösung zu ermitteln, die für Ionenbildebung geeignet sind: eine Positionsauflösung kleiner als 150 µm und eine Dicke unterhalb von 0.75 % Strahlungslängen. Zusätzliche Detektoren reduzierten die Bildauflösung aufgrund von Vielfachstreuung. Diesem Nachteil konnte teilweise entgegengewirkt werden, indem das general broken lines Modell statt geraden Spuren in Luft und den Detektoren genutzt wurde. Redundante Detektoren könnten also eingesetzt werden, ohne dabei die Bildauflösung zu verschlechtern.

Abstract

A research group for ion imaging was founded at the MedAustron facility for ion therapy and research, to develop a new and innovative ion imaging system. As part of this project, a demonstrator system was assembled to establish a workflow for measurements and image reconstruction. This work discusses measurements with the demonstrator and accompanying Monte Carlo simulations to study the technical requirements for an upcoming preclinical system.

The demonstrator consisted of double sided silicon strip detectors for tracking, and a range telescope for the residual range measurement. It was used to record individual particles passing through a small metallic stair phantom, to obtain a dataset suitable for image reconstruction. Track fitting, detector alignment and preliminary imaging was carried out with the dataset. Projection images based on multiple scattering, energy loss and beam attenuation were obtained at 79 phantom rotation angles. Tomographic reconstructions were produced for scattering and energy loss, but not for attenuation due to noise and artifacts in the projections.

Monte Carlo simulations were used to study the uncertainty of the most likely particle paths within a water phantom, modelled from detector measurements surrounding it. The intrinsic image resolution in the phantom was evaluated from the differences of individual modelled and correct paths. Simulations were repeated while iterating through many system parameters – such as position resolution, beam energy or phantom thickness – to study the impact of these parameters on image resolution. Additionally, the influence of additional (redundant) detector planes was studied.

An overview of the image resolution – as function of the parameter space of single tracking systems – was created with these simulations. It was used to identify intervals of detector thickness and position resolution that would facilitate a minimum image resolution of 2.5 lp/cm: a position resolution below 150 µm and a material budget of less than 0.75 % in terms of radiation length. Additional planes reduced the image resolution due to multiple scattering in the detectors. These detrimental effects could be partially counteracted by using the general broken lines model instead of straight lines for tracks in air and the detectors. Redundant planes could therefore be used without significantly reducing image resolution.

Contents

List of Figures

List of Tables

1 Introduction

The research field of ion imaging was established in the second half of the twentieth century, after the initial proposition for using protons in the 1960s [1] and some pioneering experiments with proton radiography [2–5], proton tomography [6–9], and imaging based on heavy ions [10–12]. Although ion imaging was surpassed as a diagnostic tool by x-ray computed tomography (CT), interest has picked up in recent years due to the increasing availability of high energy particle beams in facilities for external beam radiotherapy. Several modern prototypes for ion imaging were built and have been used to reconstruct medical phantoms [13–19].

For imaging, protons and heavy ions facilitate several advantages over x-rays. Higher contrast images can be obtained with protons and heavy ions than with x-ray radiographs [3–5, 11, 12, 20]. At the same time, ion imaging scans applied less dose to a patient than comparable x-ray images due to favourable dose deposition characteristics [7, 8, 10, 20]. The main drawback of using charged particles is that they suffer from multiple Coulomb scattering: frequent deflections of the particles as they pass through matter [21, 22]. These direction changes cause a reduced image resolution compared to an x-ray CT scan. Another advantage of x-ray CT over ion imaging is the increased cost of the latter, since ion imaging relies on particle accelerators to produce fast charged particles. Therefore, x-ray CT has been much more prevalent as a tool for medical imaging in the context of ion beam therapy.

Despite the downside in terms of a lower image resolution, ion imaging does remain a potentially lucrative candidate for improving the quality of ion therapy. Treatment planning in ion therapy relies on an accurate measurement of the spatial stopping power distribution in a patient, to convert the prescribed dose at a target depth to the initial energy of a particle beam capable of reaching that depth. Since ion imaging is not yet utilised as much as x-ray CT, the stopping power distributions are usually obtained through a stoichiometric calibration that is applied to x-ray CT images, thereby converting x-ray attenuation coefficients to stopping power [23]. This introduces ambiguities, since the same image value in an x-ray CT scan can be correlated with different stopping power values due to the chemical composition of different tissues [24]. Additionally, range uncertainties between 0.8 % to 3 % are introduced by the conversion [25–28].

Such conversion uncertainties would not be present in a direct measurement of the stopping power distribution, using an ion imaging system. Such a scanner would simply measure the energy loss as a function of the beam path through the patient and reconstruct the stopping power directly. Therefore, the range uncertainties and ambiguities due to the conversion would not be present and the total range uncertainties of a treatment plan can be reduced [29]. A demonstrator system was therefore constructed and set up at the MedAustron facility for ion therapy and research [30] during the course of this work. Measurements with this demonstrator were used to collect a dataset of position measurements and energy losses of each particle. This dataset was reconstructed to obtain three-dimensional tomograms of small metallic stair phantoms based on multiple scattering, energy loss and attenuation.

Insights gained through the setup and operation of the demonstrator system will be used in an upcoming redesign for a new and innovative scanner, which should be suitable for preclinical studies. A comprehensive understanding of how system parameters influence the image quality of a scanner is required to qualify the technical specifications of a new scanner. Exploring the parameter space, taking into account various sensor thicknesses and position resolutions, is unfeasible with prototype systems. Technical requirements were therefore explored using Monte-Carlo simulations. A parameterised model set-up for single particle tracking was built and used to simulate the passage of particle beams through a water body under various combinations of system parameters, such as detector spacing, phantom thickness or beam energy. The uncertainty of particle positions within the phantom was studied and converted to a scanner's potential image resolution. An overview of achievable image resolutions as a function of these system parameters was obtained and used to delimit intervals in the parameter space that are suitable for ion imaging. This allowed to isolate hardware requirements for a new scanner, in terms of its position resolution and material budget.

Finally, scanners using two and three detectors per tracking stage were compared to demonstrate that detector redundancy can reduce detection inefficiencies without sacrificing image resolution. Additional detector planes could be beneficial when measurements are missing due to defects or a sensitive area with gaps. In a three detector system a missing hit could be tolerated, which could reduce the dose of a scan. At the same time, the additional plane introduces multiple scattering, worsening image resolution. It was demonstrated in this work, that the reduction in resolution can be mitigated in some cases, by using a track model that accounts for multiple scattering in air and the detectors.

2 Ion Imaging Background

2.1 Interactions of Charged Particles with Matter

Charged particles that traverse through matter interact with many atoms along their trajectory, altering the states of the projectiles and the target particles (figure 2.1). The most abundant interactions involve inelastic collisions with hull electrons – causing excitation of the electron or ionisation of the atom – and elastic scattering off the atomic nuclei, however, other mechanisms such as elastic scattering with hull electrons, deflection in the Coulomb field of the nuclei with emission of bremsstrahlung and (inelastic) nuclear reactions also play an important role [31–33].

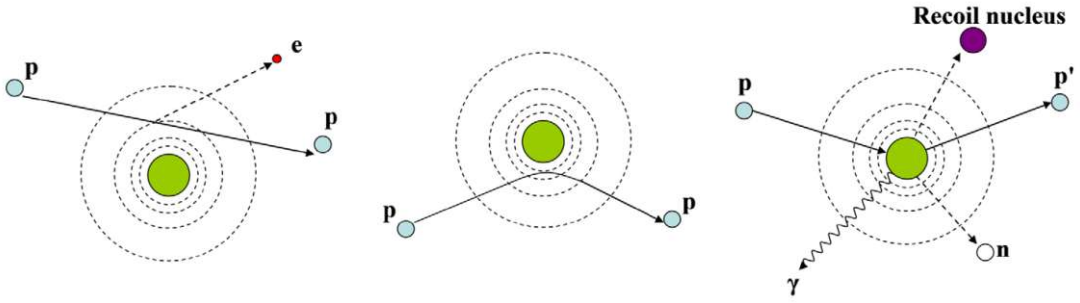

Figure 2.1: Several important interaction mechanisms of protons: (a) inelastic collisions with hull electrons, (b) elastic scattering off of a nucleus, and (c) inelastic nuclear interactions. Reproduced from Newhauser and Zhang [32].

Properties of the involved particles, such as energy and momentum, are changed due to these interactions. One consequence of frequent ionisations and excitations is that the projectiles continuously distribute their energy to the particles in the medium, with a low amount of energy at each interaction. This dissipation of energy reduces the velocity more and more as the beam reaches deeper into the medium, which further increases the rate of energy deposition (section 2.1.1).

Eventually the particles lose enough energy to completely stop at an energy-dependent depth, their range. Due to statistical fluctuations the individual particles are stopped at slightly different depths – a phenomenon that is called range straggling (section 2.1.2). Another consequence of the large amount of interactions is that the projectiles also frequently change their directions, thus creating highly nonlinear trajectories of the individual particles and a lateral widening of the beam as a whole (section 2.1.3). Lastly, some of the collisions can lead to nuclear interactions capable of fragmenting projectile (in case of ions) and target atoms. Such events continuously reduce the amount of primary particles with increasing penetration depth and can lead to a dose tail well after the primary beams range (section 2.1.4).

2.1.1 Energy Loss of Charged Particles

Particles typically used in ion therapy and imaging are protons and light ions, such as helium, carbon or neon, with energies in the range of 60 MeV/u to 600 MeV/u [31]. For these particles, the stopping power – i.e. the mean energy loss $\mathrm{d}E$ in a length $\mathrm{d}x$ – of a material can be modelled with the Bethe formula [33]

$$S(E) = \left\langle -\frac{\mathrm{d}E}{\mathrm{d}x} \right\rangle = K z^2 \frac{Z}{A} \frac{1}{\beta^2} \left[\ln\left(\frac{2 m_e c^2 \beta^2}{I \cdot (1-\beta^2)} \right) - \beta^2 - \frac{C}{Z} - \frac{\delta(\beta\gamma)}{2} \right], \tag{2.1}$$

using the charge number z of a projectile, the atomic number Z of a target, the atomic mass A of a target, the ratio of velocity and speed of light β of the projectile, the electron mass $m_e c^2$ in MeV and the mean excitation energy I of the target material. The coefficient $K = 4\pi N_\mathrm{A} r_e^2 m_e c^2 = 0.307\,075\,\mathrm{MeV\,cm^2/mol}$ is calculated with Avogadro's number N_A, the classical electron radius r_e and the electron mass. It should be noted that equation (2.1) is given with an implicit approximation for the maximum energy transfer in a single collision, which is valid at energies low enough so that $2\gamma m_e \ll M$ [33], and reads

$$W_\mathrm{max} = \frac{2 m_e c^2 \beta^2 \gamma^2}{1 + 2\gamma m_e / M + (m_e/M)^2} \approx 2 m_e c^2 \beta^2 \gamma^2. \tag{2.2}$$

Energy loss in a single collision is small compared to the initial energy, and most interactions transfer less than 100 eV [33].

Two terms in equation (2.1) are correction terms to the original Bethe formula [35], namely the density correction term $\delta(\beta\gamma)/2$ and the shell correction term C/Z.

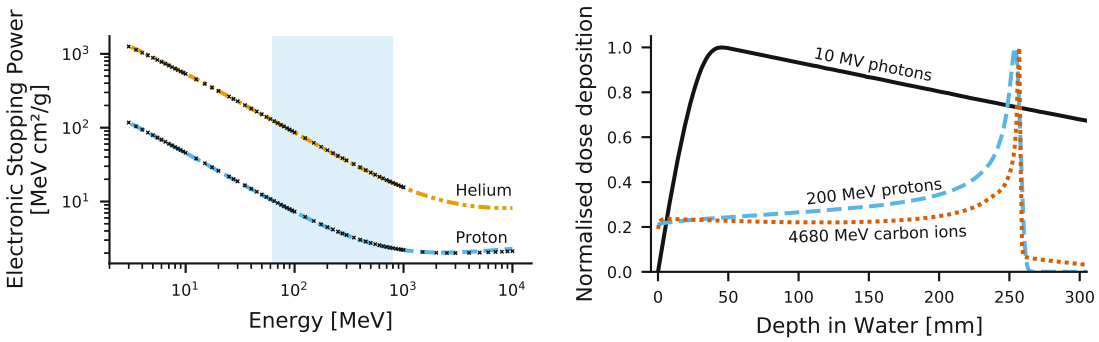

(a) (b)

Figure 2.2: (a) Electronic stopping power of protons and helium ions in water. The shaded area indicates the available proton energy range at the MedAustron facility. Crosses represent NIST data [34]. (b) Depth dependent dose distribution of photons, protons and carbon ions in water.

The density correction additionally considers polarisation effects of the target material at high projectile energies and the shell correction rectifies the assumption that the projectile velocity is much larger than the velocity of bound electrons in the target, which is invalid at low energies [36]. Grimes et al. [37] demonstrated that the correction terms can be neglected safely in the energy range of ion therapy and imaging, since the expected order of magnitude of the correction terms is below 1 %. Indeed, it is simple to visualise the small differences by setting both correction terms to 0 and comparing the graphs to tabulated stopping power values from the *ASTAR* and *PSTAR* programs [34] (figure 2.2a).

The stopping power decreases with increasing energy in the energy range typically employed for ion imaging. Besides ionisation and atomic excitation, additional radiative effects become relevant at higher energies. Due to this, energy loss starts to increase after a distinct minimum ionisation energy that depends on the material and projectile [33]. For particles traversing a medium, such as a proton beam in a water target, the continuous energy loss leads to an increase in energy loss further into the target. The depth-dependent dose distribution therefore features three distinct regions in depth: an initial plateau, where dose slowly rises with depth, followed by a sharp *Bragg* peak and a steep falloff (figure 2.2b). No dose is applied after the falloff for protons, however a dose tail is still present for heavy ion beams since these particles can fragment into lighter ions with an increased range (see section 2.1.4).

These regions can be utilised in a scenario where external beams are used on a patient to apply dose to a treatment area, such as a tumour. The ratio of dose to target and to healthy tissue is more optimal for charged particles, since the relative

dose leading up the the Bragg peak is lower and almost no dose is present after it [38]. This can also be exploited in ion imaging, where the beam completely passes through a patient in the plateau region and terminates with the Bragg peak in a detector [7, 8, 10, 20].

2.1.2 Range and Range Straggling

Beam particles are continuously slowed down in a medium due to the many energy losses along the way. At some point their energy is reduced enough to stop the particles. Many particles are stopped at a similar depth – called range – within the target. This range R can be estimated by integrating the stopping power from its initial energy to zero, which is often referred to as continuous slowing down approximation (CSDA) range [39]

$$R = \int_{E_0}^{0} \frac{1}{S(E)} \mathrm{d}E, \tag{2.3}$$

where $S(E)$ is the stopping power from equation (2.1) and E_0 is the initial energy of the particle.

Individual particles don't necessary stop at the same depth, since energy loss is a random variable that differs among particles due to the large number of interactions, however, a large amount will end up close to the range. The spread around the mean range is called range straggling and it depends on several variables, such as the particle species and initial energy, as well as the material traversed [38, 40]. As an example, heavier particles such as carbon ions have a narrower range distribution than protons (figure 2.3a) due to their larger mass [31].

CSDA ranges of protons and helium ions can be obtained from the *PSTAR* and *ASTAR* programs [34], respectively. These two particles have the same CSDA range in the energy range interesting for ion imaging, since the range scales with A/Z^2, with mass number A and atomic number Z [31], though small differences occur below 1 MeV (figure 2.3b).

Beams of protons or heavy ions are particularly useful in ion therapy and imaging because the range of such a beam is a function of its initial energy. This is exploited in therapy, where dose is applied to a target volume by varying the beam energy to reach different depths of tissue while deflecting the beam with magnetic fields such that it covers the volume perpendicular to the beam direction [31]. Ion imaging on the other hand needs to keep range in mind, to ensure that the beam fully penetrates the object to be imaged and terminates in a detector.

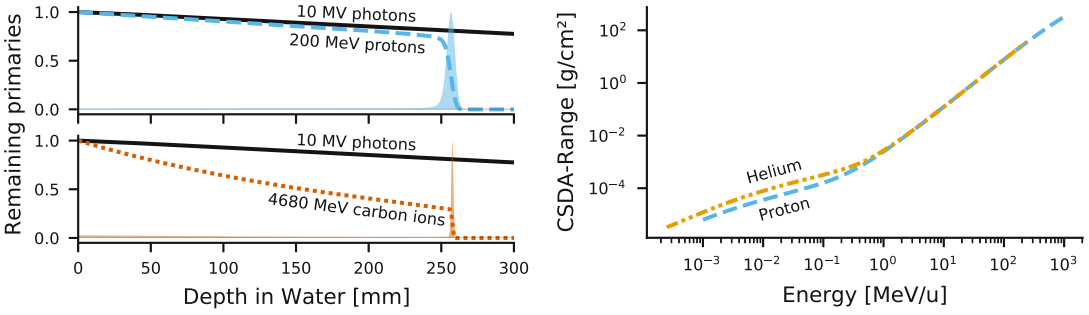

(a) (b)

Figure 2.3: (a) Proportion of remaining primaries (dashed and dotted lines) and loss of primaries (shaded areas) as function of depth in water, for photons, protons and carbon ions. A large amount of charged particles stops at a characteristic and energy dependent depth. (b) The continuous slowing down approximation (CSDA) range of protons and helium ions in water. Visualisation of NIST data [34].

2.1.3 Scattering

Particles that traverse a target frequently scatter off of the atoms making up the material, which changes the projectiles' momentum directions by a small amount at each collision. For charged particles in particular, these deflections are caused by interactions with the Coulomb field of target nuclei. The distribution of scattering angles was accurately modelled by Molière [21, 22]; it is centered around zero and widens depending on beam energy, particle species, material thickness and the radiation length of the target. For example, the kink angle distribution – the angle between individual particles trajectories upstream and downstream of a scattering body – of 200 MeV protons in a 300 µm thick silicon target is wider than the same distribution for an air target.

As can be seen in figure 2.4, the central part can be approximated by a normal distribution, though this approximation does not properly describe large angle deflections [22]. For large targets such as in ion imaging, the normal distribution is accurate for the innermost 98 % of tracks. It is therefore often used instead of the complete model, because doing so allows to conveniently calculate the width of the scattering angle distribution after passing through a material with a thickness x, with few parameters [41]

$$\langle\theta\rangle^2 = \frac{13.6\ \text{MeV}}{\beta c p} z \sqrt{\frac{x}{X_0}} \left[1 + 0.038 \ln\left(\frac{x}{X_0}\right)\right], \tag{2.4}$$

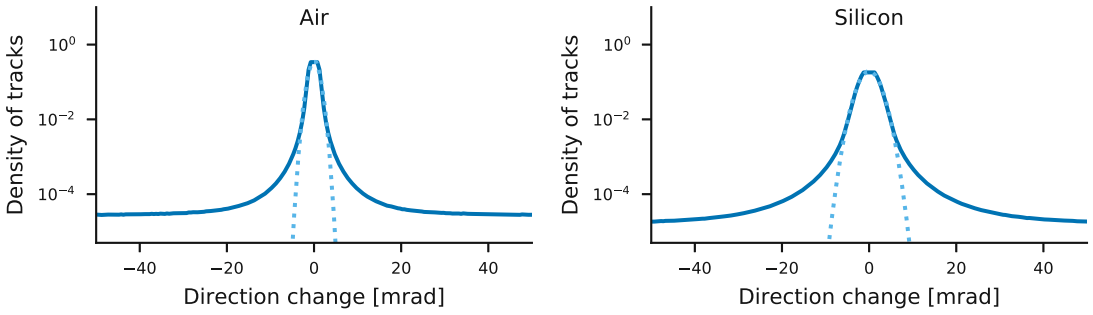

(a) (b)

Figure 2.4: Scatter angle distributions in (a) air and 300 µm (b) silicon for a 200 MeV proton beam. Normal distributions were fitted to the histograms (dotted lines): these accurately model the central 98 % but fail to take large angle scatter events into account.

using (βc), p and z as the velocity, momentum and charge of the beam particle, respectively. The radiation length X_0 is a target material property for which tabulated values are available [33, 42].

A core concept in ion imaging – the most likely path (MLP) of ions in matter introduced in section 2.3.2 – is also built around the central normal distribution approximation. Due to this, tracks with a scattering angle beyond 3σ of the distribution of measured angles are usually removed to guarantee that the data from an ion imaging scanner is well described by the approximation [43].

Equation (2.4) is used under the assumption that the energy of a particle remains constant while passing through the material. In thick absorbers, like a patient in an ion imaging scan, this is not usually the case. Therefore, the energy loss must be additionally considered by introducing an integration [44]

$$\langle\theta\rangle^2 = \frac{13.6\ \text{MeV}}{c} z \sqrt{\frac{1}{X_0}} \left[1 + 0.038 \ln\left(\frac{x}{X_0}\right)\right] \left(\int_0^x \frac{\mathrm{d}x'}{\beta^2(x')p^2(x')}\right)^{\frac{1}{2}}. \tag{2.5}$$

2.1.4 Nuclear Interactions

Some of the beam particles undergo inelastic nuclear collisions as they progress through matter, which can lead to excitation, fusion, nuclear transmutation or target fragmentation. Projectile fragmentation also occurs if ions such as helium or carbon are used as beam particles instead of protons. Cross sections for nuclear reactions are much smaller than for interactions with the target atoms, and

therefore these processes occur less often. Nevertheless, a substantial number of nuclear collisions will occur in large targets such as a patient [31, 45].

Nuclear reactions reduce the intensity of primary particles in the beam, according to the Beer-Lambert law [46, 47]

$$\Phi = \Phi_0 \exp\left(-\int_l \kappa(\vec{r}, E)\mathrm{d}l\right), \tag{2.6}$$

where Φ is the fluence of primaries after passing through a length l, Φ_0 is the initial fluence and $\kappa(\vec{r}, E)$ is the distribution of inelastic nuclear cross sections as a function of position and energy along the particle paths. These fluence losses are visible in figure 2.3a: the intensity of a 200 MeV proton beam is reduced by ≈25.57 % before it is stopped beyond a depth of 245 mm. Similarly, the intensity of a 4680 MeV carbon ion beam is reduced by 70.13 % at a depth of 255 mm.

A consequence of such fluence losses is that the ratio of Bragg peak to entrance dose is reduced with increasing initial range; beams with higher initial energy distribute a larger fraction of dose in the entrance channel than close to the range, compared to lower energy beams. Additionally, secondary particles are built up and contribute to the depth-dose distribution (figure 2.5), with different behaviour depending on whether a projectile or target atom was fragmented. Target fragments have a short range and therefore deposit their dose locally, whereas projectile fragments continue with much of the velocity before the fragmentation. Because range scales with A/Z^2 these lighter ions can carry dose to depths that primary particles would not have reached. This is visible for helium ions in figure 2.5b, where a dose tail from secondaries remains even after the Bragg peak [31, 45].

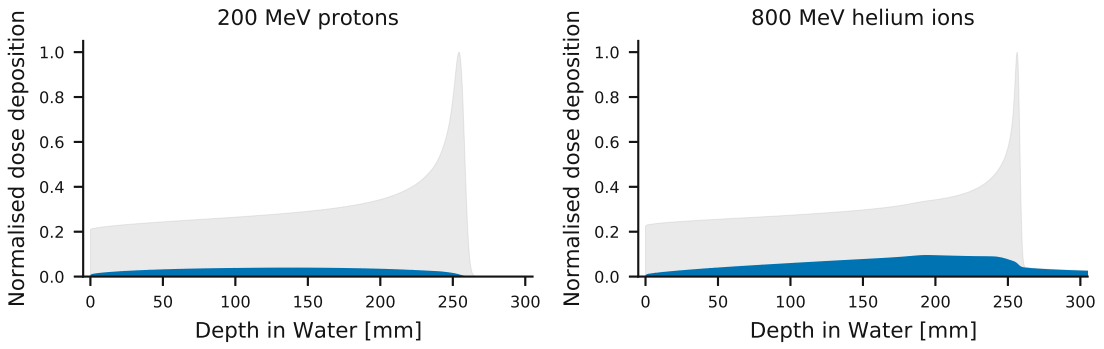

(a) (b)

Figure 2.5: Contribution of secondary particles (blue) to the total dose (grey) for (a) 200 MeV protons and (b) 800 MeV/u helium ions.

2.2 Particle Detection

Two different technologies were employed to detect beam particles and measure their properties with the demonstrator system: semiconductor detectors made of silicon (section 2.2.1), which were used to pinpoint particle positions as they passed through the two-dimensional detector planes, and plastic scintillators (section 2.2.2) that served as fast triggers on one hand and as a range telescope on the other.

2.2.1 Silicon Sensors

Semiconductor Physics

Many of the properties of silicon are a consequence of its diamond cubic crystal structure: two face-centered cubic lattices, shifted by $(a/4, a/4, a/4)$ with respect to each other, with a lattice spacing $a \approx 5.5\,\text{Å}$. The atoms are about half as densely arranged than in body-centered cubic metals and each atom has covalent bonds with four neighbours. Energy levels in individual atoms are split into many close levels that allow easy transitions due to the proximity of other atoms. Adjacent levels are therefore often referred to as energy bands [48, 49].

Electrical properties of solids depend on the band structure of their highest energy bands, which are usually named valence and conduction band. The valence band is the highest energy band with filled states if the temperature of the crystal was absolute zero. Electrons within this energy band form strong bonds with neighbouring atoms and do not conduct electric currents. Electrons in the conduction band however behave more freely: they can move around in the crystal and fill in empty states in the valence band (holes) of other atoms. The region between the energy bands is called a band gap, since there are no energy states available for electrons (figure 2.6). An energy greater than the band gap is therefore needed for an electron to enter the conduction band [48, 49].

In general, the size of the band gap groups materials into isolators, semiconductors and conductors. Isolators are characterised by a large band gap, so that thermal excitation is not enough to raise electrons to the conduction band. Therefore, these materials have almost no free electrons and poorly conduct electrical currents. Electrical conductors on the other hand are characterised by free moving electrons, due to either a very small band gap or overlapping energy bands. In between the two are semiconductors with an intermediate band gap. Some of their electrons are bound in the valence band, but they can be thermally excited and fill states in

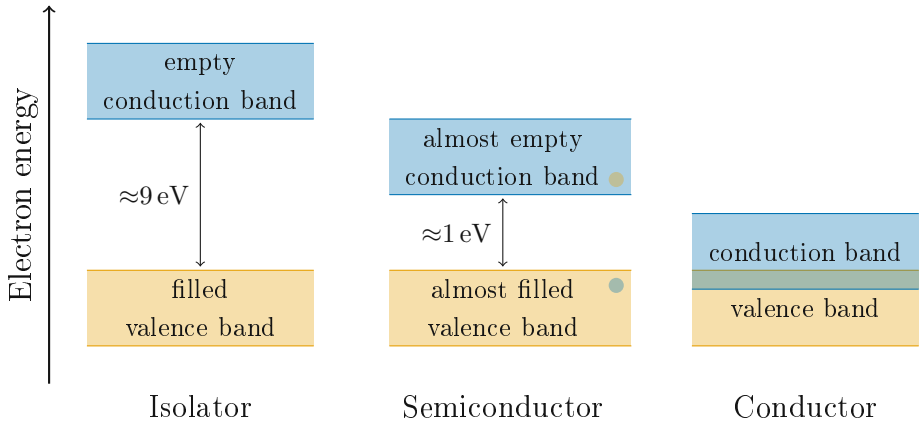

Figure 2.6: Simplified sketch of energy bands in solids. A large band gap separates the conduction and valence bands in isolators. This gap is much smaller for semiconductors; some charges are excited and fill states in the conduction band. Energy bands may overlap in conductive materials. Adapted from Lutz [48], Kolanoski and Wermes [49].

the conduction band, leaving holes in the valence band. The electrical properties of semiconductors change with temperature, external electrical fields or impurities in the lattice [48, 49].

Doping and the p-n Junction

The technique of deliberately introducing small amounts of impurities into the crystal lattice is called doping. In a silicon lattice, each atom has four valence electrons that couple with neighbouring atoms. Foreign atoms with five electrons, such as phosphorus or arsenic, can be added to increase the amount of free electrons in the material (n-doping). In the same way, three electron atoms such as boron or aluminium can be added to increase the amount of holes (p-doping). Both of these doping methods add charge carriers of one kind (electrons, holes) at the expense of the other. For example, the additional holes in p-doped silicon reduce the number of electrons in the conduction band [48, 49].

If two differently doped semiconductors are connected, they form a semiconductor junction (or p-n junction). Diffusion of charge carriers towards the junction occurs due to the different concentrations in both doped zones: electrons move towards the p-doped side and holes toward the n-doped side. Both charge carriers recombine in the middle of the junction, where a carrier free depletion zone is built up (figure 2.7). This recombination also ionises atoms in the depletion zone and thereby creates an electric field within it [48, 49].

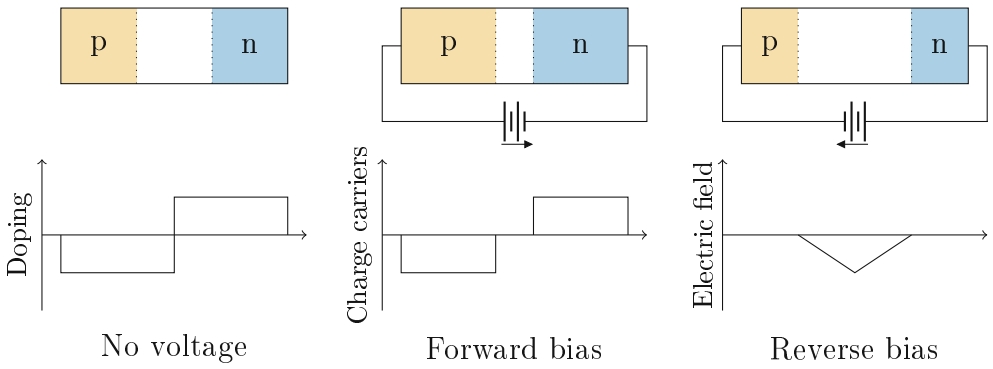

Figure 2.7: Semiconductor junction with different external voltages applied. A depletion zone without free charge carriers is formed at the junction. Silicon sensors are usually fully depleted (reverse bias). Adapted from Lutz [48] and Kolanoski and Wermes [49].

An external voltage applied to a semiconductor junction can be used to modify the size of the depletion zone. The polarity of the voltage determines whether the depletion zone is increased or decreased in size, relative to a junction without an external voltage, whereas the magnitude of the supplied voltage increases the growth or decline. Silicon sensors for particle detection are usually operated with a reverse bias: a positive potential connected to the n-doped zone, thus increasing the depletion zone. The material therefore has few available electrons or holes for electric currents. Beam particles that interact with a depleted silicon sensor deposit energy and create charge carriers, which then drift towards the electrodes due to the electric field. It is these drift currents that are measured and amplified in order to detect particle interactions [48, 49].

Double Sided Silicon Sensor

A double sided silicon strip detector (DSSD) is a flat, segmented diode that consists of a doped silicon bulk material with a thickness of a few hundred µm. Two sets of orthogonal strips are built into both of its sides, with different strip doping on the opposing sides (figure 2.8). Strips typically cover the full length of the sensor in one dimension and have a pitch (distance between strips) of a few tens of µm to a few hundred µm. Often, the bulk material is weakly n-doped (n^-), while strips are more strongly doped (p^+, n^+) than the bulk. The biasing voltage is larger than necessary to fully deplete the sensors, so that no free charges remain in the material. This also creates an electric field that separates charge carriers created by a beam particle, which then drift towards the electrodes [48, 49].

Each strip is an electrode, both for biasing the bulk and collecting charge carriers

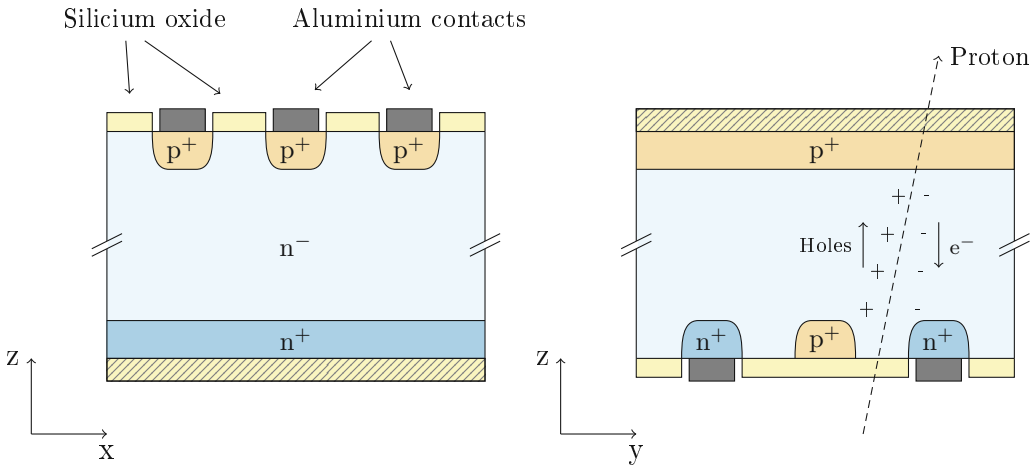

Figure 2.8: Particle detection with a double sided silicon strip detector. Orthogonal strips are located on both sides of the bulk material. Additional p-doped strips are necessary to isolate n-doped strips from each other in the n-doped bulk. Adapted from Lutz [48] and Kolanoski and Wermes [49].

from beam particle interactions. Neighbouring strips are capacitively coupled with each other, which allows to operate the detector with less readout channels than strips. To obtain a position measurement, each strip with a readout channel is amplified and read out separately. The position of an interaction is then calculated with the activated strip number and knowledge of the sensors pitch. In a simple comparison of each strip signal to a threshold, to decide whether a strip was hit or not, the position resolution σ_x^2 is approximately [48, 49]

$$\sigma_x^2 = \frac{1}{p}\int_{-p/2}^{p/2} x^2 \mathrm{d}x = \frac{p^2}{12}, \tag{2.7}$$

with the strip pitch p. A better resolution can be obtained by reading out the signal heights of each activated strip and calculating a center of gravity (see section 3.4.1), although this increases the amount of data to transfer (and therefore reduces the readout rate) [48, 49].

One peculiarity in DSSDs is that the n^+ side strips do not form a depletion zone with the n^- bulk. In a detector with only n^+ doped strips (and no additional structures on the n-side), this would create accumulations of free electrons at the surface to the silicon oxide and short circuit strips. Special structures – such as the intermediate p^+ strips in figure 2.8 – are therefore necessary to suppress this effect and isolate the n^+ strips from each other [48, 49].

2.2.2 Plastic Scintillators

Scintillating materials find frequent use in beam telescopes or ion imaging scanners, either for the generation of a fast trigger signals or for measuring properties of particles such as the residual energy (range) through a calorimeter (range telescope) or positions through scintillating fibres. The process of scintillation measurements starts with an interaction of a beam particle that causes the material it passed through to emit light. Emitted light is then converted into electrons or electron-hole pairs – depending on the detector – and amplified, so that an electric signal can be obtained [49–51].

Scintillation Light

Scintillation is light emission (fluorescence and phosphorescence) as a consequence of interactions between ionising radiation with matter. Light is emitted due to excitation and the return to a less energetic state or ionisation and recombination. Though several scintillator materials exist, such as organic and anorganic crystals, fluids, solutions and polymers (plastic scintillators), only the latter – specifically Polyvinyltoluene based plastic scintillators – were used in this work. In those materials, scintillation mainly depends on weakly bound electrons of carbon atoms and their neighbours such as those residing in delocalised π-orbitals. Instead of being associated with a strong covalent bond between two atoms, these electrons occupy a molecular orbital in molecules like ethylene or benzene [49–51].

Energy transfer due to an interaction with a beam particle excites such an electron from the singlet ground state (S_0) to an excited state ($S_1, S_2, \ldots$) or one of their corresponding vibrational modes ($S_{i1}, S_{i2}, \ldots$) of the molecule. A difference of several eV separates ground state and electron levels, whereas the vibrational modes on top of these states are elevated by a few tenths of eV. Three different transitions will usually occur following an excitation. Vibrational mode states decay within less than 10 ps to their corresponding electron levels without emitting radiation. In what is called fluorescence, electrons in the excited states are very likely to decay to the ground state or one of its vibrational modes within a few ns, releasing excess energy as light. Another (for scintillators unwanted) possibility is phosphorescence: a transition to a triplet state through a non-radiative process and a subsequent decay within a few ms [49–51].

The energy spectrum for absorption is slightly larger than the spectrum for emission (Stokes' law), because some of the excitations raise the energy level to a vibrational mode of an excited state, and some of the decays fall to a vibrational mode of the ground state. In both of these cases some of the energy is removed

from the scintillation process due to the fast non-radiative decays. Scintillators are partially transparent to their own light due to these energy losses, since such a photon no longer carries the energy necessary for an excitation. The overlap in the energy spectra is often artificially increased by adding wavelength shifters: supplementary scintillators with an absorption spectrum matched to the emission spectrum of the base material and an emission spectrum with a larger wavelength [49–51].

Electronic Readout

Photomultiplier tubes and silicon photomultipliers are commonly used to convert scintillation light to electrical signals for a readout. Figure 2.9 illustrates the working principle of a photomultiplier connected to a scintillator via a light guide. A photocathode converts scintillation light to primary electrons through the photoelectric effect. Several electrodes (called dynodes) are placed between the cathode and the anode, with a voltage difference between successive electrodes through the use of resistors. Due to the voltage differences, electrons are accelerated from one electrode to the next, where they arrive with enough kinetic energy such that secondary electrons are released. Therefore, the number of electrons in the photomultiplier increases exponentially with the number of dynodes, and amplification factors of 10^{8-9} can be realised. Finally, a signal proportional to the energy deposited in the scintillator can be measured as a voltage drop over a load resistor R_{L}, which is connected to the anode [49–51].

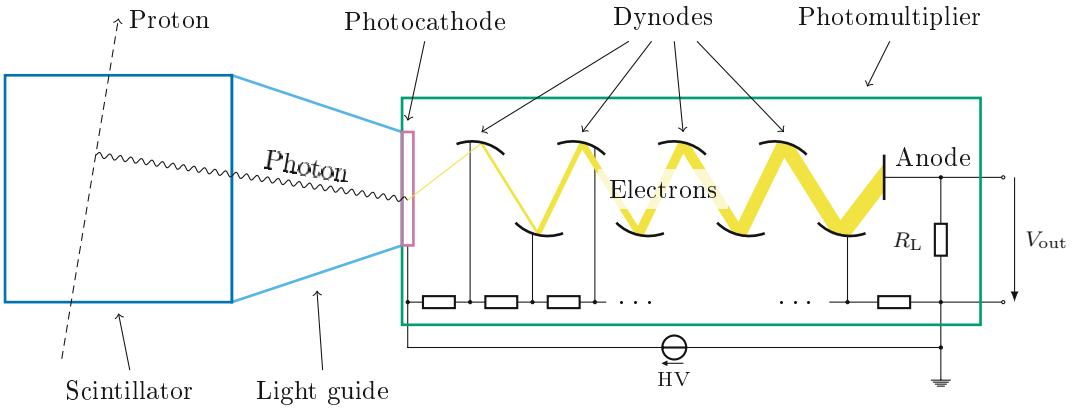

Figure 2.9: Sketch of a scintillator with light guide and photomultiplier tube. A photoelectron is accelerated from the cathode to a number of dynodes, where additional electrons are emitted, amplifying the signal.

Another technology used with scintillators is called silicon photomultiplier (SiPM),

which utilises avalanche photodiodes instead of dynodes to convert and amplify the scintillation light [52]. Simple photodiodes are semiconductor detectors with an undoped zone between a p-n junction that can be depleted by applying a voltage, allowing incoming photons to create electron-hole pairs within the zone. An advancement of the simple photodiode is the avalanche photodiode, which uses a large electric field to multiply photoelectrons and thereby additionally amplify the signal. The field in a silicon photomultiplier is created through highly doped p- and n-layers and a bias voltage that is ≈10 % to 20 % larger than the breakdown voltage. This operation is often referred to as Geiger mode, since it enables amplification factors in excess of 10^6 at the cost of needing to stop (quench) the discharge and a loss of linearity between input and output. Due to this operation mode, a single diode can only tell apart whether the sensor was hit by a photon or not. SiPMs are therefore made up of a large number of avalanche photodiodes arranged in a matrix, so that the number of diodes with a hit can be counted. Effectively, this arrangement allows to measure signals that are proportional to the amount of light in the scintillator, with a dynamic range that is limited by the number of pixels in a detector [49].

2.3 Ion Imaging

Ion imaging setups for tracking individual particles were used throughout this work. Several detectors measured positions along the trajectory as well as the residual energy, per particle (section 2.3.1). Position measurements were used to infer entry and exit positions on the surface of an object to be imaged and to model the path within this object (section 2.3.2). An imaging plane within the object was then subdivided into two dimensional pixels and each particle associated with the pixel that it passed through according to the modelled path. Two dimensional projection images of changes to particle properties, as a function of the location within the object, were created for three different quantities: energy loss, multiple scattering and attenuation (section 2.3.4).

2.3.1 Experimental Setup

The reference design for a single particle tracking system for proton computed tomography was discussed in Schulte et al. [53]. This work describes the composition of a generic system, using two tracking stages placed upstream and downstream of a target and a residual energy measurement at the terminal end of the beam (figure 2.10). Data from the tracking stages is used to derive the path through

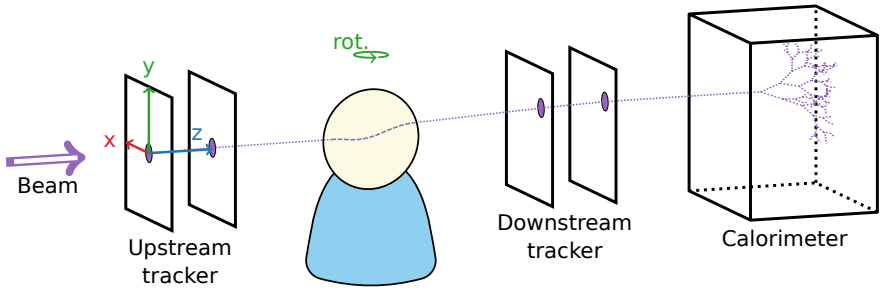

Figure 2.10: Sketch of ion imaging setup. Particles from an accelerator pass through an upstream tracker, an object to be imaged (patient or phantom), a downstream tracker and are stopped in a calorimeter. The tracking detectors record two dimensional positions to reconstruct particle paths through the object, and the calorimeter determines the residual energy.

the target and, combined with the energy measurement, to calculate the energy loss along this path. Several ion imaging systems have implemented this layout in simulations and hardware [13–15, 17, 18].

Tracking Stages

Each of the tracking stages is subdivided into a number of tracking planes that are able to produce a two-dimensional position measurement. Some systems realise these measurements with pixel detectors [17], while others split the two-dimensional positions into two (orthogonal) [14–16] or three (60° rotated) one-dimensional measurements using strip detectors [18, 54].

It is possible to determine the particle directions if more than one tracking plane is used in a tracking stage; or, for the upstream tracker, if additional information can be obtained from the beam delivery system of the particle accelerator. Whether a hypothetical new system should measure the direction or not is an important design choice, since its availability has a strong influence on the spatial resolution of the images that the system can produce [55, 56].

Residual Energy Measurement

Given an initial energy it is necessary to measure the residual energies of the tracked particles, so that the energy loss can be correlated with every particle's path. During image reconstruction the mean energy loss in each target volume element is then used to find the local (relative) stopping power (see section 2.3.4). Residual energy is determined by either directly measuring it in a homogeneous

or segmented calorimeter, or by converting another signal to energy, such as range from a range telescope, momentum from a magnetic spectrometer or velocity from a time-of-flight spectrometer.

Diverse methods and technologies have been employed in ion imaging to carry out these measurements. The most simple approach was a direct measurement of the residual energy using scintillators like a YAG:Ce crystal [15]. Energy depositions were also sampled with five stages of scintillators in the beam direction, to achieve better resolution over a range of different residual energies [57]. Other prototypes used more than 40 layers to find the residual range [16, 58] or even well over 60 that were additionally subdivided laterally, so that the location of the energy deposition could be determined too [17]. Besides scintillators, silicon strip and pixel detectors with absorber plates between them have also been used to build range telescopes for ion imaging [18, 19].

2.3.2 Path Reconstruction

Due to multiple Coulomb scattering (section 2.1.3) it is not possible to perfectly recreate particle trajectories [59]. Thus, the trajectory of each particle is approximated using sophisticated path models. Depending on whether the particle went through the target or through air only, either two or three path models are employed. At least two path models are used for the upstream and downstream trajectories in air and, if the particle passed through the target, a third model is used to connect those two. During the event reconstruction, path models in air are used to determine the upstream and downstream boundary conditions on the target surface, i.e. the positions and directions where the particles entered and exited the target. Afterwards the path within the phantom can be modelled based on the boundary conditions, so that the three models seamlessly connect to each other (see figure 2.11).

Reconstruction in Air

A track fit is performed on the position measurements of the two tracking stages. The simplest track model in air is a straight line in three-dimensional space. Both the upstream and downstream model need at least two position measurements for a reconstruction of the direction. Another model that is used in physics applications such as beam telescopes or large particle detectors is called general broken lines (GBL) [60]. This model requires at least three position measurements, but it can additionally take the expected amount of multiple Coulomb scattering in the

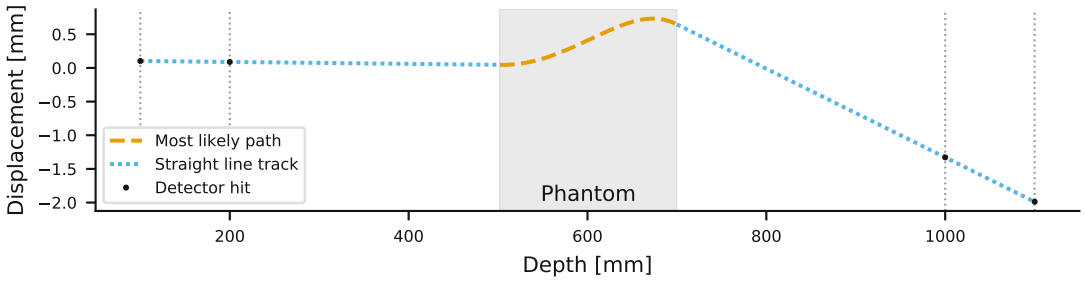

Figure 2.11: Connection of path models in ion imaging. Straight lines are fitted to the detector hits and the intercepts between those paths and the phantom surface are calculated. Then, the entry and exit positions and directions are used by the most likely path model to estimate the path within the phantom.

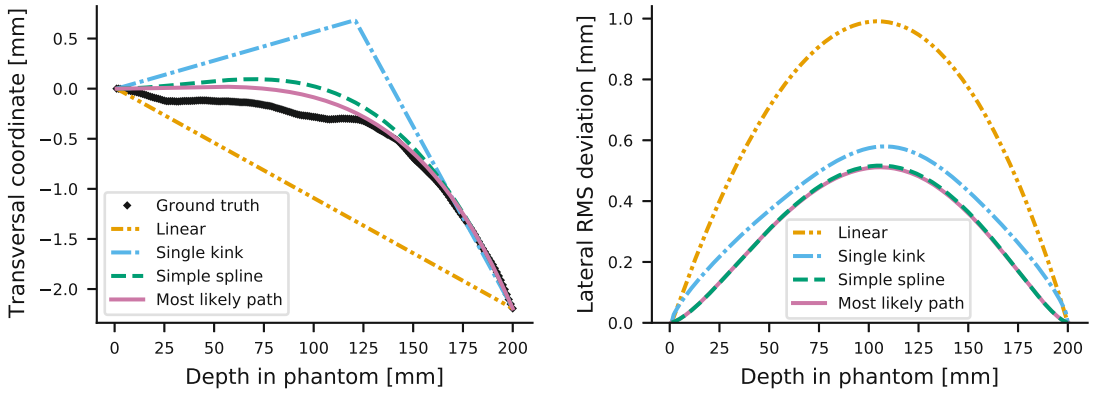

Figure 2.12: (a) Comparison of the x-coordinate of one simulated path through the phantom and several model estimates. (b) The lateral root-mean-square deviation (RMSD) of many simulated paths and their model estimates, for several path models.

detector planes into account. To do that, kink angles are allowed at the inner – i.e. not the first and last – detector planes within a tracking stage; with accepted angles calculated according to the central Gaussian approximation of multiple scattering (equation (2.4)).

Reconstruction in the Target

Several path models have been used to describe trajectories through a target in an ion imaging context, such as straight lines, two straight lines that meet at a single kink [61], cubic splines [62] and the MLP model [63]. A comparison of these models is visualised in figure 2.12a, for a single simulated particle trajectory. The

accuracy of each of these models can be estimated based on Monte Carlo simulation of many trajectories. Particles are recorded by sampling their positions as they move through a target. Then, by taking the first and last position and direction as input, each of the trajectories is estimated by the path model in question. The squared difference in simulated and estimated positions perpendicular to the beam direction is calculated and summed over many events, thus yielding the root-mean-square deviation (RMSD) (figure 2.12b); a depth-dependent measure for path uncertainty

$$\mathrm{RMSD} = \sqrt{\frac{\sum_{i=1}^{N} (\hat{x}_i - x_i)^2}{N}}, \tag{2.8}$$

where $\hat{x}_i$ and x_i are the estimated and true displacement of the i-th trajectory, respectively, and N is the number of events. Uncertainty increases from the surface towards the middle of the phantom, with a maximum slightly shifted towards the exit surface due to energy loss in the phantom. The overall bell shape of uncertainty envelopes is similar among different path models, since it is merely a consequence of missing measurements within the phantom. However, the heights of these curves and the location of their maxima differs. Using this method it can be verified that the MLP is the most accurate model, i.e. the model with lowest maximum and integral RMSD. Therefore it is currently considered to be the reference model for ion imaging [62, 64–66].

2.3.3 Spatial Resolution of an Image

An important quality factor of an imaging system is the spatial resolution of the images it produces, i.e. the lowest distance at which small details can still be differentiated. Detector systems produce images that are slightly blurry due to their nonzero spatial resolution, which originates from physical limitations such as multiple scattering and the sampling accuracy of measured signals. A step from one material to another will not produce a step function in a reconstructed image; instead, the profile across the step steadily changes from the signal of one material to the other (figure 2.13). The edge spread function (ESF) of a scanner describes how a step function within the scanned object is transformed in the reconstructed image. It is the two-dimensional Fourier transform of image values along a line that is orthogonal to the edge of the step function. The derivative of the ESF is the line spread function (LSF) of a scanner, which describes how a thin line (such as a slit) is transformed in the image. Like the ESF, the LSF is the two-dimensional Fourier transform of a line orthogonal to the line in the object [67].

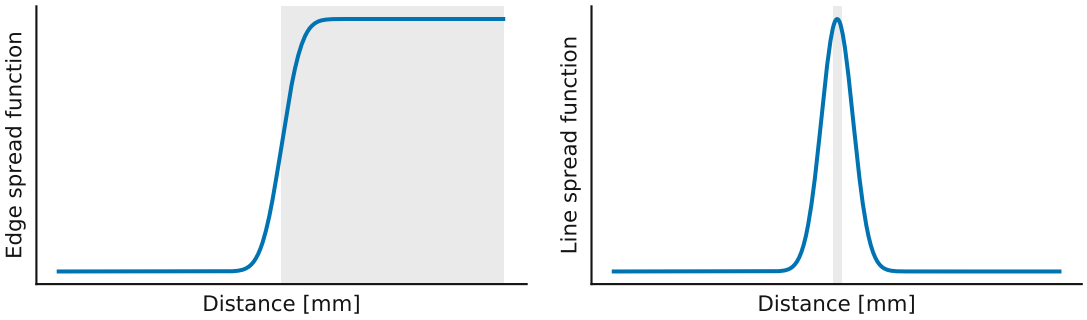

Figure 2.13: The edge spread function and line spread function.

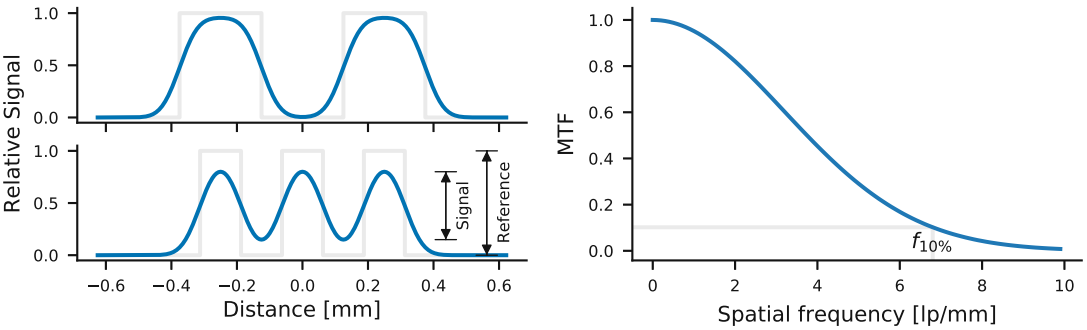

(a) (b)

Figure 2.14: (a) Reconstructed line pair profiles of two and three line pairs. (b) The modulation transfer function (MTF).

Either of these functions can be measured to estimate the spatial resolution of a scanner, using specialised phantoms with material inserts such as line pairs for a step function or slits for a thin line. A common approach is to use a phantom with several sets of line pairs (lp) with an increasing spatial frequency (lp/mm) [56, 62, 64, 68–70]. The ESFs of the individual steps begin to overlap at increased frequencies which reduces the signal size in the image, when compared to reference values. Additionally, the local minima between the line inserts are elevated (figure 2.14a). At some point, the overlapping ESF merge so that the separate peaks cannot be resolved any more [67].

The reduction of the ratio of signal to references values is summarised in the modulation transfer function (MTF), defined as

$$\mathrm{MTF}(f) = \frac{s_{\max}(f) - s_{\min}(f)}{S_{\max} - S_{\min}}, \tag{2.9}$$

where $s_{\max}(f)$ and $s_{\min}(f)$ are the local maximum and minimum of the signals, respectively, which can be measured. $S_{\max}$ and $S_{\min}$ are the reference values of the phantom materials used for the line pairs. Often, the spatial frequency $f_{10\%}$ at which the MTF falls below 0.1 (figure 2.14b) is used to qualify the spatial resolution of a scanner [67].

2.3.4 Imaging Modalities

A big motivation for ion imaging is the ability to directly measure stopping power distributions in a patient for improving treatment planning in particle therapy. Besides the energy loss, other quantities such as the amount of multiple scattering and the attenuation of the beam can be measured as well. The same data from an ion imaging scanner are suitable to reconstruct relative stopping power (RSP), relative radiation length and macroscopic nuclear cross-section distributions of an object that was imaged [46, 47, 71–73].

Relative Stopping Power

The RSP reconstruction problem is obtained by reordering equation (2.1)

$$-\mathrm{d}E = S\left(\vec{\Gamma}(l), E(\vec{\Gamma}(l))\right)\mathrm{d}\vec{\Gamma}(l), \tag{2.10}$$

where $\vec{\Gamma}(l)$ is the curved path of a particle, l the length along this path and $E(\vec{\Gamma}(l))$ the energy of a particle at each position along this path. The equation is divided by the stopping power of water ($S_{\mathrm{H_2O}}$) on both sides to introduce the RSP on the right side, which is less dependent on beam energy (see figure 2.15) [46, 71, 72, 74]

$$\mathrm{RSP}(\vec{\Gamma}(l)) = \frac{S(\vec{\Gamma}(l), E(\vec{\Gamma}(l)))}{S_{\mathrm{H_2O}}(E(\vec{\Gamma}(l)))}. \tag{2.11}$$

Since the left side is independent of location and the right side only weakly depends on energy, both sides can be integrated separately [46, 71, 72, 74]

$$-\int_{E_0}^{E_{\mathrm{R}}} \frac{\mathrm{d}E}{S_{\mathrm{H_2O}}(E)} = \int_0^l \mathrm{RSP}(\vec{\Gamma}(l'))\mathrm{d}\vec{\Gamma}(l'). \tag{2.12}$$

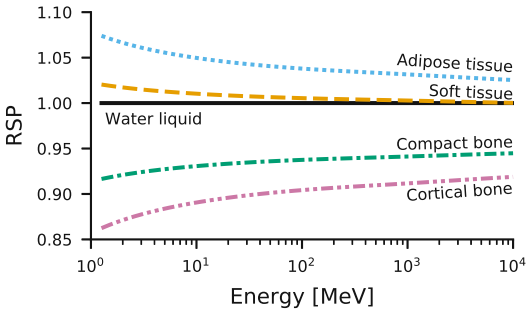

Figure 2.15: The relative stopping power (RSP) of protons in several materials.

The result of the left integral in equation (2.12) is called water equivalent path length because it is equal to the length of water in which the same energy loss occurs. It is evaluated from the initial energy E_0 – which is assumed to be equal to the accelerators' extraction energy – to the residual energy E_R that was measured with a detector. Energy losses in air are neglected [46, 71, 72, 74].

Relative Scattering Power

The concept of scattering power is introduced by differentiating equation (2.4) and reordering to introduce a concept of scattering power T, similar to the stopping power from energy loss imaging [44, 71–73]

$$\mathrm{d}\underbrace{\langle\theta\rangle^2}_{A} = T\left(X_0(\vec{\Gamma}(l)), E(\vec{\Gamma}(l))\right)\mathrm{d}\vec{\Gamma}(l), \tag{2.13}$$

which depends on the local radiation length X_0 and the energy loss prior to reaching a point along the path $\vec{\Gamma}(l)$. An equivalent formulation of the scattering power can be obtained by mapping the energy loss in a medium to the angular dispersion $E = h(A)$ [72, 73]

$$\tau(X_0(\vec{\Gamma}(l)), A(\vec{\Gamma}(l))) \equiv T(X_0(\vec{\Gamma}(l)), h(A(\vec{\Gamma}(l)))). \tag{2.14}$$

A similar scattering power for water is defined with its own mapping function $h_{\mathrm{H_2O}}$ [72, 73]

$$\tau_{\mathrm{H_2O}}(A) \equiv T(X_{0,\mathrm{H_2O}}, h_{\mathrm{H_2O}}(A(\vec{\Gamma}(l)))). \tag{2.15}$$

Finally, equation (2.13) is divided by the scattering power of water to obtain a relative scattering power in the same way as suggested for the relative stopping power [72, 73]

$$\mathrm{RScP}(\vec{\Gamma}(l)) = \frac{\tau(X_0(\vec{\Gamma}(l)), A(\vec{\Gamma}(l)))}{\tau_{\mathrm{H_2O}}(A(\vec{\Gamma}(l)))}. \tag{2.16}$$

As was previously the case, this allows to integrate both sides separately [72, 73]

$$\int_0^{A_\mathrm{R}} \frac{\mathrm{d}A}{\tau_{\mathrm{H_2O}}(A)} = \int_0^{l} \mathrm{RScP}(\vec{\Gamma}(l'))\mathrm{d}\vec{\Gamma}(l'). \tag{2.17}$$

The result of the left side of equation (2.17) is the scattering water equivalent path length: the length of water with the same increase in angular dispersion [72, 73].

Attenuation

Particle beams passing through an object to be imaged gradually reduce their intensity due to (inelastic) nuclear reactions (section 2.1.4). Though this beam attenuation is an unwanted side-effect in ion imaging, it can also be used to measure the nuclear cross section by counting the fluences of the beam entering and exiting the object. If the reduction in fluence is only due to inelastic nuclear scattering – that is, if events with elastic scattering are counted in the downstream tracking stages – then the cross section κ can be reconstructed based on equation (2.6). It can be directly reconstructed by defining projection pixel values g_i according to [46, 47, 71, 72]

$$g_i = -\ln\left(\frac{\Phi_i^{\mathrm{out}}}{\Phi_i^{\mathrm{in}}}\right), \tag{2.18}$$

with the particle fluences Φ_i^{in} and Φ_i^{out} of particles that intercept pixel i.

3 Materials and Methods

Over the course of this work two iterations of a demonstrator system for ion imaging were assembled and operated during beamtests to obtain data sets suitable for ion imaging. Both demonstrators included a beam telescope consisting of position sensitive detectors. These allowed to perform clustering, track fitting, alignment of the detectors and imaging based on beam particle scattering. The sensors of the first iteration were replaced by new ones, due to inefficiencies caused by radiation damage. Additionally, the second iteration featured a detector capable of determining the residual energy per particle. The otherwise independent tracking and residual energy systems were synchronised with a shared triggering logic and used to reconstruct the position resolved reduction of range due to energy loss.

Apart from conducting the measurements, an analysis based on Monte Carlo-simulations was developed to explore the requirements for a potential successor of the current demonstrator. Simulations of the movement of particle beams through a water volume were used to evaluate the achievable image resolution of different system configurations and detector parameters. By iterating through different parameter values this allowed to find intervals in the parameter space suitable for ion imaging. Requirements in terms of position resolution and material budget for a hypothetical new detector were identified, and the option of using three tracking planes per tracking stage (instead of two) was explored.

3.1 The MedAustron Facility

Beamtests were carried out at the MedAustron facility for ion therapy and research, located in Wiener Neustadt (Austria). The facility features a synchrotron capable of accelerating protons and light ions for treatment of deep seated tumours at depths of up to 38 cm for protons or 28 cm for carbon ions. MedAustron offers four irradiation rooms, three of which are reserved for clinical treatment and one available for non-clinical research (figure 3.1). Currently, proton and carbon ion beams are available at the facility, with a clinical energy range of 62.4 MeV to 252.7 MeV and 120 MeV/u to 400 MeV/u, respectively. The technical requirements

Figure 3.1: Layout of the MedAustron[1] facility [75].

to support 400 MeV/u carbon ions in the bending magnets of the synchrotron allow to accelerate protons to energies that exceed the energy range during clinical use. Therefore, the research room was built and commissioned to support an increased range of proton energies of up to 800 MeV[30, 75].

The facility was designed to operate with up to four electron cyclotron resonance ion sources, three of which are in active use: one to supply protons, one for carbon ions and one redundant source. A fourth slot could potentially be commissioned to support additional ion species, such as neon, helium, oxygen or nitrogen. To inject the extracted particles into the synchrotron, they are accelerated to 7 MeV/u by a radio frequency quadrupole followed by a linear accelerator. The particles reach their final energy in the synchrotron and can be extracted slowly, with pulses containing up to 10^{10} particles in a configurable extraction window lasting between 0.1 s to 10 s. Upon extraction, the beam can be guided to one of the irradiation rooms or a dedicated beam dump [30, 75].

Due to the single particle tracking operation of the imaging demonstrators it was

[1] https://medaustron.at

necessary to cooperate with MedAustron to commission additional configurations for the beam extraction of the accelerator. Available settings at the start of this research project had a high beam intensity, which would not have allowed to record individual particles in either of the tracking system or the range telescope. Therefore, custom extraction methods for low intensity beams were commissioned for lower rate physics experiments by tuning the injections into the linear accelerator and the synchrotron, as well as the extraction from the synchrotron. Three different settings were made available in the energy range from 62.4 MeV to 252.7 MeV, which support particle rates of 3 kHz, 350 kHz and 4.7 MHz [76].

Reduced rates were available for the central beam spot only, since the dose delivery systems of the accelerator were built for much higher beam intensities and could not pick up electromagnetic signals from the bunches exceeding noise. Though this posed no problem for the beamtests within this work, it would have prevented imaging of head-sized phantoms unless a new controller for scanning spots or a scattering body in front of the measurements would have been used.

3.2 Software Tools

3.2.1 Geant4

The freely available Monte-Carlo simulation framework Geant4, version `10.5.p01`, was used to create a simulation of a generic single particle tracking system (section 3.5). Geant4 provides many classes for the simulation of high energy particle physics, such as physics models governing the interactions of particles and matter, the description of volumes involved in the simulation (geometry and materials), detector logic, particle sources, visualisation and UI messengers: classes that allow users to interactively configure and run simulations with a macro language [77].

Geant4 provides several `C++` libraries that users are supposed to link to their own simulation executables. The framework handles particle transport and interactions, but uses inversion of control to let users create their own logic for certain steps during the simulation: for example after updating a particle's state or when a run has finished. To do that, users have to implement several abstract classes that are called by the framework [77].

Detector construction defines the physical setup of the simulation, which includes geometry, materials, the sensitive volumes and the detector classes attached to those volumes.

Physics list defines the available particles and all physics processes that are used in the simulation. This class does not strictly need to be implemented by users, since several framework provided physics lists are available, but the user must instantiate and initialise one.

Action initialisation defines the user action classes that are used during inversion of control-steps in the simulation. While the primary generator must be defined, other user action classes, such as the run action, event action, stacking action, tracking action and stepping action default to a `null` behaviour, effectively doing nothing when called.

Primary generation action instantiates and initialises primary particles during the simulation. This class does not strictly need to be implemented, but users must instantiate and initialise one in the action initialisation.

Although default implementations of the following classes are available, these were overridden for the simulations of this work. The descriptions below are not general examples of Geant4 but rather specific to the simulations conducted in this work:

Sensitive detector instantiates a hit object when particles interact with a detector volume, which stores the current interaction position and kinetic energy of the particles until the end of an event.

Run action configures the output file format; a table with columns for the interaction positions, kinetic energies, and whether the hit occurred in a detector or in the phantom.

Event action collects all hits that occurred during an event. If an event is complete – no or only a few hits are missing – it is stored in an output file.

At the beginning of a simulation executable an instance of the *G4RunManager* singleton must be connected to instances of the detector construction, physics list and action initialisation classes. This run manager has control over the simulation state machine and will initialise, carry out and finalise runs as soon as *BeamOn* is called through either the main executable or a UI messenger command [77].

3.2.2 GATE

GATE is an additional layer on top of Geant4 that adds several tools to allow users to more easily build a functioning simulation. Among them are the actor concept and a large amount of UI messengers, both of which were utilised for several figures in chapter 2 of this work, using version `v8.2` of GATE [78].

Actors in GATE are a group of detector classes that are attached to the otherwise passive volumes in a Geant4 simulation. An actor object essentially adds a sensitive detector to the volume it is attached to and then performs some logic during the action phases of a simulation, such as the individual steps of a particle track or the end of a run. The logic performed depends on the actor itself – for example, a dose actor records the dose distribution within a volume, whereas a phase space actor records the properties of each passing particle [78].

Another important aspect of GATE is the large amount of UI messengers. Messengers provided by GATE define many commands to instantiate physical volumes, create and attach actors, and to define particle sources. Users are supposed to configure the simulation with these messenger macros, which is reflected by the method of running the simulations. In contrast to simulations built on Geant4, where users are required to program the detector construction and compile their own executables, GATE comes with a single executable that interprets macros [78].

Several GATE actors were used for counting particles and recording their positions as well as dose and energy depositions.

Production and stopping actor stores positions of particles that were created or which terminated within a volume in a histogram.

Dose actor stores the position-resolved dose deposition within a volume in a histogram.

Phase space actor Stores selectable properties of particles that enter or exit a volume, such as species, position, direction, energy or momentum in a table.

3.2.3 Corryvreckan

The Corryvreckan framework for beam telescope track reconstruction, version `v2.0` was used extensively during the production of this work, to perform track fitting, telescope alignment and several analyses with data from beamtests at MedAustron and from Monte-Carlo simulations. It is a `C++` program that dynamically loads, configures and runs modules – small processors that carry out the individual work steps in an analysis – based on text configuration files. A core library contains classes for parsing configuration files, a shared temporary storage called clipboard, detector definitions, the abstract base class of a module and a module manager which controls the programs state machine and handles the event loop. The core is extended by an *objects* library, which defines classes that can be stored on the clipboard, such as pixel hits, clusters or tracks [79].

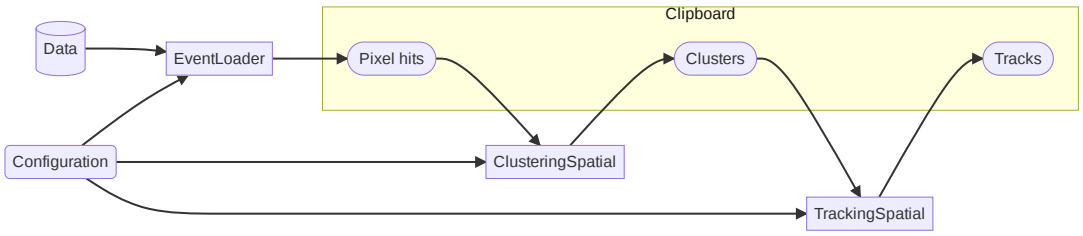

Figure 3.2: Example of a Corryvreckan tracking analysis. Modules interact with the clipboard by loading and storing temporary data, such as pixel hits, clusters or tracks. In this example an event loader puts pixel hits on the clipboard, which are converted to clusters, and the clusters to tracks. Each module has access to the configuration and the clipboard, but not to other modules.

All of the logic of an analysis is encapsulated in module classes so that the individual work steps are logically separated. Figure 3.2 illustrates a hypothetical analysis based on Corryvreckan: each module interacts with the clipboard only. They can load, transform and store objects on the clipboard, but do not directly interact with each other. Typically, a loader module loads raw data from a data file and stores pixel hits – a class that holds the row, column and signal strength of a single activated pixel – on the clipboard. Another module for clustering can then combine adjacent hits to form a cluster – a collection of hits to calculate their center of gravity – and store it on the clipboard for tracking modules to use [79].

The structure of an analysis and the behaviour of the involved modules can be controlled with text files, referred to as configurations. Each configuration contains sections for the modules being used and key-value pairs for each of the parameters of the modules. For the example analysis in figure 3.2, four sections would be used: one global section that applies to all modules and one section for each module. At the beginning of an analysis Corryvreckan's module manager instantiates modules in the same order as their sections appear in the configuration. This order is also used throughout Corryvreckan's simple `initialise`, `run`, `finalise`-state machine, where inversion of control is used at each of the three states to allow modules to fulfil their purpose. Each module can initialise itself – for example, to create histograms or reserve memory for member variables – prior to the event loop (the `run`-state). During the event loop, the modules can return signals to the module manager, to indicate whether processing was successful for a single event, no data was available, the event should be skipped or the analysis should be terminated. After all events have been processed, the modules can finalise their tasks – for example, to calculate statistics or store results in an output file [79].

Over the course of this work, several modules of the Corryvreckan framework were used, such as:

TrackingSpatial performs a search for track candidates using a linear extrapolation and spatial cuts. This module only supported straight lines at the time of writing.

Tracking4D similar to TrackingSpatial, but additionally considers time cuts and supports the GBL model for tracks in air.

TrackingMultiplet performs tracking for two tracklets that are connected at a single point of closest approach, with a kink angle between them. Both straight line tracks and general broken lines are supported for the tracklets.

Prealignment roughly aligns telescope planes with respect to a reference plane based on the correlation of hit positions between different planes.

AlignmentTrackChi2 aligns telescope planes with respect to a reference plane by minimising the χ^2-distribution of many track fits.

AnalysisMaterialBudget creates a 2D-resolved projection image at a plane perpendicular to the beam-direction, by visualising the kink angle distribution width of tracks intersecting the plane.

3.2.4 Scikit-image

The freely available image processing library scikit-image [80] was used to reconstruct three dimensional tomograms based on projection images from the Corryvreckan analyses. Two inverse transforms – filtered back projection [81] and simultaneous algebraic reconstruction technique (SART) [82] – are available in the library, out of which SART was used. It should be noted, that neither of these methods is inherently suitable for the reconstruction problem with charged particles, since they were originally implemented for X-ray tomography and do not take the nonlinear trajectories of particles into account. The method does, however, yield promising results for high energy electrons used in imaging of thin scattering bodies [61]. Using Monte-Carlo simulations it is simple to demonstrate that the difference in image resolution is negligible among different path models for such a small phantom (see below). Additionally, the expected image resolution due to multiple scattering would have been larger than what could be exploited with the available data from the demonstrator, since the number of particles per pixel was low enough at the edge of the beam spot so that meaningful statistics could only be obtained for pixels greater than $0.5 \times 0.5\,\mathrm{mm}^2$.

Scikit-image functions for inverse transforms expected many projections measured at different rotation angles around an axis in the center of the phantom, such as the vertical axis (which was used throughout this work). To use SART it

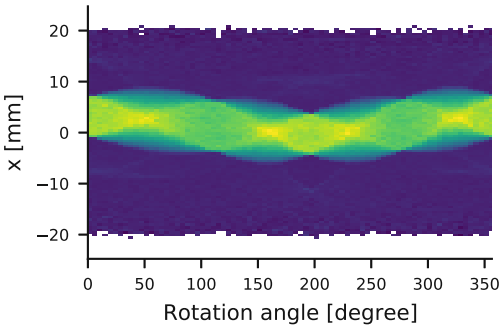

Figure 3.3: Example of a sinogram for a stair phantom.

was merely necessary to rearrange the projection images into many sinograms, one for each horizontal line at a constant value of the vertical coordinate (figure 3.3). Thus, each produced sinogram contained line profiles along the horizontal coordinate, at different rotation angles of the phantom. In this work the x/y-plane was consistently used for detector coordinates and projection images, whereas z was used for the initial beam direction. The phantom was rotated around the y-axis, the perpendicular coordinate in the sinograms was x and the reconstructed section images were in the x/z-plane.

Three-dimensional tomograms were then rendered using contour functions provided by the *mlab* API of the python library Mayavi [83].

The single kink model was used for producing projection images from measurements throughout this work. Projections were then reconstructed with the SART algorithm. Though this choice opposes standard practice in ion imaging – where the MLP model is used in conjunction with reconstruction algorithms for curved lines – it is not unreasonable for this work, due to the small size of the used phantoms. In fact, it could be demonstrated that the single kink model is comparable to the MLP model in terms of image resolution in a 10 mm aluminium phantom, using Monte Carlo simulations (section 4.3.6).

3.3 Demonstrator System

Two iterations of a demonstrator system for ion imaging were used for data taking. At first, a telescope made of four square sensor modules and no residual energy measurement was made with readily available components (section 3.3.1). This system was eventually replaced by another detector, with new sensors for the

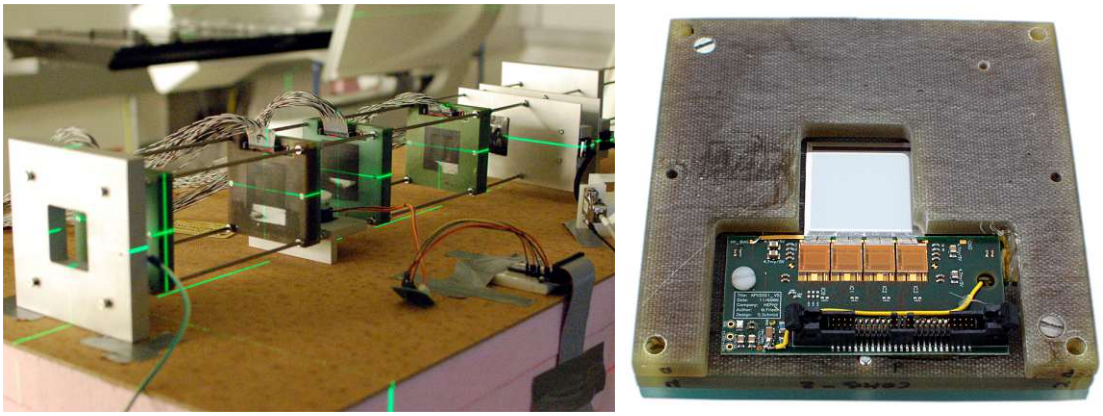

(a) (b)

Figure 3.4: (a) Photograph of the first generation telescope used at MedAustron. (b) Photograph of the p-side of one first generation detector module.

trackers and an additional range telescope. Tracking and residual range measurements were synchronised with a dedicated triggering system, so that tracks and energy losses could be correlated per particle (section 3.3.2).

3.3.1 Particle Tracking with a DSSD Telescope

The first demonstrator was constructed from four DSSD modules mounted on four metal rods and held in place using fixing collars. Together with an available positioning laser this allowed a precision of less than a mm in the beam direction and a few degrees in rotation (figure 3.4a). In between the second and third detector was a rotating table to hold a phantom in place. Two $50 \times 50 \times 10\,\mathrm{mm}^3$ plastic scintillators[2] for triggering were placed downstream of the last module so that no additional energy loss and scattering would compromise the tracks due to the scintillator material. Each of these scintillators was connected to a photomultiplier (PMT)[3] via an acrylic light guide, and wrapped in light-tight tape. A coincident signal from both PMTs was obtained by converting the analog signals to a single digital pulse with a discriminator[4] and a logic and-operation on the two pulses.

Each of the tracker modules had a carrier structure that held a 300 µm thick DSSD and its front-end electronics in place (figure 3.4b). The sensors had an active area

[2]EJ-228 Fast Timing Plastic Scintillator, Eljen Technology
[3]H10721-210 Photosensor Module, Hamamatsu
[4]V895 16 Channel Leading Edge Discriminator, CAEN SpA

of 2.56 mm × 2.56 mm with orthogonal strips on both sides of the same silicon bulk. One side of the sensors used 512 p-doped strips with a pitch of 50 µm. The other side only had 256 n-doped strips with a pitch of 100 µm due to additional p-doped implants between the strips to prevent an accumulation of electrons on the surface that would otherwise short-circuit strips. Strips on both sides were connected to their respective APV25 readout chips [84] through wire-bonds. Since each of the chips could handle 128 strips, there were four chips on the p-side and two on the n-side. Leftover sensor modules were readily available from a former radiation hardness study in which they were irradiated with a 700 kGy dose with a Co-60 source [85].

In the first iteration of the telescope, a prototyping system for the readout electronics employed at the Belle II Silicon Vertex Detector [86] was used to collect strip signals and transfer them to a personal computer via a VME bus. This system was replaced by a similar but more refined version, which is explained in section 3.3.2.

3.3.2 Full Demonstrator System

A new telescope was constructed from previously unused sensors, since the initial tracking modules were irradiated with a large dose and radiation damage was evident. Additionally, a range telescope from the TERA foundation [58] was acquired to be included in the demonstrator. The complete demonstrator consisted of two sets of up to three tracking detectors that were placed upstream and downstream of a rotating table with a phantom. Two scintillators for triggering were placed after the downstream tracker set and in front of the range telescope, which terminated and measured the residual energy of the beam (see figure 3.5).

Upgraded Tracking System

Tracking sensors used in the second generation demonstrator were slightly different than those from the first telescope. Similarly to the first version, the sensors were DSSDs with a thickness of 300 µm and orthogonal strips on both sides of the sensor. As was previously the case, the strip pitch was 50 µm on the p-side and 100 µm on the n-side, though the total number of strips was 512 for both sides. This meant that the sensors had a rectangular shape with an active area of 5.12 mm × 2.56 mm and four APV25-chips on either side (figure 3.6).

A VME based readout system that was developed for the Belle II Silicon Vertex Detector [88] was used to transfer raw data from the sensors to data files on a

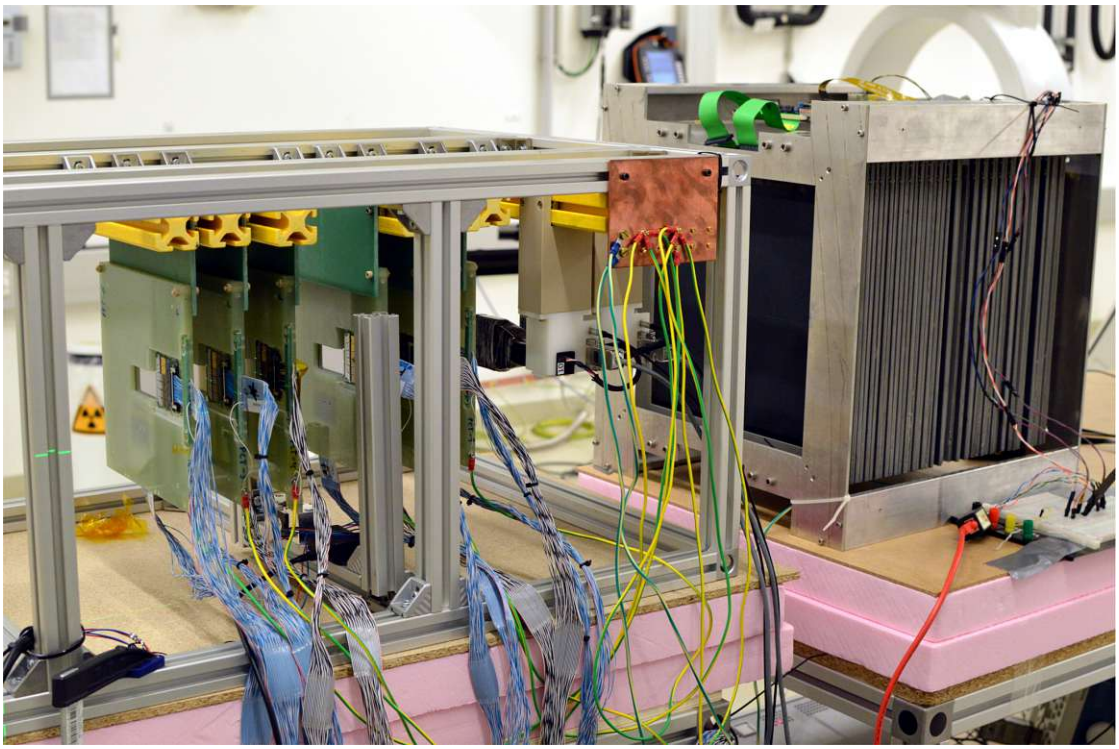

Figure 3.5: Photograph of the current demonstrator system for ion imaging, using upstream and downstream tracking triplets, two scintillators for triggering, and a terminal range telescope to measure the residual energy.

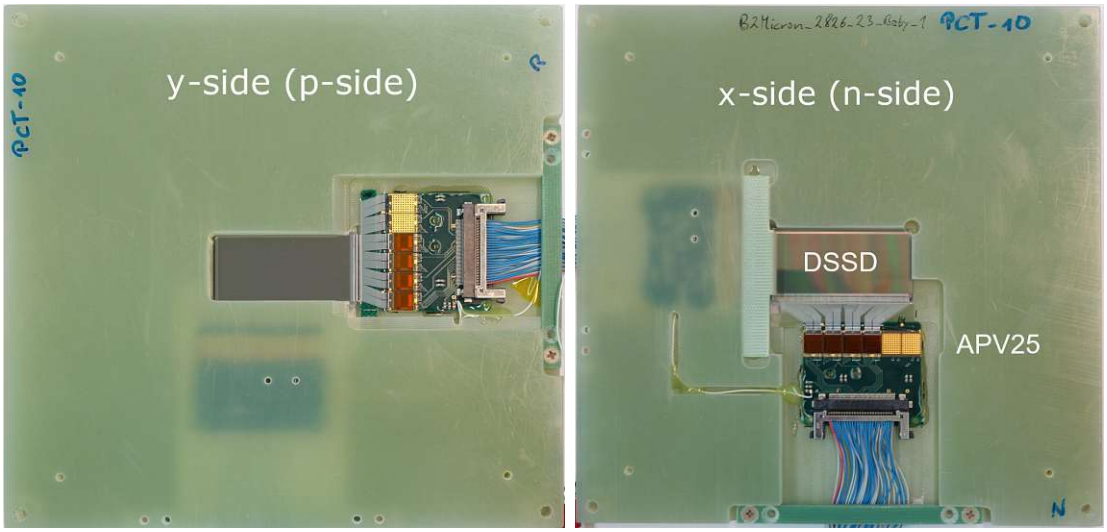

Figure 3.6: Photographs of both sides of a tracker module. The silicon strip sensor is connected to the front-end electronics on each side using a pitch-adapters [87].

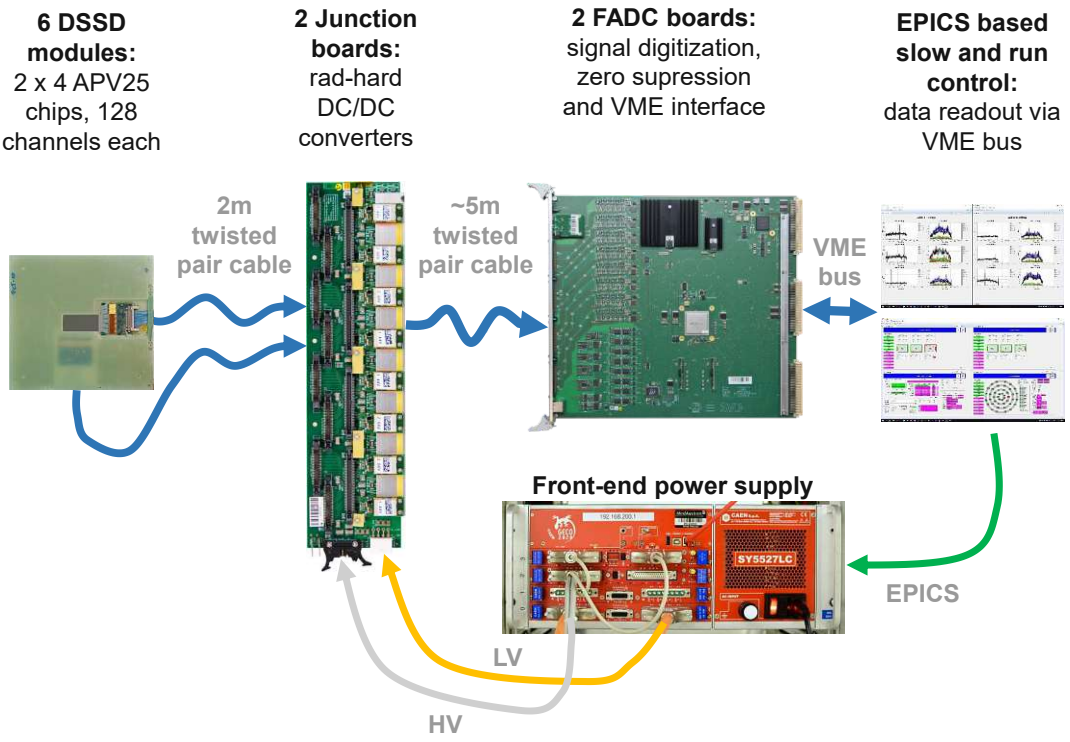

Figure 3.7: Sketch of the tracking system readout [87].

personal computer (figure 3.7). Strip signals were amplified, shaped, sampled and buffered in an analogue pipeline by the APV25 chips [84], to allow a configurable latency between the trigger and a readout. The chips were fixed to hybrid boards directly on the detector modules, each of which could support up to six APV25s. They were connected to up to two junction boards – each supporting a maximum of eight hybrids or four modules – that supplied voltage for the front end electronics and the biasing to deplete the silicon sensors. In addition to powering the modules, these junction boards connected hybrids to the flash analog digital converter (FADC) boards responsible for digitisation, noise corrections, zero suppression and event building prior to the block transfer to a computer [87, 88].

Two different transfer implementations were used. Initially, events were read out via the VME bus of the crate hosting the FADCs and an optical bridge to a PCIe slot. This was eventually replaced by a readout using a direct gigabit ethernet connection, which allowed to increase the data acquisition (DAQ) rate of single particle tracking from ≈0.5 kHz to 2 kHz. The computer connected to the readout electronics ran several services that together implemented a run and slow control

system built upon the EPICS protocol[5]. Together with a user interface written in `Java` this system allowed to operate and monitor power supplies and DAQ in a distributed way. Many process variables – for example the current run control state, error messages or measurements from the power supply – were made available in the local network of the readout computer. These variables could be picked up or modified by other computers in the same network, which only needed the user interface installed on them to interact with the DAQ [89].

A copy of the `xml` configuration and at least one binary data file containing either raw or zero suppressed data from the FADCs were created during each acquisition. Data files containing raw data needed to be preprocessed by applying a pedestal and common mode noise subtraction. After reordering the strip signals and removing the digital headers and tick marks inserted by the APV25s, the data contained six time samples of ADC counts. An example of an event with two active strips on a single APV is illustrated in figure 3.8. The frame with maximum signal was usually used for cluster finding and analyses built upon the cluster positions.

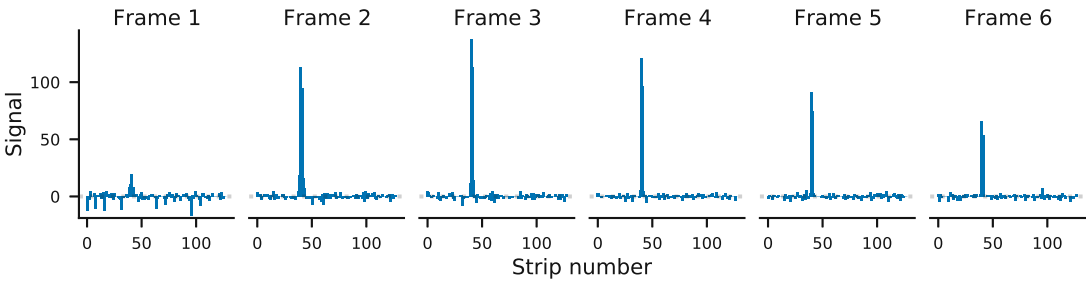

Figure 3.8: Time structure of a single APV25 event. Six consecutive samples allow an accurate reconstruction of the dose deposition as a function of time.

Range Telescope for Residual Range Measurement

To determine the stopping power distribution of an object it was necessary to include an energy loss measurement of each particle. In the prototype this was realised with a range telescope built by the TERA foundation [58], which was composed of 42 plastic scintillator planes[6] with an extent of $3 \times 300 \times 300\,\mathrm{mm}^3$. Each plane was connected to a SiPM[7] and wrapped in aluminium foil and dark paper to reflect internal light back and isolate the scintillator from outside light sources (figure 3.9) [87].

[5]Experimental Physics and Industrial Control System (`https://epics.anl.gov/`)
[6]BC-408 Premium Plastic Scintillator, Saint-Gobain Ceramics & Plastics, Inc
[7]MPPC S10362-11-050C, Hamamatsu

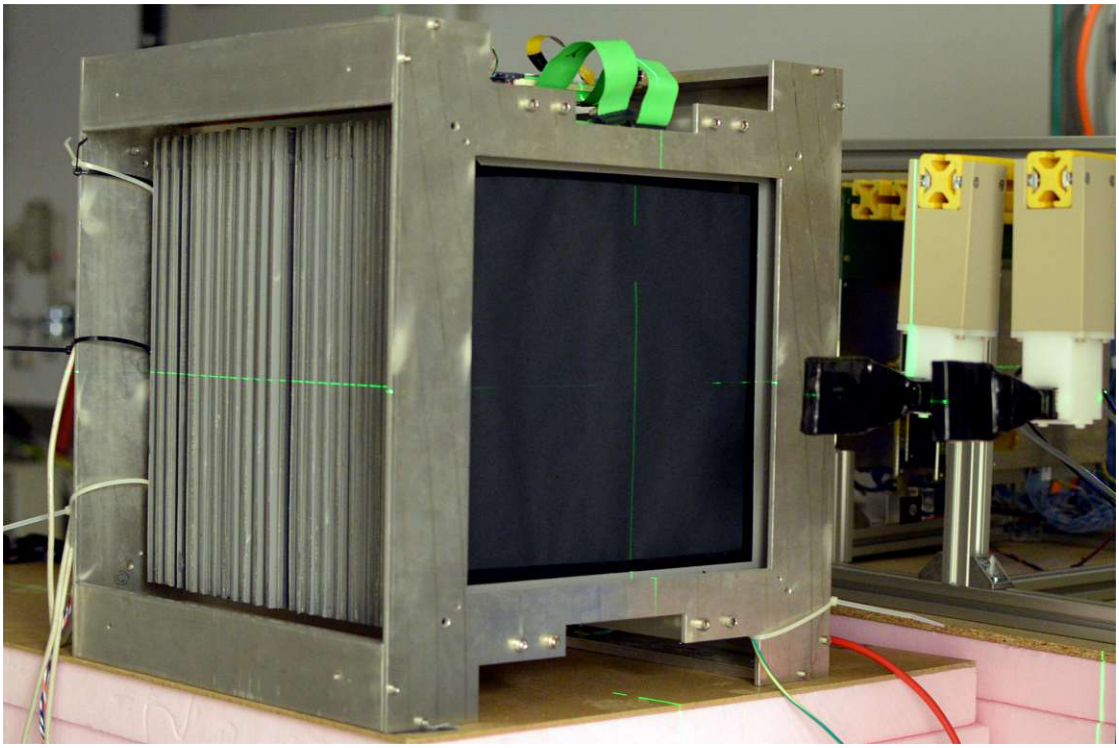

Figure 3.9: Photograph of the range telescope for measuring the residual range of the particles and the trigger modules for initiating a readout.

The SiPMs converted scintillation light into electrical signals that could be picked up by the readout electronics. Each SiPM consisted of an array of 400 avalanche photodiodes, so that the amount of active cells in the array should be proportional to the amount of light in the scintillator (and therefore, the energy deposition). This operation method was, however, not possible with the current demonstrator, since the low number of pixels supported a dynamic range incapable of accurately measuring the different energy depositions at the Bragg peak and the plateau leading up to it. Therefore, it was operated as a range telescope: to measure the residual range of each particle instead of sampling its energy depositions.

Hypothetically, the complete assembly could terminate and measure a proton beam with an initial energy of approximately 140 MeV. Though a reduced rate beam was available for 145.4 MeV, it was decided to use a lower energy of 100.4 MeV for imaging over concerns of whether the smaller spot size at 145.4 MeV would fully cover the phantom.

This decision also allowed to mitigate technical issues with the detector. Instabilities in the voltage supplies of the SiPMs caused noise and frequent failures in some of the slices; a reliable operation over a long beamtest was deemed improbable at

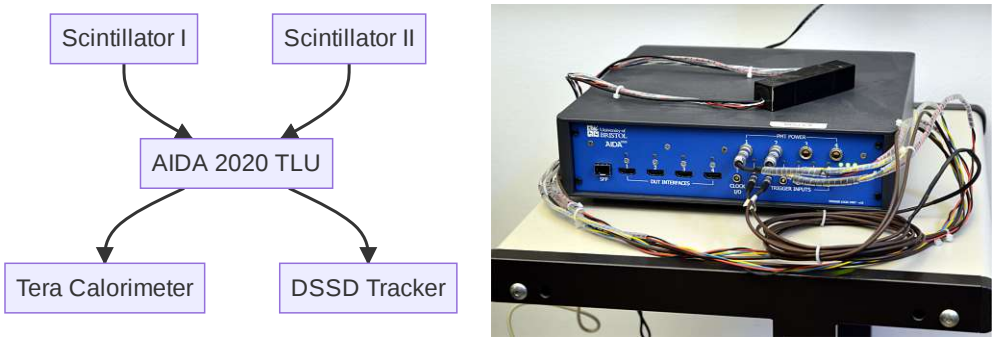

(a) (b)

Figure 3.10: (a) Sketch of the trigger system connections. Both trigger scintillators are glued to photomultipliers (PMTs) powered by the trigger logic unit (TLU). The PMT signals enter the TLU, which internally creates a logic AND of the two signals to trigger an event for the calorimeter and tracking devices. (b) Photograph of the AIDA2020 TLU.

the time. Therefore, unfailing slices were positioned at the front of the detector and the beam energy was reduced so that the maximum range of particles traversing mostly air could be measured with certainty. This also had a positive side effect on the range resolution due to reduced range straggling.

Triggering System

A common trigger logic was necessary so that raw data from the otherwise independent detector systems (tracker and calorimeter) could be correlated during the analysis. Though the two plastic scintillators were kept to provide a fast trigger signal, the AIDA2020 trigger logic unit (TLU) [90] was introduced to the demonstrator to replace the simple and-operation used in the first iteration of the demonstrator. It could supply power to the photomultipliers and collect their analog signals. The TLU was also connected to both of the devices (calorimeter and tracker) to handle a synchronous readout (figure 3.10).

Events were initiated by the TLU when a coincident (within a short time frame) signal occurred in both of the trigger modules (figure 3.11). The tracking system and calorimeter were notified through a digital trigger signal that changed state from low to high at the beginning of an event. Both devices responded by raising a busy signal which inhibited the TLU from initiating additional events until the devices were ready again. Then, the TLU changed its trigger state from high to low, followed by the transmission of a 15 bit long trigger number for the current event (an incrementing counter reading) to the devices, which they included in

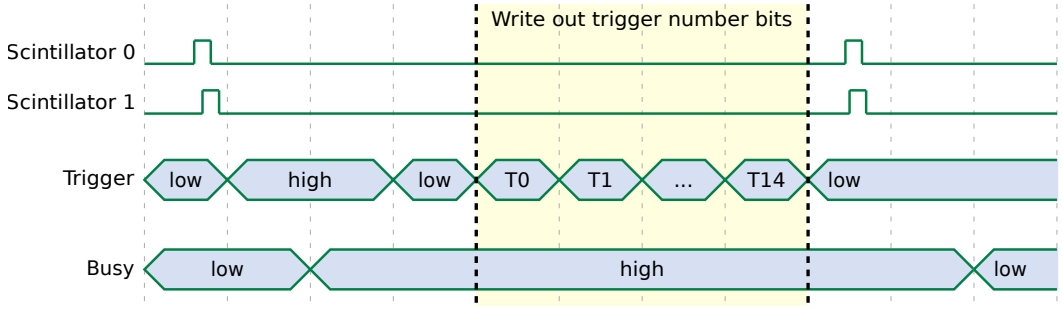

Figure 3.11: Sketch of the trigger sequence of an event. A coincident signal causes the trigger logic unit (TLU) to raise a trigger signal, which then starts a readout in both devices. Devices raise their busy signals as an acknowledgement and to prevent additional triggers during the readout. Afterwards the TLU sequentially sends out the individual bits of the current trigger number.

their respective raw data files. This allowed events to be uniquely identified by their trigger number, regardless of the readout technicalities of the devices. Both devices lowered their own busy signal as soon as they were finished with their own readout procedure. Finally, the TLU was ready to initiate another event as soon as all of the busy signals were lowered.

3.4 Imaging with the Demonstrator

Both of the demonstrator iterations were used to perform track reconstruction and imaging based on multiple scattering [87, 91]. Additionally, the current iteration was used for attenuation and energy loss imaging. Raw data from the sensors required several work steps in preparation that are summarised in section 3.4.1. Among these steps were the conversion of activated silicon strips to clusters, track fitting and the tracker alignment procedure.

It was unexpected that the setup could produce attenuation images, since the method for obtaining projection images relies on counting particles without a track in the downstream tracking stage. Given that the triggering scintillators were placed downstream of this tracking stage, it was expected that most of the recorded particles would also have an associated downstream track. It turned out that this was not the case, since the triggers had a larger cross section than the tracking detectors. Therefore, attenuation images could be produced with this setup even though a dedicated attenuation imaging system would normally place the triggers in front of the object to be imaged.

Due to imprecisions in the placements and rotations of physical sensors, measured clusters are usually biased with systematic offsets with an order of magnitude of ≈1 mm and 1°, respectively. These biases can be corrected by performing an alignment for the telescope, using no phantom between the upstream and downstream tracking stages and a high energy beam, so that scattering in air and detectors is reduced. Therefore, a single data set was recorded without a phantom placed on the rotating table and with a high energy beam – usually 250 MeV – at each beam test. This dataset was used to carry out an alignment, which reduced the uncertainty of detector placements to below 100 µm. The phantom was placed on the rotating table only after a successful alignment was obtained. Afterwards the imaging data sets were measured with a lower energy beam in the range of 100 MeV to 150 MeV. Positioning and a complete coverage of the phantom with the beam were verified using track based imaging and a short acquisition of approximately 10^5 events. Finally, a large amount of projection data sets were recorded at different rotation angles, using up to 2.5×10^6 events per rotation. Imaging measurements were carried out for many rotation angles of the phantom, so that a three-dimensional tomogram of the reduction of range could be obtained using image reconstruction techniques (section 3.4.2).

3.4.1 Tracking Data Preprocessing

Preprocessing was carried out with modules provided by Corryvreckan and one additional module developed for loading raw data from files and storing clusters on the clipboard. An overview of the workflow is illustrated in figure 3.12. Each rectangle in the illustration represents a configuration for a single Corryvreckan analysis that contained sections for several Corryvreckan modules. All of the analyses used a section for the custom event loader – which performed clustering for the silicon strip data – and additional sections based on the modules needed for the work steps within the analysis. Furthermore, all analyses required a geometric configuration of the detectors provided in a text file called the detectors file. The original detectors file described the ideal geometry of the beamtest, with no uncertainty taken into account. It was written based on handwritten notes of the physical setup and contained one section per detector plane with the parameters of the detector, such as its strip pitch, the number of strips and the placement in the beam direction. This file was updated twice, once during the prealignment step and once during the alignment. Imaging runs only made use of the aligned detectors file, since this configuration contained the most accurate description of the realistic setup.

After the alignment produce, which was carried out once, many data sets were

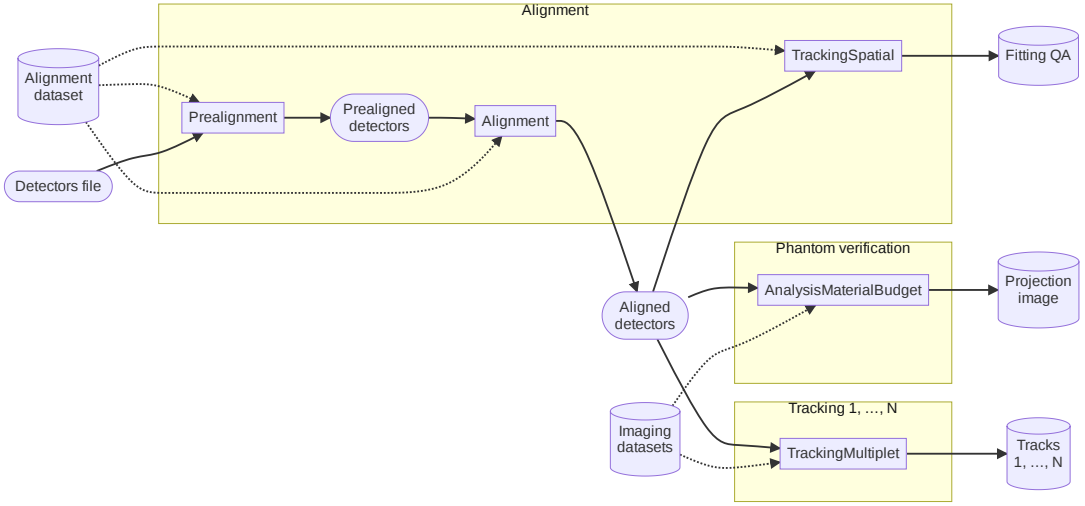

Figure 3.12: Alignment and tracking procedure performed with Corryvreckan. A rough prealignment is used as an initial guess to guarantee a fast and accurate alignment. Following the alignment, track fitting is performed once more on the alignment dataset to verify the alignment quality. Afterwards the sample or device under test is installed in the telescope and many track fitting runs may be carried out based on the aligned detectors file.

recorded at different phantom rotations. These were converted to tracking data sets or projection images in many similar analyses that merely differed in which data file was used. For example, a single projection image was produced at the start of the DAQ for imaging to confirm a full beam coverage of the phantom. Afterwards many data files with track fits were created to combine with energy losses from the residual energy detector, to produce a stopping power tomogram in a work step outside of Corryvreckan.

Tracker Event Loader

Raw data from the silicon sensors were stored on the clipboard by a custom written module called *EventLoaderPCTMA*, where *PCTMA* is short for proton computed tomography at MedAustron. Unlike conventional Corryvreckan loader modules this custom loader did not store pixel hits on the clipboard – which would require a clustering module to be used - but rather internally performed clustering and stored clusters instead. This was necessary due to the use of strip detectors and the one dimensional clustering associated with them. Clusters were first calculated on each of the strip coordinates and combined afterwards. For pixel hits the clustering algorithm would have used both coordinates to calculate a two-dimensional cluster position instead.

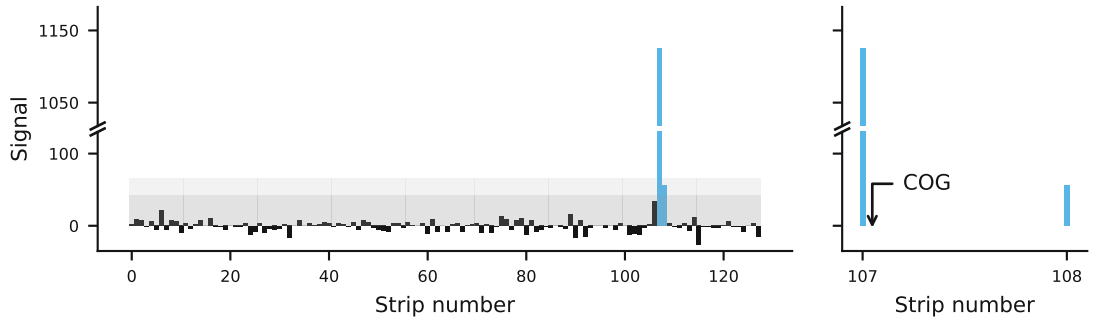

(a) (b)

Figure 3.13: Thresholds and center of gravity (COG) of a two-strip cluster. (a) The seed (middle) strip signal must exceed 5 times its noise to be considered a cluster. Neighbouring strips are included if their signal exceeds 3 times their noise. (b) A center of gravity of all strips in a cluster is calculated to yield an accurate position measurement.

Candidates for a cluster were identified by comparing thresholds to the strip signals for each of the strips in a given event (figure 3.13). Two thresholds were used: a *seed* threshold to find potential clusters and a slightly lower *neighbour* threshold to include neighbouring strips into an identified candidate. Both threshold values were calculated as a multiple of the strip noise in a given event, where the multipliers were configuration parameters of the module. Default values of 5 and 3 times the strip noise were usually used for the seed and neighbour multipliers, respectively, if no explicit parameters were configured in an analysis.

Cluster positions were calculated as the center of gravity (COG) of the strip signals, so that the relative signal heights of the strips in a cluster could be utilised to accurately predict the interaction position. Both components in the x- and y-direction were calculated separately to yield the components of the COG and the equation for the y-component is analogous to the equation for the x-component

$$\mathrm{COG}_x = \frac{\sum_{i=i_{\min}}^{i_{\max}} x_i s_i}{\sum_{i=i_{\min}}^{i_{\max}} s_i}, \tag{3.1}$$

where x_i and s_i are the strip positions and signals, respectively. While this method can improve the accuracy of position measurements, it is only available for detector systems that read out the individual strip signals, such as the one used in this work. A readout that only produces a boolean signal – whether a strip was above a threshold or not – would end up with a worse position resolution [49].

After calculating the two one-dimensional COGs the loader counted the available clusters. Only events with a single cluster in both coordinates were processed

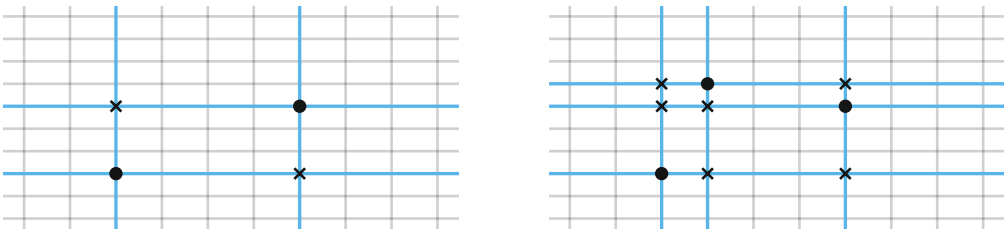

(a) (b)

Figure 3.14: Ghosts and actual clusters on a pair of strip detectors for (a) two and (b) three interactions. Ambiguity between ghosts and real clusters rises with a power of two of the number of interactions.

further, while others were dropped due to a missing measurement or because they were potential ghost hits. Ghost hits were ambiguous candidates for clusters when there were two or more candidates on at least one of the strip detector's sides (figure 3.14). Since the strip readout on either side was one-dimensional it was not easily evident which of the candidates was a result of an interaction and which of them was a ghost hit. For two clusters there would be two correct positions and two ghosts, whereas for three clusters there would be six ghosts already since the number of candidates is the squared number of clusters. Other detector layouts, such as pixel detectors or strip detectors with stereo angles, a measurement of the signal height in the strips, or pattern recognition in conjunction with track reconstruction could have been used to dispose of ghost hits. However, ghost hits did not occur in many events due to the particle rate of the beam used; which was low enough for single particle tracking. Therefore, events with ghosting were simply discarded.

Prealignment

The alignment procedure for a beamtest was performed in two steps. First, a rough prealignment was carried out using only the cluster positions (and no tracking) and the *Prealignment* module provided by Corryvreckan. It used the first plane in the beam direction as reference plane and shifted subsequent planes in the coordinates perpendicular to the beam direction. Each of the shifts moved the spatial correlation between cluster hits on the plane and on the reference plane in such a way that the correlation was centered around zero. Although the preliminary alignment was not very accurate it was robust and allowed track fitting to be performed, paving the way for an alignment based on a large number of tracks [79, 92].

Besides a large value of 100 for the time cut parameter only default values were used in the configuration of the preliminary alignment. Since the DAQ of the demonstrator guaranteed that only individual proton tracks were recorded in each event, and since no time difference was stored in the clusters, there was no need for a time cut. However, the Prealignment module skipped pairs of clusters with a time-difference of 0 and so a large value was set for the cut.

Track Reconstruction

Track models attempt to reconstruct the trajectories of individual particles from the point measurements at the detector planes. Two different models were supported in Corryvreckan and used for analyses of the beam test data, namely straight line track (SLT), a simple straight line; and general broken lines (GBL), a set of straight lines with kink angles at the detector planes [60]. Both could be used either as simple track fits for a set of position measurements, or to form multiplets: pairs of tracks that meet at a point of closest approach with a single kink joining them. Whereas the simple track models were intended for fitting a single track to several position measurements, multiplets were better suited to two sets of measurements separated by a large distance or a scattering body, such as a phantom. This made them ideal for the imaging data sets, since the upstream and downstream paths of a particle track could differ significantly in their direction vector, and a single straight track would be an inadequate model in this case.

Tracking modules started their process by identifying candidates for tracks, using an extrapolation from initial track candidates to include additional measurements on subsequent detector planes. Although this approach could potentially find several tracks per event, only either one or no tracks were found in the data of this work due to the single tracking nature of both the demonstrator and the simulations. Following the identification of track candidates from the measurements, a track fit was carried out by the module to calculate residuals – differences in position of the measured cluster coordinates and the track intercepts on each detector plane – and the reduced χ^2 statistic used to judge the alignment quality

$$\chi^2 = \sum_{i=0}^{N} \left(\left(\frac{\hat{x}_i - x_i}{\sigma_x} \right)^2 + \left(\frac{\hat{y}_i - y_i}{\sigma_y} \right)^2 \right), \tag{3.2}$$

where $\hat{x}_i$ and $\hat{y}_i$ are track fit intercepts, x_i and y_i are position measurements and σ_x and σ_y are position resolutions in x and y, respectively. The terms $\hat{x}_i - x_i$ and $\hat{y}_i - y_i$ are the residuals for both detector coordinates, which under ideal circumstances

should be centered around zero with a distribution width of 5 µm to 9 µm for the 50 µm pitch [93], or 15 µm to 32 µm for the 100 µm pitch coordinate [94].

Track candidates would be rejected by the module if their associated χ^2-value was beyond a configurable maximum value. This was intended to discard tracks depending on their fitting quality, so that only optimal tracks would be used for alignment or analysis purposes. Similar cuts were available for the position difference in subsequent measurements; however, due to the large amount of multiple Coulomb scattering in air and in the detectors it was necessary to use large spatial cuts of 1 mm. Otherwise only a small proportion of the events would yield track fits.

For the beam test data, simple track models were used during the alignment and for the verification of track fits, once the alignment was obtained. With the first iteration of the ion imaging demonstrator the GBL model was not yet implemented in Corryvreckan, and so only straight line track (SLT) was used for these data sets. However for the current iteration both models were used and compared in terms of the residuals and in terms of the χ^2-distribution of the fits. Owing to their usefulness for imaging, multiplets were used to create projection images of beam test data and for connecting different parts of the trajectories in studies on the most likely path uncertainty (section 3.5).

Alignment

Given a large number of track fits, a program could shift and tilt the detector transforms until the χ^2-distribution of the track fit residuals approaches a minimum. The obtained shifts and tilts could then be used to transform cluster coordinates, so that their bias disappears and the residuals would be centered around zero. This procedure was built into the Corryvreckan module *AlignmentTrackChi2*, which iteratively updates detector transforms and repeats track fitting, according to a parameter *iterations* [79, 92].

It was used to align measurements together with dedicated 252.7 MeV alignment runs recorded at the beginning of each beamtest. Track fitting was performed once more with corrected cluster positions, so that the quality of the measurement could be reviewed. Residual distributions were used to estimate the achievable position uncertainty of cluster measurements, which depends on the intrinsic resolution and the amount of multiple Coulomb scattering. Additionally, χ^2-distributions were compared to theoretical expectations. Since measurements with six planes could be carried out, these comparisons were made with both SLT and GBL track models.

3.4.2 Imaging Workflows

Three different imaging workflows, each based on a different mechanism, were used in this work. Images based on multiple scattering were produced with the *AnalysisMaterialBudget* module, which was originally provided by the Corryvreckan framework. It was slightly adapted to work with different variance estimators (section 3.4.2). Two histograms were added to the *TrackingMultiplet* module, which was also provided by Corryvreckan, to produce projection images of particle beam attenuation (section 3.4.2). Finally, a residual range imaging workflow was created with two new modules that load and process residual range measurements (section 3.4.2).

Track-Based Multiple Scattering Imaging

Imaging based on scattering in the phantom was carried out with the Corryvreckan module *AnalysisMaterialBudget*. This module created a projection image at the center of a scattering body, by evaluating the amount of scattering for all tracks that intersected the imaging plane, grouped by the pixel that each track passed through. Only multiplet tracks were supported by the module, since the signal being measured was the direction change of each track. Image values of all the pixels were evaluated as the width of the distribution of scattering angles associated with each pixel. The evaluation originally provided by Corryvreckan was the average absolute deviation of the inner 90 % of scattering angles, as suggested in Jansen and Schütze [61].

The module was modified to support the use of squared scattering angles and other evaluations of the distribution width. A new parameter that allowed to select the desired evaluation method was added to the module. While the parameter defaulted to the original method if no explicit value was configured, it also enabled a newly added evaluation based on the median value of squared scattering angles; a method that was previously used by Plautz et al. [95], Ulrich-Pur et al. [87] and throughout this work because it yielded results closer to theoretical expectations. Instead of collecting both of the scattering angles θ_x and θ_y in a single collection with twice the size, the angles were combined to yield $\theta^2 = \theta_x^2 + \theta_y^2$. In each pixel the square root of the median value of combined scattering angles was selected as the image value.

Besides the imaging method parameter – which was set to *median_squared* – only two other parameters were configured for this module. The image size was set to 50 mm × 25 mm and the cell size (original term for pixel size in the module) to 500 µm × 500 µm, while keeping other parameters at their default values.

Attenuation Imaging

Unlike multiple Coulomb scattering, which mostly causes small angle deflections, nuclear interactions can divert a particle so much that it is no longer registered in the rear tracking stage. This is utilised in attenuation imaging, which links the transmission rate of particle beams to the location within a sample to visualise the spatial distribution of linear inelastic cross-sections. In such an analysis, the upstream and downstream rate would be counted and correlated with the paths of each particle. Therefore, a triggering system would be located in front of the sample, so that all upstream particles could be accounted for. Although this layout was not used with the demonstrator at MedAustron – triggering scintillators were placed after the rear tracker, to reduce the overall amount of multiple Coulomb scattering – it was still possible to acquire projection images of the attenuation of proton beams due to the scintillators being larger than the tracking sensors.

Only minor changes to the Corryvreckan module *TrackingMultiplet* were necessary to add support for an imaging workflow based on attenuation imaging. The original version of the module first attempted to find upstream and downstream track candidates separately, and then matched them with each other to yield one multiplet track for a matching pair of candidates. If no downstream candidate was found for an upstream candidate, then the upstream candidate was simply dismissed without producing a multiplet. This method of identifying track candidates and matching them was not changed for attenuation imaging; rather, additional histograms were added to it.

In total, three two-dimensional histograms were added, two of which were filled during the per-event analysis, and one was constructed from these two after the analyses ended. During the analysis, one histogram was filled with the total upstream fluence, i.e. the number of upstream track candidates intersecting each histogram cell. The intercept position of the upstream track on the scattering plane was used to determine which histogram cell was filled, for both of these histograms. This is similar to how *AnalysisMaterialBudget* matches image values (width of the distribution of scattering angles) to cells, only without the contribution of a downstream track. To control the area of the histograms and their cells, two more two-dimensional parameters – cell size and image size – were added to *TrackingMultiplet*. Note that the behaviour of these parameters was designed to be identical to the same parameters in the *AnalysisMaterialBudget* module.

Similar to the total fluence histogram, a second histogram called lost fluence counted the number of upstream candidates that failed to match with a downstream track in each cell. Finally, a third histogram representing the attenuation

image was derived from the other two after all events in the run were handled during the analysis. Each cell value of the final image was evaluated as the negative logarithm of the transmission rate

$$\text{image}(x,y) = -\ln\left(\frac{\text{total}(x,y) - \text{lost}(x,y)}{\text{total}(x,y)}\right) = -\ln\left(1 - \frac{\text{lost}(x,y)}{\text{total}(x,y)}\right). \quad (3.3)$$

Residual Range Imaging

Two additional modules were added to support an imaging workflow based on residual range: an event loader for range measurements, called *EventLoaderTera*, and an analysis to correlate them with tracks and produce projection images, called *AnalysisEnergyLoss*. Both modules are based on an original analysis of Ulrich-Pur [96], which was rewritten to integrate with Corryvreckan.

For each event, the *EventLoaderTera* module stored the residual range of the particle on the clipboard. Because Corryvreckan was not designed to support the concept of energy measurements, these residual ranges were instead put into the charge-property of a cluster with no position measurement. To prevent the use of such pseudo-clusters during tracking or alignment a detector role of device under test (DUT) was configured for the calorimeter.

It was required that the loader only stored the residual range when the tracking data had a matching trigger number, so that tracks could be properly correlated. One parameter *trigger_overflow_size* was added to both loader modules to allow a configuration of the limited length of trigger numbers; which was 15 bit (32 767) with the demonstrator system. After counting to the maximum number of bits the trigger unit would start at 0, which occurred several times during a single acquisition. Each loader separately kept track of overflows to obtain a non-overflowing 32 bit trigger that was used to pair measurements. The tracker loader created events and stored them on the clipboard, together with the tracking clusters, whereas the calorimeter loader retrieved events and, if the trigger numbers matched, additionally added a pseudo-cluster containing the residual range.

A parameter *first_slice_threshold* – usually set to a value of 4 MeV – was used to suppress events with a signal in only the first of the scintillators. Another parameter *higher_threshold* – set to 2.5 MeV – determined the residual range of each event. The last scintillator from the front that was above this threshold was selected as the range.

Finally, a module *AnalysisEnergyLoss* was written to determine the position resolved residual range of a phantom. The module featured the same parameters *cell_ size* and *image_ size* that were previously used in the *AnalysisMaterialBudget* and the modified *TrackingMultiplet* to configure the two dimensional histograms corresponding to the projection images. A parameter *minimum_ cell_ content* was used to set pixel values to 0 if less tracks intersected than the parameter value intersected the cell; it was usually set to 5 tracks.

During an analysis the module simply attempted to load a single multiplet and the pseudo-cluster of the calorimeter. In events that had both, the module calculated the projected position at the scattering plane and filled in the pseudo-clusters charge value; which actually stored the residual range. A second histogram kept track of the number of multiplets intersecting each pixel. At the end of an analysis, each projection histogram cell was set to zero if there were less than the minimum cell content tracks. Otherwise, the filled value was divided by the number of tracks to yield the mean residual range in the pixel.

3.5 Estimating Image Resolution with Monte Carlo Simulations

Image resolution of any ion imaging scanner is closely tied to multiple Coulomb scattering, since the particles undergo many interactions within matter, consequently changing their direction in the process. Due to the stochastic nature of multiple scattering it is not possible to obtain the original trajectory of, say a proton traversing a patient, by measuring the entry and exit tracks. Several models have been used to reconstruct single particle paths within a patient with varying degrees of accuracy, such as a straight line from entry to exit, two straight lines with a single kink [61], cubic splines [62, 64], or the concept of MLP – the established standard model in ion imaging, which has seen several implementations in the literature [43, 63, 65, 97, 98].

The intrinsic uncertainty of such path models has been investigated based on Monte Carlo simulations, which allow a direct comparison between a model and the actual path of a particle. Cuts on the distributions of energy loss and scattering angle [43], or filters based on the energy deposition in a staged calorimeter [99] have been investigated. Different ion species were compared [65], and material inhomogeneities in the phantom or patient were taken into account [66, 100, 101]. While these works focused on the MLP within a phantom only, others additionally took external uncertainty sources into account, such as the detector parameters

of the trackers [14, 102] and the geometry of phantom and detectors [13, 14, 103]. For example, it is important to keep the detector material budget small, since scattering in the trackers introduces a non-zero uncertainty in the reconstructed surface positions and directions [14, 102, 104]. These surface uncertainties reduce the accuracy of the MLP within the phantom and can lead to a worse radiographic image resolution. Thus, only the lowest necessary amount of tracking planes – typically four – is generally considered in ion imaging. In this work, the impact of two additional tracking planes on the MLP uncertainty was explored by comparing uncertainty envelopes of set-ups with four and six tracking planes obtained through Monte-Carlo simulations.

In addition to the number of detectors in a set-up, detector attributes were also studied together with the other parameters. System parameters can amplify each others' influence on the MLP uncertainty. Therefore, it is useful to take into account how combinations of parameters influence uncertainty [104, 105]. For example, a detector developer might be interested in the expected image resolution achievable with a hypothetical new sensor. Thus, a comprehensive comparison of system parameters and their influence on MLP uncertainty in a water phantom was carried out in an analysis based on Monte-Carlo simulations. System geometry, detector properties, different beam energies and particle species were taken into account to cover a large part of the parameter space. Image resolution was summarised as a function of these parameters and intervals in terms of position resolution and material budget useful for ion imaging were identified. These could serve as a guide for decisions regarding the requirements of potential new hardware developments. This comparison was previously made available in a preprint and therefore closely follows the work presented in Burker et al. [106].

It is worth mentioning that analytical methods have previously been used instead of the Monte-Carlo method, to study the influence of external parameters [104] or compare different types of imaging setups in terms of image resolution [55]. Using such models allows to study a large parameter space with much less computing time, since no particle transport or interactions would have to be simulated. Simulations were still preferred for this work, since they do not disregard the detrimental effects of nuclear interactions on the MLP uncertainty, yielding slightly more realistic estimates. Furthermore, preferring simulations allows to analyse individual events in the same way as a real measurement would have been processed. This enabled to easily use the GBL model for tracks in air and the detectors, since it was already implemented for telescope analyses. It also enables potential concretisation of the simplified and idealised simulation in future upgrades, to reproduce a more realistic system: the detector boxes could be replaced by real sensors with passive material that impacts the measurement, or with misalignments in detector

locations and rotations.

3.5.1 Path Simulation

As can be seen in figure 3.15, the simulation layout for path uncertainty studies was designed to be a simplification of single particle tracking setups [53].

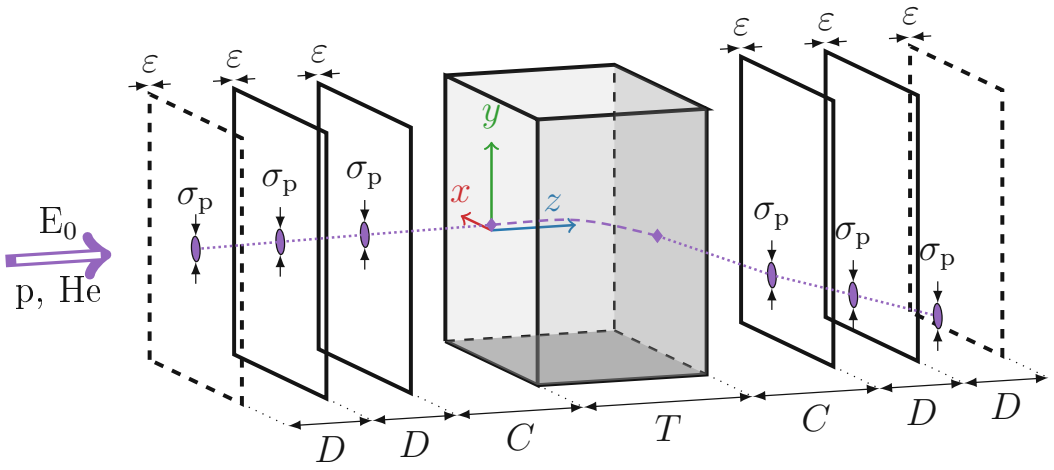

Figure 3.15: Layout of the path uncertainty simulations. A homogeneous water phantom with thickness T is surrounded by pairs or triplets of tracking detectors, each of which has a material budget ε and a position resolution σ_p. Upstream or downstream tracking detectors are separated by a distance D and a clearance C keeps the phantom apart from the inner detectors.

A uniform water box, referred to as phantom, was placed such that its front surface is located at the origin. It was subdivided into 1 mm thin slices and had a sensitive detector attached to it so that particle positions in the x- and y-direction as well as energies could be sampled. Through this sampling, the path and energy loss within the phantom was recorded for each of the particles. Two tracking stages were located upstream and downstream of the phantom, each of which consisted of either two or three detector planes. Each plane had a sensitive detector attached to it, to record the local positions and energies of particles interacting with the detector. A point source in front of the first upstream plane created primary particles aimed at the phantom. All simulations considered 5×10^5 primary particles. One single simulation used the *G4EmStandardPhysics_ option3* physics list, which considered standard electromagnetic physics processes such as bremsstrahlung, pair production, multiple scattering, nuclear stopping, ionisation and energy loss of ions. It was used to compare the effectiveness of 3σ cuts on scattering and energy loss

Table 3.1: Parameters in the path simulation (top) and uncertainty analysis (bottom) and their ranges of values.

Variable	Name	Value interval	Default value	Unit
n	Number of planes	2 or 3	2	-
D	Detector distance	25 to 300	100	mm
C	Clearance	100 to 300	300	mm
T	Phantom thickness	100 to 300	200	mm
ε	Material budget (x/X_0)	0.001 to 2	0.4	%
E_0	Initial Beam energy	200 to 500	200	MeV/u
p	Beam particle	Proton or Helium ion	Proton	-
σ_p	Position resolution	1 to 250	100	µm
-	Track model in air	SLT ($n = 2, 3$), GBL ($n = 3$)	SLT	-

to reduce MLP uncertainty between only electromagnetic physics and electromagnetic plus hadronic physics. To include elastic and inelastic hadronic interactions, all other simulations used the reference physics list *QGSP_BIC*.

Parameter Values

Many of the quantities describing a simulation were used as parameters, so that simulations could be repeated for different parameter values to study their influence on the path uncertainty (table 3.1). Whereas the materials and base areas of all box volumes were fixed, their thicknesses were varied between simulations, with values typically used in ion imaging. Air, silicon and water were used for the world, detector and phantom volume materials, and their extent was 500 mm × 500 mm. Added together the parameters that described the geometry were the number of planes, the distance D between detectors, the clearance C between the innermost detectors and the phantom surface, the phantom thickness T and the material budget ε of the detector planes. The phantom thickness was simply configured in mm, while the thicknesses of the detectors were given in % of the radiation length of silicon $X_0 = 93.7\,\mathrm{mm}$ [33].

Previous studies demonstrated how a small distance between the detectors of a tracking stage can increase uncertainty due to the lever on position resolution and scattering [107]. Distances larger than 50 mm were suggested to prevent issues due to such leverage [13, 104]. In contrast to distance, which reduced uncertainty, a larger clearance was found to be detrimental and an air gap as small as possible and as large as necessary – to safely operate the scanner – should be used [14, 53, 103].

Similarly, a smaller detector material budget is preferable since the amount of multiple scattering in the detectors can be reduced. A large maximum was deliberately chosen for material budget, so that not just sensor thicknesses used in ion imaging [14–18, 54, 108] would be covered, but also detectors that would feature additional structures in the beam, such as mounting or cooling.

Initial energy E_0 and particle species p were used as parameters for the beam. Helium ions were compared to protons in most of the simulations due to their reduced amount of multiple Coulomb scattering and potential for a better image resolution [65, 105, 109]. Other ions such as carbon – which is actively used for treatment at MedAustron – were left out to limit the parameter space to a manageable amount. Although a similar investigation could be performed for carbon ions, care should be taken to consider dose to patient as well, which is much higher in a carbon radiography [109]. Limiting the particles to protons and helium ions also allowed the use of only one interval of initial beam energies, since the ranges of both particles are similar (section 2.1.2). An often used energy for uncertainty studies with protons is 200 MeV, which is enough to traverse a water body of 200 mm representative of a human head [14, 43, 53, 62–65, 97, 98]. Although 200 MeV was used in an investigation of six plane set-ups to yield comparable results, most other simulations were carried out with a higher energy of 250 MeV – to fully traverse larger phantoms as well.

Finally, non-zero displacements were randomly sampled from a normal distribution with zero mean and a standard deviation of σ_p – a parameter called position resolution – and added to the position measurements. These displacement-terms were not added during the simulation. Instead, the positions were recorded with ideal accuracy and displacements were applied during event loading in the analysis, so that each of the simulations could be reused for several analyses with different parameter values of position resolution. The interval for position resolution values was selected so that existing sensors in proton CT scanners were included [14–18, 54, 108].

Comparison of Set-Ups with Four and Six Planes

Realistic detectors occasionally fail to respond to a particle due to dead-time, defect or noisy strips, or gaps between sensitive areas of the detectors (fill factor below 100 %). A single missing detector response in a four plane set-up would be enough to drop an event, since the direction of either the upstream or downstream stage would be undetermined. Therefore the detection efficiency of the tracking system would be ϵ^4, where ϵ is the detection efficiency of a single plane. The overall tracking efficiency could be increased when using three planes per tracking stage,

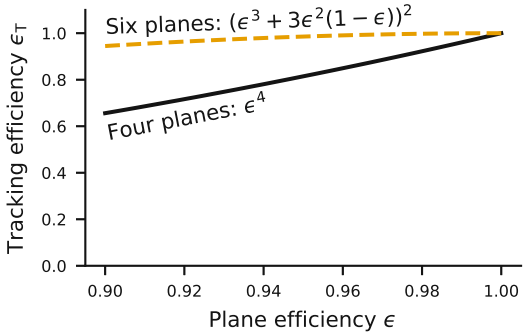

Figure 3.16: Tracking efficiency as function of the detection efficiency ϵ of individual planes, for four and six detector planes. A single missing hit in either of the upstream and downstream trackers is still acceptable for a six plane set-up to make use of an event.

since a redundant measurement allows one missing hit per stage (figure 3.16). In this case the tracking efficiency of one stage is the probability of having three measurements ϵ^3 plus the probability of exactly one missing hit for each plane: $3\epsilon^2(1-\epsilon)$. Since both stages must yield a track, the tracking efficiency is just the stage efficiency squared: $(\epsilon^3 + 3\epsilon^2(1-\epsilon))^2$.

While a six plane setup could potentially reduce the dose of an ion imaging scan, it is expected to yield a worse image resolution due to additional scattering in the detectors. Therefore, simulations of set-ups with two and three detectors per tracking stage were carried out and analysed to examine the differences in terms of MLP uncertainty. Particle tracks on each side of the phantom were modelled as SLT for both of the four- and six plane set-ups. Six plane set-ups were additionally analysed with GBL for the upstream and downstream tracks to investigate whether the GBL track model could improve MLP uncertainty.

A smaller parameter space was used for the six plane comparison, than for the comprehensive summary. An initial energy of 200 MeV/u was used with protons and helium ions to compare uncertainty envelopes for both particles. Four simulations with a phantom clearance of 300 mm, a detector material budget of 0.4 % and a position resolution of 50 µm were used to qualitatively assess uncertainty envelopes within the phantom. The mean RMSD of MLP positions along the phantom depth was then used as a figure of merit. It was explored in three sets of simulations, each of which varied one parameter of clearance, material budget and position resolution, while keeping the others constant. Constant values of clearance, material budget and position resolution were 300 mm, 0.4 % and 50 µm, while their parameter intervals were 100 mm to 400 mm, 0.2 % to 2 % and 1 µm to 250 µm, respectively.

Comparison of Path Models in a Small Aluminium Phantom

One additional simulation was carried out to compare the performance of different path models while matching the parameters of the imaging data sets with the demonstrators (section 3.4). The simulation was analysed with the linear, single kink, simple spline and most likely path models. A 10 mm thick aluminium slab was used as phantom to match the material of the imaging data sets. Other system parameters were selected to roughly replicate the environment of the measurements too: distance and clearance were set to 50 mm, energy to 100.4 MeV, material budget to 0.32 % and position resolution to 28.87 µm.

3.5.2 Most Likely Path Uncertainty Analysis

The uncertainty analysis was carried out using a modified version of the Corryvreckan framework. An overview of the analysis for one simulation is laid out in figure 3.17. Each simulation was processed twice; once, to calculate the distributions of scattering angles and energy losses between the tracking stages, and a second time to apply cuts based on these distributions and obtain the RMSD curve of the remaining events. The modules involved were an event loader for the simulation data, a slightly modified *TrackingMultiplet*, one module to calculate and apply data cuts and an analysis module for building the MLP at each event and evaluating the RMSD.

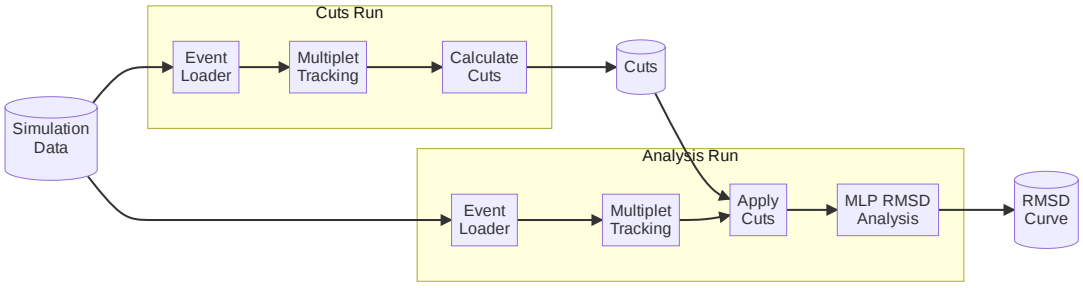

Figure 3.17: Modules used in the most likely path analysis. In a first run, distributions of energy loss and scattering angles of the tracks are calculated. These are used to apply 3σ cuts in the analysis run.

Two additional classes were added to the Corryvreckan *objects* library so that instances for the sampled, simulated path and a MLP model could be stored on the clipboard. The sampled path was merely a storage for the energy and position measurements within the phantom and was supposed to be filled by the simulation loader. Since the MLP model relies on particle charge, the radiation length of the

target material and a parameterisation of the energy loss as function of depth in the material, its object internally stored charge and radiation length and a class for loading the parameterisation. All three of these members were supposed to be set by the RMSD analysis module. The parameterisation was constructed once at the beginning of each analysis, by reading in the simulation output and evaluating the mean kinetic energy as function of phantom depth, using the sampled energies of each event. At each depth, the product of velocity βc and momentum p was calculated using kinetic energy and the particle rest energy m_0c^2. Following the method of Williams [63], which has been commonly used to parameterise MLP calculations [43, 64, 65, 97, 98, 104], a fifth order polynomial was fitted to this curve and the coefficients a_i were stored in the MLP object for the duration of the analysis

$$\frac{1}{(\beta cp)^2}(z) = \left(\frac{E_{\text{kin}}(z) + m_0c^2}{E_{\text{kin}}(z)\left[E_{\text{kin}}(z) + 2m_0c^2\right]}\right)^2 \approx \sum_{i=0}^{5} a_i z^i. \tag{3.4}$$

Additional modules carrying out the individual work steps were also added. These comprise a loader class *EventLoaderPathSimulation*, one class to calculate and apply data cuts and a class for the RMSD analysis of MLP estimates.

Event Loader

The *EventLoaderPathSimulation* module was developed as a custom loader class to store clusters for each of the detector measurements on the clipboard. Position measurements from the simulations were given in *global* coordinates and *local*, *row* and *column* values were obtained using the transformation matrices of the detector instances. Although the *raw* signal was originally intended to store the energy deposition in a detector, it was instead filled with the local particle energy from the simulations. This way the following data cut module could approximate the energy loss as if initial beam energy and residual energy were available, by taking the *raw* cluster signals.

Three parameters *infile*, *xml_ config* and *apply_ error* were used to configure the file path to the simulation output, the file path to the configuration of the simulation and whether or not random displacement should be applied to the cluster positions to simulate position resolution, respectively. In analyses where the loader was configured to apply errors, the class sampled random numbers from a normal distribution with zero mean and a standard deviation equivalent to the spatial resolutions of each detector, which were configured in the detectors file. These displacements were added to the global positions prior to storing it in the cluster

instances. Finally, the loader also read path samples within the phantom from the simulation output and stored them on the clipboard as well.

Multiplet Tracking

A small modification was applied to the *TrackingMultiplet* module offered by Corryvreckan. The *momentum* parameter was separated into two parameters *momentum_upstream* and *momentum_downstream*, to support energy loss between the tracking stages. Both parameter values were configured per simulation, based on the mean kinetic energies $E_{u,d}$ measured at the innermost detector planes and, with the rest mass m_0, were calculated according to

$$p_{u,d} = \sqrt{E_{u,d}^2 + 2m_0 E_{u,d}}, \tag{3.5}$$

which was given in MeV/c.

For the analysis of simulations with four detector planes, only SLT was used as track model at each tracking stage. Simulations with six planes were analysed twice, using SLT and GBL, to test the feasibility of GBL in an ion imaging context.

Data Cuts Module

Cuts can be applied to ion imaging data sets, to improve the image resolution [43] and density resolution [29] of a scan. A new module *DataCutProtonCT* had to be developed so that Corryvreckan could support the concept. The class was designed for a dual use of both calculating the underlying signal distributions (energy loss and scattering angle) and applying cuts based on those distributions. One parameter *distribution_file* was added to switch between the two uses. In analyses where a distribution file was specified, the module loaded previously calculated distributions from this file and applied the cuts, filtering out events. Otherwise, the module defaulted to evaluating the distributions instead, which it stored in the Corryvreckan *histograms_file* for another analysis to load.

Two other parameters *last_front_detector* and *first_back_detector* configured the names of the innermost detectors – i.e. the planes facing the phantom. The module used the *raw* signal value of clusters at these detectors – which actually contained the local energy due to the simulation event loader – to calculate the energy loss between the tracking stages. Additionally, it evaluated the distributions of kink

angles by loading multiplet tracks from the clipboard and calculating the differences in direction between the innermost detectors. Since kink angles in the x- and y-directions are not correlated, they were combined in a single distribution with twice as many entries. For runs where the module evaluated distributions, these were simply stored. Otherwise, energy loss and kink angles were compared to the loaded distributions at each event to determine whether the event had a measurement further away than three standard deviations (3σ) from the corresponding distribution mean (figure 3.18). Events outside this 3σ-interval were rejected for the analysis by returning a `StatusCode::DeadTime` from the module's `run` method, causing the module manager to continue with the next event instead of calling the next module.

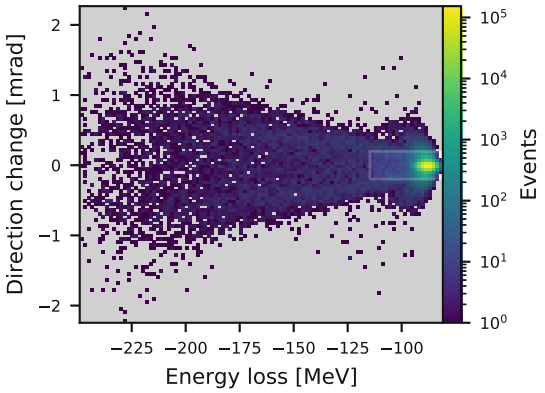

Figure 3.18: Data cuts on energy loss and direction changes for a simulated set of proton tracks. Events in the shaded area corresponding to more than a 3σ-deviation of the mean energy loss and direction change were not processed during the rest of the analysis.

Uncertainty Envelope Analysis

The final work step in the analysis was implemented in another custom written module *AnalysisModelRms*, which estimated MLP paths for each event and compared the estimates to the sampled positions. Per event, it loaded a multiplet track and the ground truth path within the phantom from the clipboard. Multiplets were used to evaluate the MLP between the entry and exit points of the phantom. Since the phantom surface was known in this experiment – due to it being a simple box volume – no representation of its hull was necessary for ray tracing. Instead, the z-coordinates of the beginning and end of the sampled ground truth path were used to evaluate the boundary conditions for the MLP estimate – i.e. the intercept positions and directions at the entry and exit z-coordinates. Both track models used in this experiment were linear, with SLT being a single straight

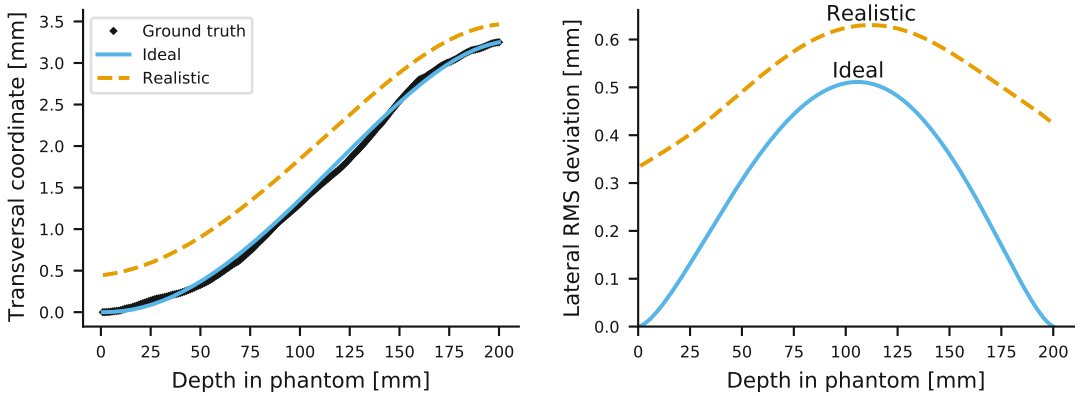

(a) (b)

Figure 3.19: (a) Comparison of the x-coordinate of one simulated proton path through the phantom with ideal and realistic position measurements. (b) The root-mean-square deviation (RMSD) of many simulated proton paths and their MLP estimates, for ideal and realistic position measurements.

line and GBL being segmented into several lines with kink angles at the detector planes. For a tracking stage with N planes, the GBL model would yield $N-1$ lines with $N-2$ kink angles, since no more measurements are available prior to the first and after the last detector. Thus, the boundary conditions were evaluated as the directions at the innermost detectors and a linear extrapolation to the phantom surface. Positions at the phantom surface were not generally reproduced in the analysis, due to uncertainties in the measurements such as position resolution and scattering in the detectors (figure 3.19a).

Following the evaluation of the boundary conditions, the MLP model was estimated at each z-coordinate of the ground truth path samples. The quadratic difference between estimated and ground truth positions was summed up for all events and converted to RMSD at the end of the analysis (equation (2.8)), at each z-coordinate, yielding a single depth-dependent uncertainty envelope per analysis. Compared to an ideal case, where uncertainty was only driven by multiple scattering in the phantom, the realistic envelopes were significantly worse, with non-zero RMSD at the surfaces (figure 3.19b). Uncertainty at the exit was slightly higher than at the entrance, which can be attributed to energy loss within the phantom and, as a consequence, a worse downstream direction measurement.

The lateral spatial frequency $f_{10\%}$ corresponding to a decay of the modulation transfer function below 0.1 was selected as figure of merit so that the performance of hypothetical scanners can be compared in terms of their theoretically achievable image resolution [55, 105]. This also allows to compare simulation parameters to

resolutions measured by reconstructing phantoms with line-pair or edge inserts [56, 62, 64, 68–70]. As described by Krah et al. [55], $f_{10\%}$ can be derived from the depth dependent RMSD

$$f_{10\%} = \frac{\sqrt{2\ln 10}}{2\pi}\frac{1}{\mathrm{RMSD}}. \tag{3.6}$$

Since the image resolution depends on the depth within the phantom, usually the mean value in the z-direction is used to represent a system's resolution. In this work, however, the maximum value in z was used instead, because it yielded a more conservative *worst-case* result useful for testing requirements of new detectors.

4 Results

4.1 Results with the DSSD Tracking Telescope

Results with the first telescope were previously published in Burker et al. [91], however, the framework for reconstruction in this publication was EUTelescope [110, 111] which was replaced by Corryvreckan for this work. Although there were differences in the workflow and results, these were minor overall and the same conclusions could be drawn when using either of EUTelescope or Corryvreckan.

Pre-irradiated sensors were used as components in the first generation telescope. This is evident in the geometric distributions of 252.7 MeV clusters COG on each sensor (figure 4.1), where gaps in the beam profiles reveal that many strips could not be utilised due them being dead or masked for excessive noise. Nevertheless the system could be aligned and an image of a phantom was obtained based on multiple Coulomb scattering.

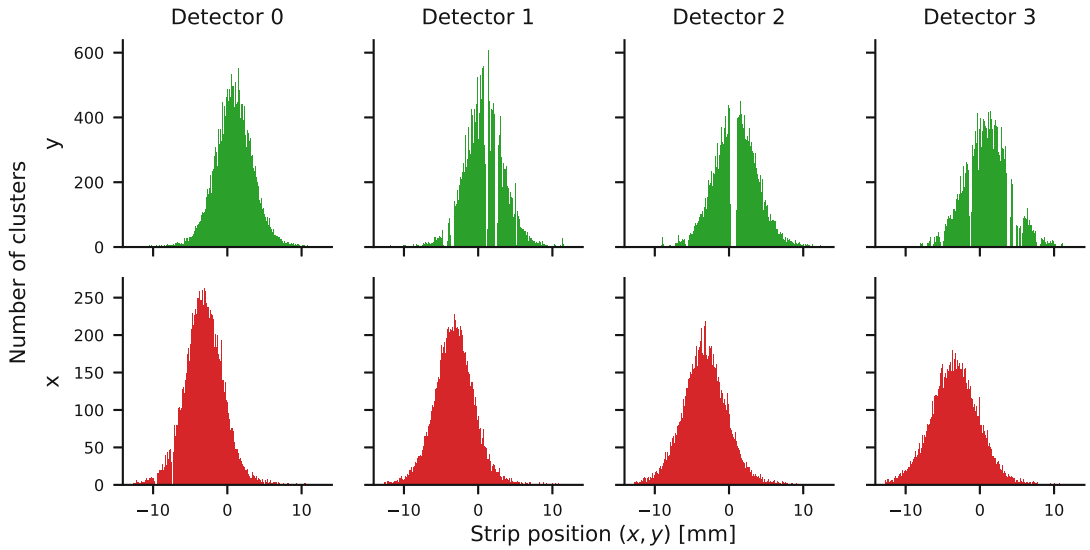

Figure 4.1: Geometric distributions of clusters on each sensor of the first generation telescope, from a 252.7 MeV proton beam.

A prealignment based on the correlations of clusters on each plane with clusters on the first (reference) plane was carried out to obtain an initial guess for the tracking-based alignment (figure 4.2). An ideal correlation for perfectly aligned sensors would have been characterised by 45° lines for forward-directed tracks.

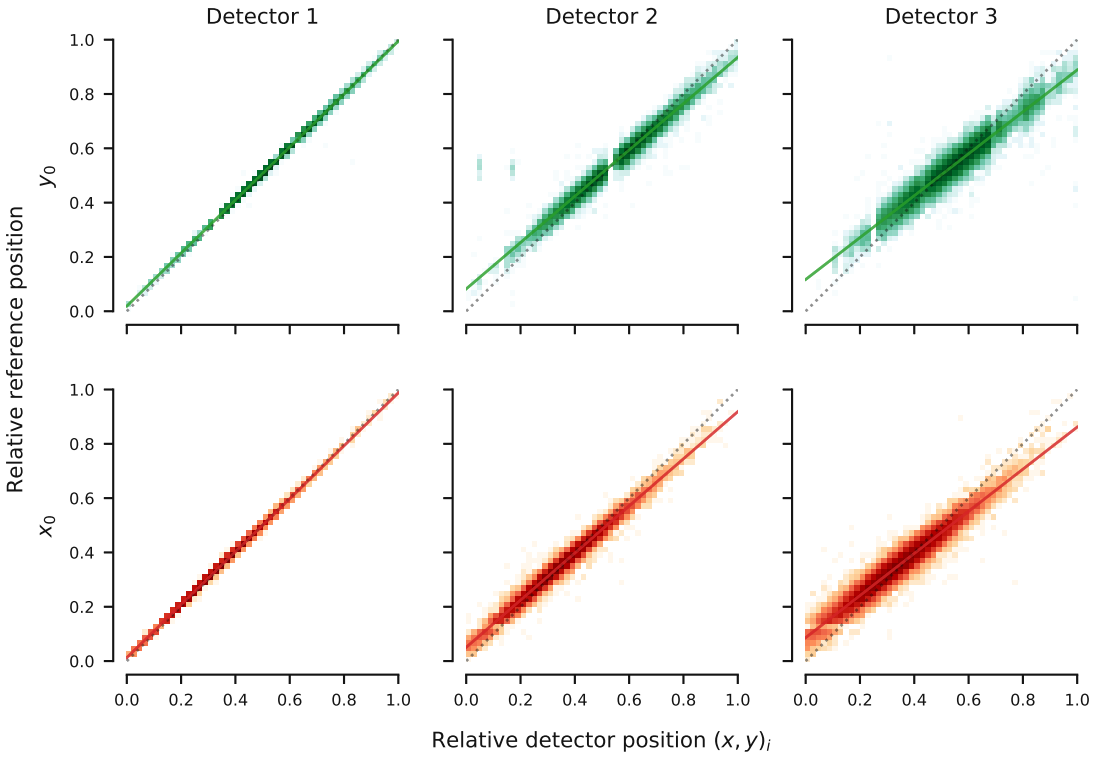

Figure 4.2: Correlations of cluster positions on the first (reference) detector plane with the other planes, normalised to the width and height of the sensors. Dotted 45° lines through the origin indicate an ideal correlation and coloured lines are linear regressions of the data.

Data points in the correlation-plots were however distributed over an area around these ideal lines, with an increasing width for sensors further downstream; a consequence of multiple Coulomb scattering and beam divergence and not misalignment. Two other observations could however be explained by a misalignment of the sensors. Regression lines were vertically shifted with respect to the 45° lines, which indicated translational offsets of the detector planes, relative to the reference plane. These offsets were corrected during prealignment, by shifting the sensor planes so that the correlations would be centered on the 45° lines. Additionally, slope angles that differed from 45° were observed in the data point distributions, indicating non-zero rotations of the detectors. These were not corrected during pre-alignment, since the three rotations could not be easily separated from another.

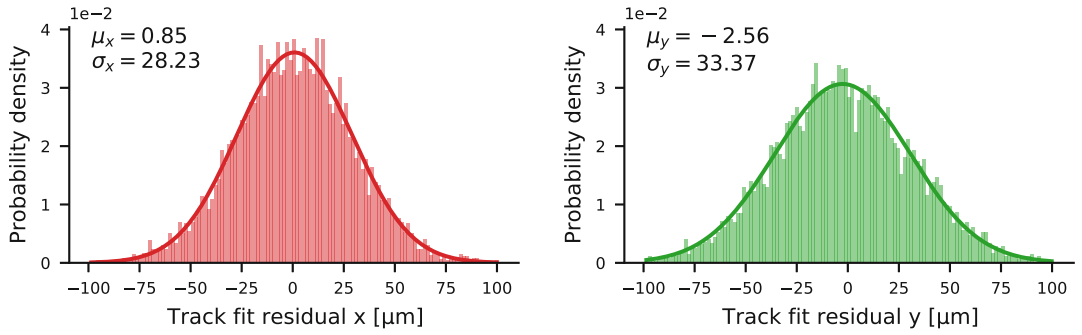

(a) (b)

Figure 4.3: Residual distributions on the first detector plane for the (a) x- and (b) y- coordinates. Mean and standard deviation of a fit to a normal distribution are annotated on the upper left of both graphs.

An alignment procedure based on an ensemble of 252.7 MeV tracks was used to correct detector translations and rotations. The procedure minimised the distribution of the track χ^2-statistic, by shifting and rotating the detector planes and re-fitting the tracks iteratively. Afterwards, the residuals of track intercepts and actual measurement positions on each plane were centered around zero (figure 4.3). Normal distributions were fitted to the residuals to summarise the track fitting accuracy of all detectors in the telescope, together with the χ^2-statistics (figure 4.4).

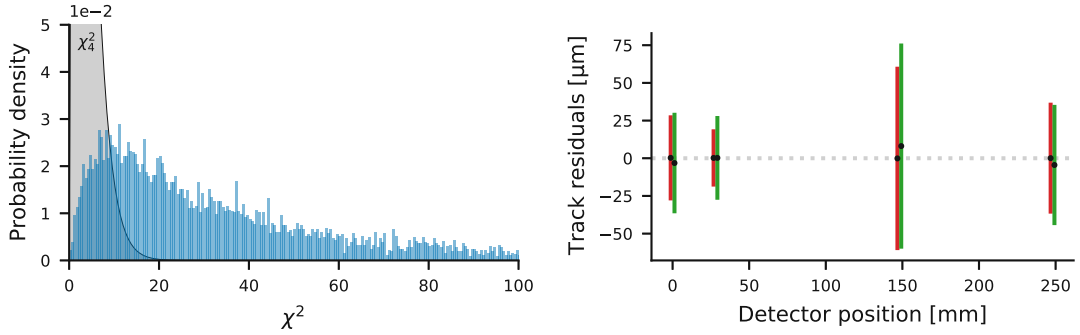

(a) (b)

Figure 4.4: (a) χ^2-distribution of track fits for the first generation prototype, using 252.7 MeV protons and the straight line track model in air. The grey area outlines the theoretical χ^2-distribution for four degrees of freedom. (b) Normal distribution fits to the residuals on all detector planes for the x-(red) and y-(green) coordinates. Points and bars indicate the means and standard deviations, respectively, of the fitted normal distributions.

It is evident that the theoretical χ^2-distribution with four degrees of freedom – 8 position measurements (x_i, y_i) minus 4 fit parameters (k_x, k_y, d_x and d_y) – was not replicated by the data. Additionally, the residual widths were larger than the expectations of 14.43 µm and 28.87 µm due to the strip pitch for the x- and y-coordinates, respectively. For example, σ values of 60.84 µm and 68.06 µm were obtained through normal distribution fits to the x- and y-residuals of the third detector. Both of these results suggested that the expected position resolution could have been too low. Given that the energy used was quite low and multiple scattering in the sensors would be significant, a more likely explanation would be that a SLT through all four planes was an inadequate model.

Using approximately 3.3×10^5 single particle events of a 100.4 MeV proton beam, a single multiple scattering projection of an aluminium mounting hub with threaded holes, and nylon screws and iron set screws was acquired (figure 4.5). Though the beam did not cover the entire phantom it was still possible to clearly display the phantom and distinguish its different materials. A more detailed analysis into image resolution or contrast was not carried out with this system, since it was replaced with new sensors that were not previously irradiated and no suitable calibration was available.

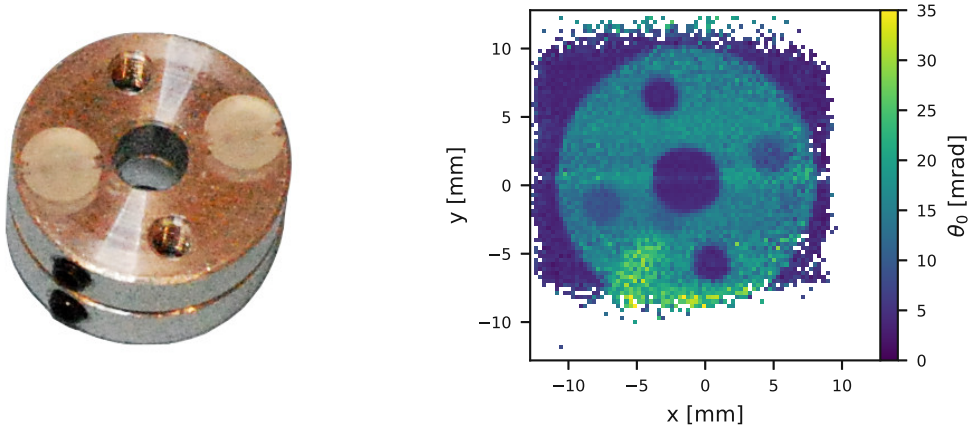

(a) (b)

Figure 4.5: (a) Photograph of an aluminium mounting hub with plastic and iron screws, which was used as a phantom. (b) Multiple scattering radiography of the mounting hub phantom. The distribution width of kink angles in each 300 µm × 300 µm pixel was measured with a 100.4 MeV proton beam.

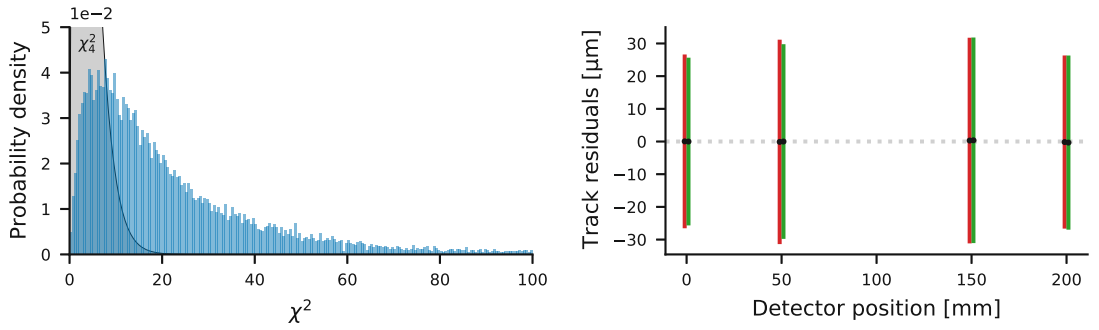

(a) (b)

Figure 4.6: (a) χ^2-distribution of track fits using the straight line track model in air. The black curve outlines the theoretical χ^2-distribution for four degrees of freedom. (b) Normal distribution fits to the residuals on all detector planes for the x-(red) and y-(green) coordinates. Points and bars indicate the means and standard deviations, respectively, of the fitted normal distributions.

4.2 Results with the Full Demonstrator System

Following the initial results with the squared tracking telescope, a second demonstrator was constructed using sensors that were not previously irradiated. The characteristics of the new sensors were similar to those of the first iteration, though their sensitive areas was twice as large since both of the sides had 512 silicon strips.

Track fitting results after a prealignment and alignment procedure were comparable to the first iteration telescope, with residual distribution widths of 26.34(40) µm for the first and last planes and 30.99(70) µm for the inner planes (figure 4.6). A difference in residual widths between the x- and y-components was not observed even though the detectors had unequal strip pitches among the components. Therefore, the residual widths did not yield the detector resolution but the uncertainty due to multiple scattering. Similarly, the χ^2-distribution of track fits did not reproduce the theoretically expected distribution with four degrees of freedom, which could mean that the position resolutions were underestimated or that the model of a single straight track was inadequate.

Since more than four detector modules were available with the new sensors it was possible to work with six planes per tracking stage. This allowed using GBL not just as the track model for the entire telescope, but also for each of its two stages separately. A simple comparison of the alignment quality was carried out using both of the SLT and GBL models for the telescope (figure 4.7), with four iterations for the χ^2-minimisation. Compared to a four plane telescope the track

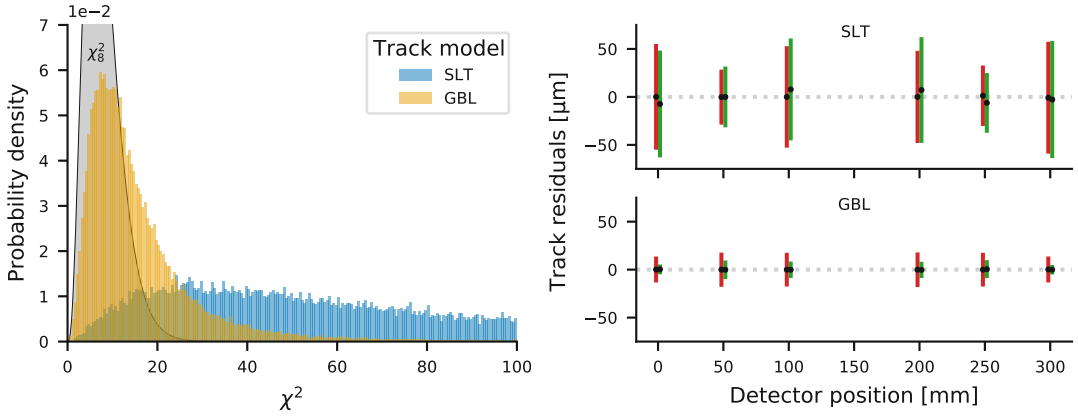

Figure 4.7: (a) χ^2-distributions of track fits using the straight line track (SLT) and general broken lines (GBL) models in air. The black curve outlines the theoretical χ^2-distribution for eight degrees of freedom. (b) Normal distribution fits to the residuals on all detector planes for the x-(red) and y-(green) coordinates. Points and bars indicate the means and standard deviations, respectively, of the fitted normal distributions.

fitting quality consistently worsened when SLT was used: the mean residuals were slightly offset from zero, distribution widths increased and the χ^2-distribution strongly differed from the theoretically expectation with 8 degrees of freedom. It should be noted that the alignment quality could probably be improved by hand, using several iterations of alignments with tighter cuts at each iteration. The SLT model would, however, likely be inadequate anyways, since a discrepancy between expectations and observations was already found with four detectors.

A less labour-intensive alignment that was also more accurate was obtained when GBL was used instead of SLT. Using GBL, the χ^2-distribution of track fits more closely reproduced the expectation. Residuals were properly centered on zero and their distribution widths more accurately reflected the differences between the sensor sides; with a larger x- than y-component (figure 4.7b). The inner four residual distributions were slightly wider – 17.74(16) µm in the x- and 9.01(54) µm in the y-direction – than those at of the very first and last detector, which had a σ of 13.51(4) µm in x and 5.05(6) µm. Overall, the position uncertainties were 16.33(200) µm in x and 7.69(192) µm in y. Even though these results reproduced the expected position resolutions of the sensors, it should be noted that the residual distributions were biased, since all planes contributed to the track fits. A proper measurement of the sensor resolution would need to use a telescope with higher resolution sensors and a layout similar to the set-up used in this work, but with a sensor under test placed in between the two tracking stages. Track fits from the tracking stages without considering the test sensor could then be associated with

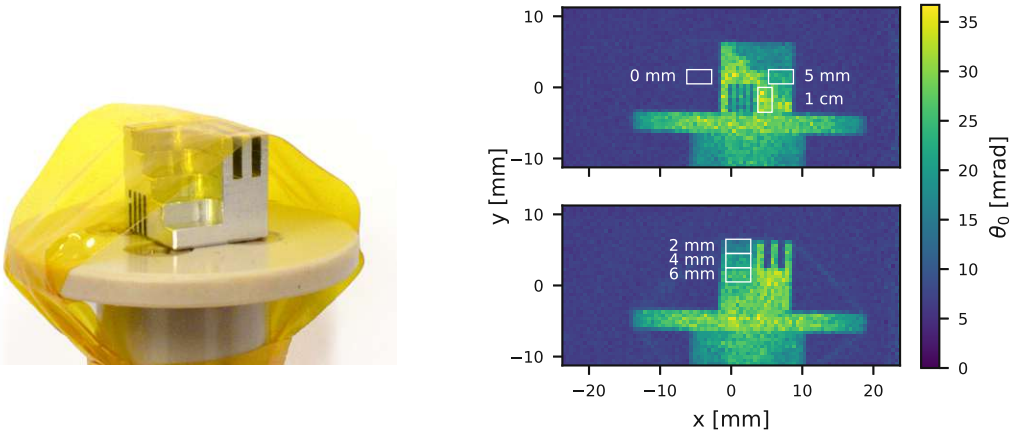

(a) (b)

Figure 4.8: (a) Photograph of the aluminium stair phantom with cutouts. (b) Multiple scattering projection images of the stair phantom, using beamtest data.

measurements on the test sensor to yield unbiased residuals corresponding to the sensors position resolution.

4.2.1 Multiple Scattering Imaging

A Corryvreckan based analysis was used to transform raw beamtest data into many two-dimensional projection images of a phantom. Particle tracks were reconstructed and associated with those pixels that the tracks intersected in a plane through the phantom. Each pixel thus displayed the amount of beam widening due multiple Coulomb scattering in the phantom material for tracks that passed this pixel at the phantom plane. Data from beamtests at MedAustron was used to create images of two aluminium phantoms, one of which had stairs and trenches (figure 4.8a) and the other one of which had stairs only. The results have been published in Ulrich-Pur et al. [87].

Stair Phantom with Trenches

Due to the limited readout rate of the tracking detectors and the shift-schedule at MedAustron only three projection images could be recorded of the phantom with trenches, two of which are displayed in figure 4.8. Several regions of interest were annotated in the image; these correspond to a known material thickness and were

Table 4.1: Expected and observed scatter distribution widths for each material thickness. Mean measurement angles were reduced by the mean background, while the standard deviations were added together.

Thickness [mm]	Expectation [mrad]	Observation [mrad]
background	8.48	7.24 ± 0.34
2	9.27	8.26 ± 1.70
4	13.73	13.26 ± 2.09
5	15.62	15.08 ± 2.09
6	17.40	16.79 ± 2.38
10	23.81	23.93 ± 3.03

used to compare observations to the expected amount of scattering for each of the thicknesses.

The pixel image values within each of these areas were summarised in table 4.1 and compared to the expected amount of scattering according to equation (2.4). Expected values were calculated in the same way as in Ulrich-Pur et al. [87]. Since equation (2.4) contains an energy dependent term βcp, the energy in the regions of interest was approximated as a geometric mean $\overline{E}_t = \sqrt{E_0 E_t}$ of the initial energy E_0 and the energy after passing through a thickness t of aluminium. The energy E_t was transported numerically, by dividing the thicknesses t into thin slices dt and using the stopping power $S(E)$ to update the energy at each slice i, beginning with the initial energy

$$E_i = E_{i-1} - S(E_{i-1}) \times \mathrm{d}t. \tag{4.1}$$

The final energy was converted to the term βcp according to

$$\beta cp = E \frac{E + 2m_0c^2}{E + m_0c^2}, \tag{4.2}$$

where (βc), p, E and m_0 are the velocity, momentum, energy and rest mass of a proton.

While the method in Ulrich-Pur et al. [87] was equivalent to the one described above, the analysis in it was performed with an entirely custom made Corryvreckan module. This module has since become obsolete due to the introduction of the modules *TrackingMultiplet* and *AnalysisMaterialBudget* in Corryvreckan, which were used instead throughout the work at hand. Thus, the observations differed slightly due to small differences in the tracking and pixel association logic. Within the statistical uncertainty due to noise, the observations and expectations displayed

good agreements with both of the custom made module as well as the adaptation of *AnalysisMaterialBudget*.

Stair Phantom

The second stair phantom (without trenches) was used in beamtests in October, 2020. Since the data could be read out with a gigabit ethernet connection instead of the previously used VME bus, a much higher readout rate was achieved. Additionally, a smaller beam spot size was used with an increased particle rate. Thus, it was possible to record 79 projections of the phantom, each of which contained at least 2.5×10^5 events.

Similarly to the phantom with trenches, the Corryvreckan workflow was used to create projection images, separate for each rotation angle. Afterwards all of the projection images were reconstructed into a three dimensional tomogram. Two three-dimensional contour surfaces of the tomogram were rendered (figure 4.9b) to visually separate the rotating table from the phantom. Contours for the rotating table (blue) and the phantom (orange) were obtained using levels of 0.35 mrad/mm and 0.65 mrad/mm, respectively.

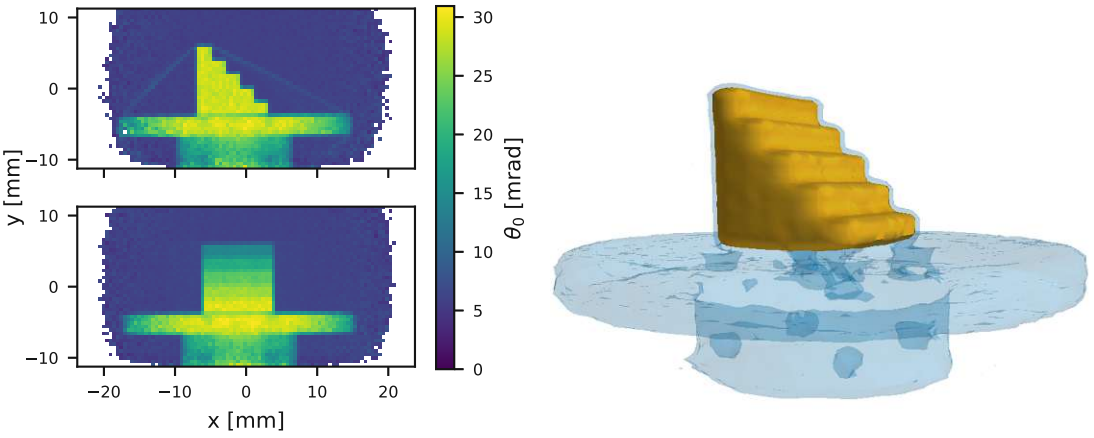

(a) (b)

Figure 4.9: (a) Multiple scattering projection images of the stair phantom, using beamtest data. (b) Three-dimensional contour surfaces of the phantom, excluding (orange) and including (blue) the rotating table.

4.2.2 Attenuation Imaging

Using a small modification of the Corryvreckan module *TrackingMultiplet* it was possible to obtain two dimensional projection images with the attenuation of the primary beam between upstream and downstream tracker pairs (figure 4.10). Given the same data, several drawbacks became evident when attenuation projections were compared to multiple scattering projections.

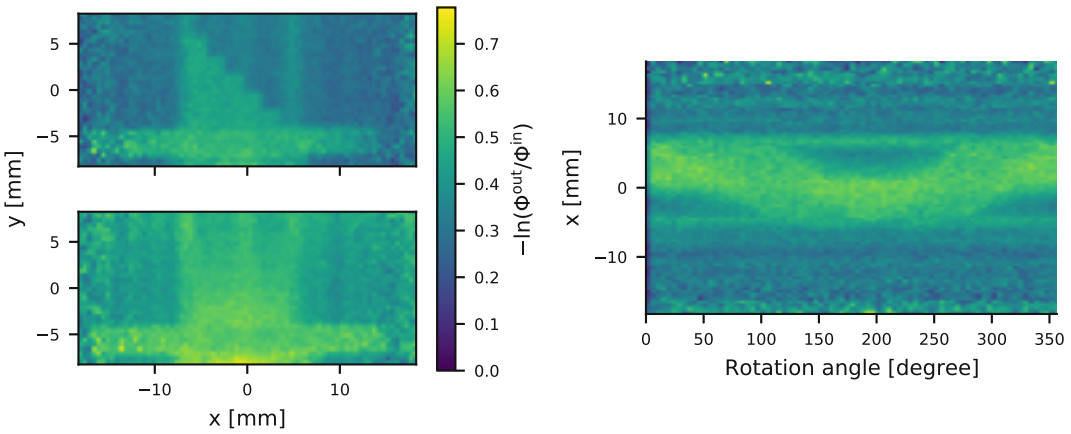

(a) (b)

Figure 4.10: (a) Attenuation projection images of the stair phantom, using beamtest data. (b) Sinogram of horizontal line profiles through the vertical center of the phantom ($y = 0$).

A much higher ratio of lost particles was observed for interactions close to the sensor edges of the upstream detectors. This effect was expected, since tracks at the edges were likely to scatter outside the sensitive areas even without nuclear scattering. It was not observed in other imaging modalities, since these did not consider events with a missing downstream track at all. Since the effect occurred far from the phantom, this problem could be removed by clipping the image to a smaller region of interest, prior to a image reconstruction.

Another drawback of the attenuation based imaging was the increased amount of noise compared to multiple scattering imaging or energy loss, which was expected due to the scarcity of (inelastic) nuclear interactions compared to the other mechanisms [46, 47, 71].

Finally, regular artifacts with a spatial frequency of approximately 3 mm were observed in the x-direction of the projection images. Artifacts were visible at every rotation angle and could be caused by detection efficiency differences at the

borders of 32-strip blocks. This was not investigated and could be dealt with in a more in-depth future study, however due to the elevated noise and artifacts no three dimensional reconstruction of the nuclear cross section was produced.

4.2.3 Residual Range Imaging

The calorimeter used during beam tests was operated such that slices were either activated above or below a threshold value. With this method it was possible to estimate each particles range as the last scintillator from the front with a signal above the threshold (figure 4.11), which would result in a range resolution in an order of magnitude corresponding to the thickness of a scintillator.

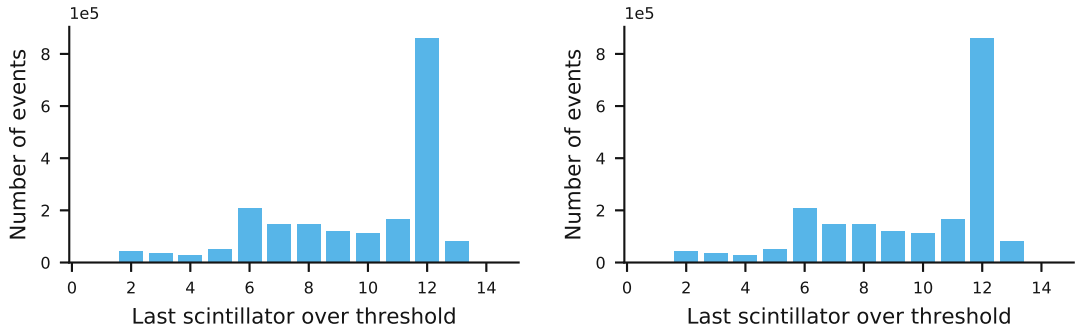

(a) (b)

Figure 4.11: Residual range of many 100.4 MeV protons at a phantom rotation of (a) 0° and (b) 90°.

Due to the unique trigger number generated during the synchronisation of both detector systems (section 3.3.2) it was possible to correlate individual energy loss measurements with individual particle tracks. This enabled an analysis to visualise the position resolved residual range at each phantom rotation (figure 4.12a). Both the phantom and table were distinct and each of the stairs could be distinguished well from the others. Though the energy loss projection visually appeared to be less noisy than the multiple scattering projection – which would be an expected outcome for those modalities [47, 71] – this was likely a consequence of the simplistic imaging method and its limitation in terms of range resolution.

One shortcoming of the low beam energy used for imaging was that the energy loss in the middle of the rotating table was large enough, such that no residual range measurement was available in some pixels. Additionally, the region of interest for the three dimensional tomogram needed to be clipped to just below the flat top of

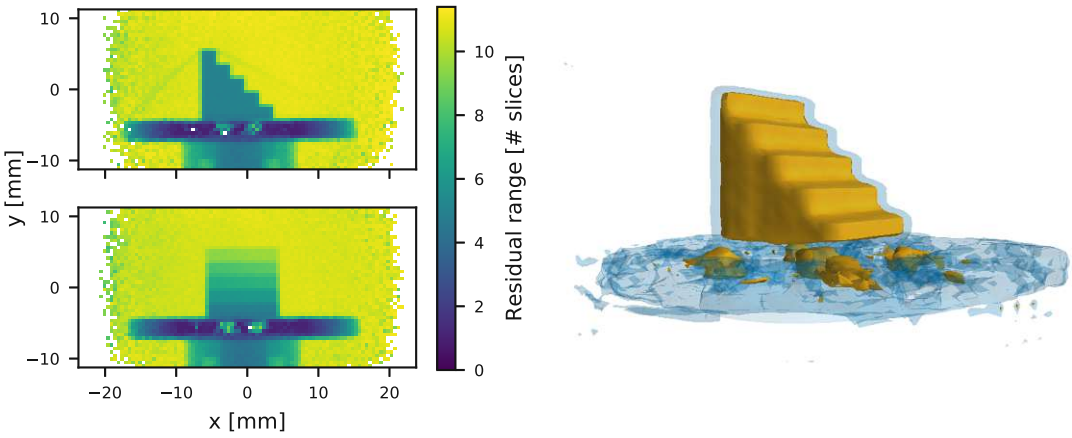

(a) (b)

Figure 4.12: (a) Residual range projection images of the stair phantom, using beamtest data. (b) Three-dimensional contour surfaces of the phantom, excluding (orange) and including (blue) the rotating table.

the rotating table, to remove artifacts resulting from the limited beam spot size (figure 4.12b).

Three-dimensional contour surfaces of two different levels were used to visually separate phantom (orange) and table (blue) in the same way as was previously described for the multiple scatter images (section 4.2.1). Contours of $-0.24\,\text{slices/mm}$ and $-0.01\,\text{slices/mm}$ were used for the phantom and table, respectively. Due to the artifacts at the borders of the beam and missing data points in the flat top of the table it was difficult to clearly separate phantom and table. Additionally, the table itself was reconstructed poorly, with many variations at its surface.

4.3 Achievable Image Resolution of a Single Particle Tracking System

In total, 847 Monte-Carlo simulations were carried out to study the achievable image resolution of a single particle tracking system under various parameter sets. The influence of data cuts was qualitatively evaluated for different position resolutions, and contour levels for constant image resolutions were prepared using detector distance versus clearance, beam energy versus phantom thickness and detector position resolution versus material budget. Although these results were not previously published, they were made available in a preprint [106].

Additional simulations not present in the preprint were carried out to study the differences in set-ups with two and three detectors per tracking stage, using SLT and GBL as track models.

4.3.1 The Influence of Data Cuts

The effect of data cuts on the realisable image resolution was studied for two simulations, one of which used only electromagnetic physics and one that additionally considered hadronic interactions. As described in section 3.5.1, these simulations considered the reference physics lists *G4EmStandardPhysics_option3* (labelled *Only EM*) and *QGSP_BIC* (labelled *Full Physics*). Default parameters were used for the simulations and position resolution was varied between 1 µm to 250 µm (figure 4.13). All analyses were carried out twice, once without applying any cuts and once with 3σ cuts on the distributions of scattering and energy loss between the innermost detectors.

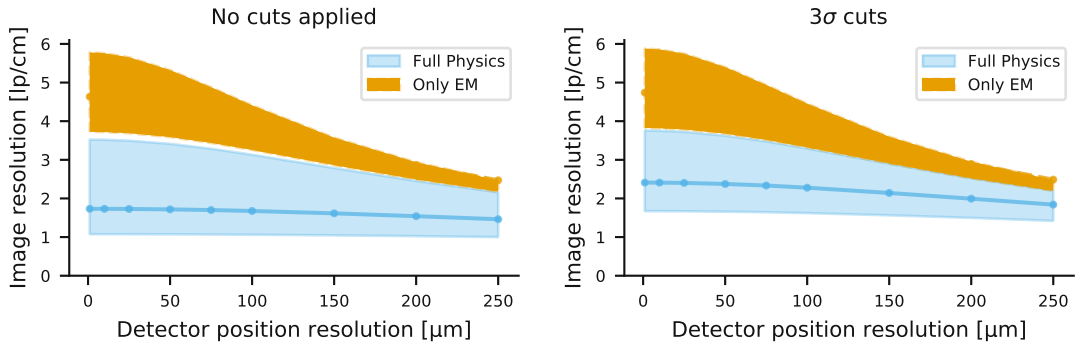

(a) (b)

Figure 4.13: Image resolution (a) without data cuts, and (b) with 3σ data cuts, for full physics and only electromagnetic (Only EM) physics simulations. The shaded area illustrates the range of image resolutions along the z-direction in the phantom. Its minimum is at the peak of the uncertainty envelope and the maximum at the entrance surface. Lines correspond to the mean image resolution within the phantom.

As expected, data cuts improved the image resolution in a full physics simulation while no significant difference was observed with only electromagnetic interactions, indicating that the cuts were likely effective in removing large angle scattering events due to nuclear interactions. Since the distribution of scattering angles in the electromagnetic simulations was based only on the central Gaussian approximation of multiple scattering, no tails were present that could have been removed by such data cuts [41, 112]. Entrance resolution (at the front of the phantom) improved slightly, whereas the minimum resolution increased from 1.06 lp/cm to 1.62 lp/cm

and the mean resolution from 1.68 lp/cm to 2.28 lp/cm, at a position resolution of 100 µm. It is also evident in these results, that the position resolution of the detectors merely had a minor effect on the image resolution. Image resolutions of 2.41 lp/cm, 2.28 lp/cm and 1.84 lp/cm were observed at position resolutions of 1 µm, 100 µm and 250 µm. A more pronounced change in image resolution as function of position resolution was observed for only electromagnetic simulations, possibly indicating that some detrimental effects of nuclear interactions remained even after the cuts.

4.3.2 Distance and Clearance

The distance between detector planes within a tracking stage weakly interacted with other parameters. It was initially used as a parameter, but changed to a constant after reviewing results. A single set of simulations was selected to demonstrate the effects of detector distance. Combinations of distances between 25 mm to 300 mm were used together with clearances between 100 mm to 300 mm, at two position resolutions 50 µm and 200 µm. Default values were used for the other parameters, and both protons and helium ions were considered.

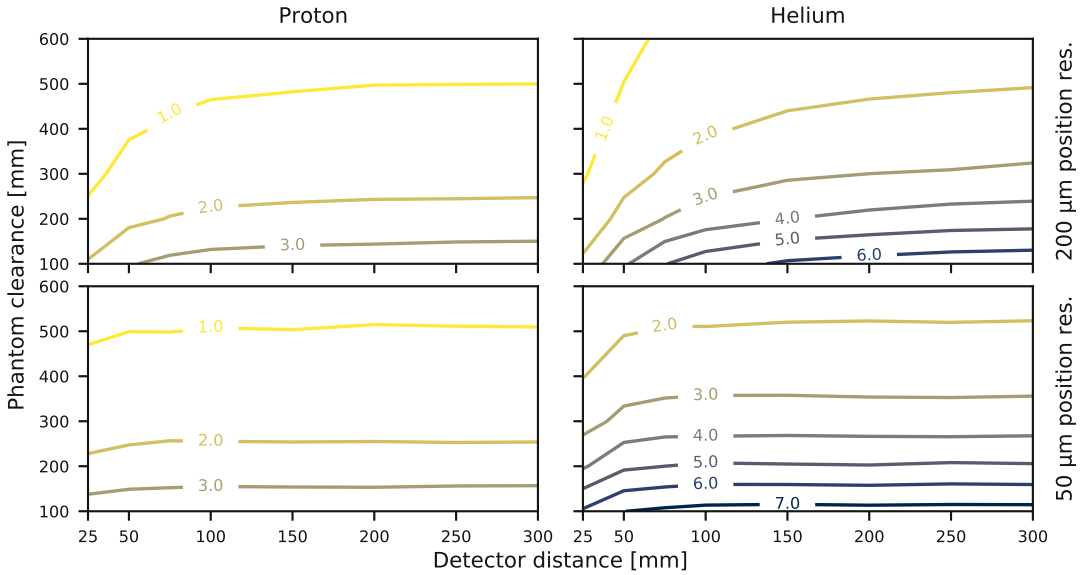

Figure 4.14: Image resolution (1 lp/cm to 7 lp/cm) contours as function of detector distance and phantom clearance, for protons (left) and helium ions (right) and two position resolutions of 50 µm (bottom) and 200 µm (top).

Contour levels of constant image resolutions between 1 lp/cm to 7 lp/cm were used to illustrate the effectiveness of clearance over distance (figure 4.14). Since the con-

tours were mostly parallel to the distance parameter, this meant that an increasing distance was ineffective to increase image resolution. At smaller distances, the contours were less parallel and increased in density with decreasing distance, which was more clearly visible for helium ions and the 200 µm position resolution. Thus, distance initially had an influence on image resolution that disappeared once a large enough distance was reached. For a 50 µm position resolution the contours were already parallel to distance at a value of 100 mm, whereas a small influence was still present at a 200 µm position resolution. Given that larger distances were found to be beneficial for image resolution, a fixed value of 100 mm was used as a compromise between tracking stage compactness and image resolution for the rest of the simulations.

4.3.3 Initial Beam Energy and Target Thickness

Energy and target thickness were studied together at two different clearances of 100 mm and 300 mm and for protons and helium ions as particles. Thicknesses between 100 mm to 300 mm were considered for the phantom and to ensure that primary particles could fully traverse the 300 mm, an energy range of 250 MeV to 500 MeV was used. Similar to distance and clearance, the results were presented as contour lines of constant lateral image resolution (figure 4.15).

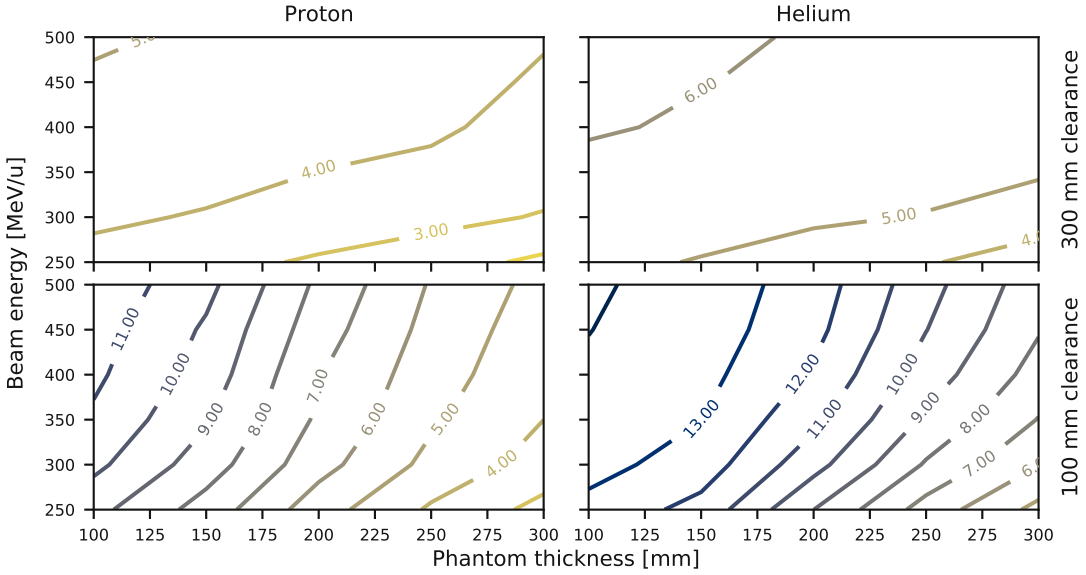

Figure 4.15: Image resolution (2 lp/cm to 13 lp/cm) contours as function of phantom thickness and initial beam energy, for protons (left) and helium ions (right) and two clearances of 100 mm (bottom) and 300 mm (top).

Larger energies resulted in higher image resolutions, likely because of the reduced amount of multiple scattering. This was similar for all four combinations of clearance and particle, with comparable contour densities for both particles at the same clearance. Thickness had a stronger influence on image resolution at a clearance of 100 mm since the slope of the contours was steeper than at 300 mm; also the contours were more dense in the thickness direction. Similarly, the density was reduced for the energy parameter and additional energy was less effective in increasing image resolution, at a large clearance. This was especially apparent at energies above 350 MeV/u, at which additional energy only slowly increased image resolution. The remaining parameters were studied for energies below 400 MeV/u since high energy was less effective in increasing image resolution at a clearance of 100 mm as well, and because elevated energies could impede the density resolution in an ion imaging scan and reduce image contrast [29].

4.3.4 Detector Position Resolution and Material Budget

The two parameters for modelling a detector – position resolution and material budget – were examined given three different beam energies of 250 MeV, 300 MeV and 350 MeV; two phantom thicknesses of 200 mm and 300 mm; two clearances of 100 mm and 300 mm; and using both protons and helium ions. Contours in the position resolution and material budget plane were plotted for all three energies and grouped by the other parameters (figure 4.16).

An imagined normal vector on a point of such a contour line would be directed towards the gradient of image resolution – i.e. at the strongest ascent or descent – since the contours themselves represent a constant level of lateral image resolution. Therefore, the slope of these lines was tied to the influence of both position resolution and material budget. At a $-45°$ slope, both parameters had the same influence on image resolution because the normal vector was directed towards both axes equally; with steeper or less steep angles corresponding to a stronger influence of position resolution or material budget, respectively. Roughly comparable influences were observed often when both parameter values were far from zero. In these cases an improvement in either parameter would also improve image resolution. One could however observe that the slope gradually became flatter or steeper towards lower parameter values, especially for position resolution, where diminishing returns were found below a resolution of 50 µm. Under 25 µm the contours were mostly parallel to the position resolution axis, which meant that with better position resolution additional improvements were less effective. Although the contours were generally steeper at higher energies and for helium ions instead

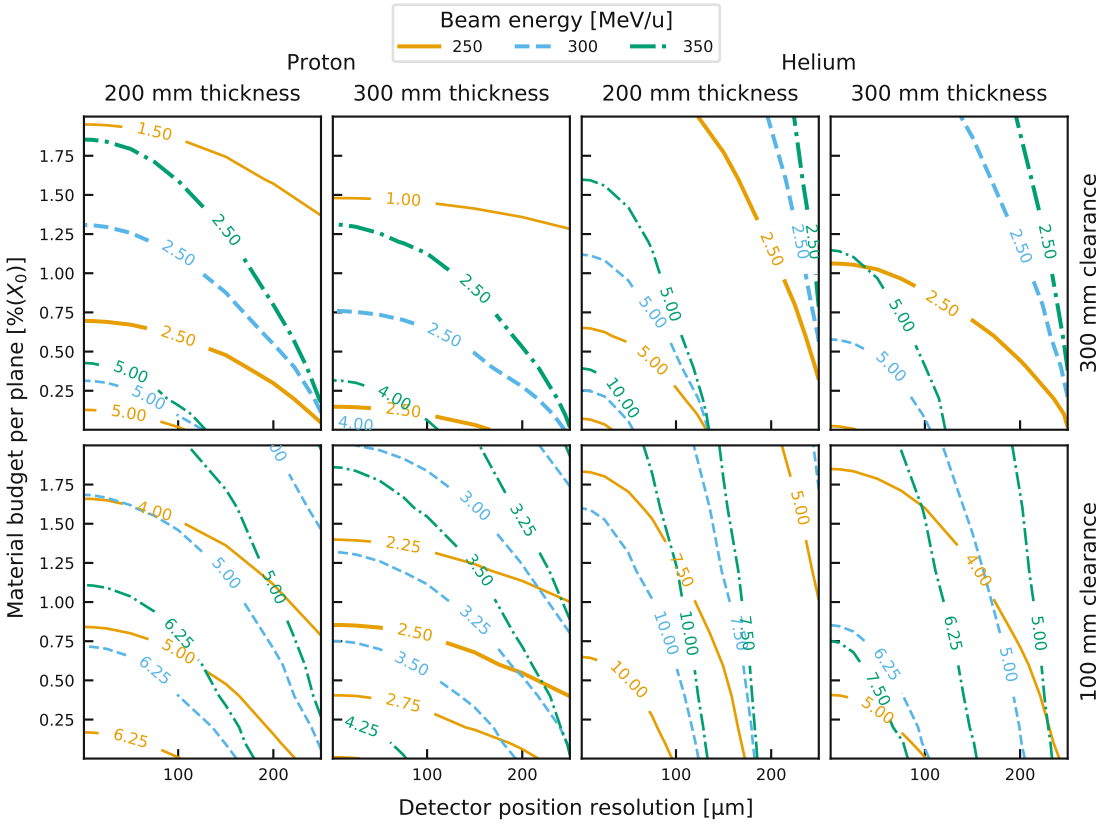

Figure 4.16: Image resolution (1 lp/cm to 10 lp/cm) contours as function of position resolution and material budget at different energies, thicknesses, clearances and for protons and helium ions. Rows correspond to different clearance values of 100 mm (bottom) and 300 mm (top). Columns represent both different particle species – the first two columns corresponding to protons, and the last two to helium ions – and phantom thicknesses, which alternate between 200 mm and 300 mm.

of protons, they were still mostly parallel below 25 µm in these cases too. Diminishing returns were also observed for the material budget parameter when helium ions were used, but a thickness reduction of a thin sensor was still effective for a better image resolution in proton imaging.

Figure 4.16 also illustrates how other parameters could change the influence of a detector's position resolution and material budget. For example, additional energy not only reduced the contour density but also moved the same image resolution levels towards larger values of both detector parameters. Thus, additional energy could be used to compensate for a sub-optimal (thick) detector. In the considered parameter space this effect was more relevant for material budget than position resolution, especially for helium ions. A similar but inversed effect was observed for

additional clearance, where a bigger air gap between detectors and phantom moved the same contours towards smaller parameter values and increased the density. The worst results in terms of image resolution were observed for a proton beam irradiating a 300 mm phantom at a large clearance of 300 mm. In this scenario a resolution of 4 lp/cm was found for thin and accurate detectors.

A lower limit of 2.5 lp/cm in image resolution was selected as suitable for ion imaging, since it corresponds to the Nyquist frequency of an image with a reasonably large pixel size of 2 mm. To meet the 2.5 lp/cm requirement, a hypothetical sensor would need to be left of the corresponding contour in terms of position resolution and below the contour in material budget. This was mostly fulfilled at a clearance of 100 mm (lower row in figure 4.16), except for a proton beam irradiating a 300 mm phantom (second column). In this scenario, the target contour for a 250 MeV beam was located at 0.75 % to 0.5 %, depending on position resolution. Given an energy of 300 MeV, the target contour was already outside of the parameter ranges used. Slightly more strict requirements were observed for the larger clearance of 300 mm (top row in figure 4.16) where the 2.5 lp/cm appeared for all four combinations of particles and phantom thicknesses considered. Again, the worst results were observed when using a proton beam and a 300 mm thick phantom (second column). In this case, the target contour was below a position resolution of 150 µm and below a material budget of 0.15 %.

4.3.5 Four vs. Six Tracking Planes

Set-ups with four and six detector planes were compared in terms of their MLP uncertainty, to determine whether the redundancy of a six plane set-up could be used to reduce imaging dose without reducing the achievable image resolution (section 3.5.1).

Tracking Accuracy

The accuracy of track fits in each tracking stage was evaluated to confirm the validity of the results. Tracks were fitted to measured positions with random displacements applied to them, using SLT as the track model for the four plane set-up and both of SLT and GBL for the six plane set-up. Positions and directions of the resulting tracks were compared to the actual positions and directions at each detector plane – which were stored during the simulations – to evaluate the RMSDs of track fit positions and directions (figure 4.17).

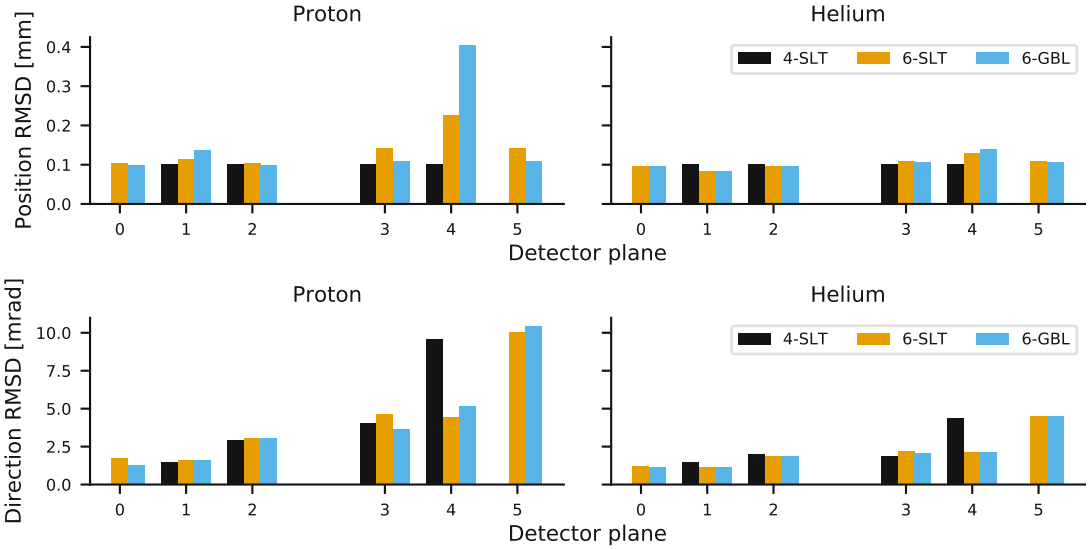

Figure 4.17: Position (top) and direction (bottom) root-mean-square deviation (RMSD) of track fits based on position measurements with random displacements applied prior to tracking, and actual interaction positions and directions. Six plane set-ups with straight line track (SLT) and with general broken lines (GBL) as track models were compared to standard ion imaging systems.

As expected, the position RMSD of four plane set-ups was equivalent to the random displacements applied to the measurements, prior to tracking. Six plane set-ups with SLT as track model had higher position RMSDs on the downstream tracking stage, likely caused by scattering in the detector planes. Using GBL instead of SLT, these RMSDs were corrected for the first and last detector, but significantly increased for the middle detector in the stage. While similar observations were made for protons and helium ions, the magnitude of these effects was much lower for helium ions. Position RMSD at the first downstream detector was slightly larger for six plane set-ups regardless of the track model, using helium ions.

Direction RMSD increased towards the downstream end of the system for all tracking configurations. Here, the observations were different for the two particle species. For protons, the first downstream direction RMSD was slightly worse when using SLT and slightly better with GBL. Using helium ions, both of the track models produced a worse RMSD for six plane set-ups. Since measurements at the innermost detectors were used to reconstruct the MLP within the phantom, position and direction RMSDs at those planes should be comparable to the standard four plane set-up. This results indicate that the GBL model could be used to improve the performance of six plane set-ups for protons, but not for helium ions, given default system parameters.

Influence of System Parameters

136 simulations were carried out while iterating through different system parameter values to study the performance of six plane set-ups compared to four plane set-ups. One set of simulations was used for each of the parameters: beam energy, detector distance, phantom clearance, material budget and position resolution. Each set considered protons and helium ions for four plane set-ups using SLT and six plane set-ups using both SLT and GBL (figure 4.18).

A single simulation with default parameter values was used to qualitatively compare the uncertainty envelopes, converted to lateral image resolution, according to equation (3.6). Using default parameters, the image resolution of six plane set-ups were observed to be lower than those of four plane set-ups (figure 4.18a), regardless of the track model. For protons, the second half of the depth-dependent image resolution curve was improved slightly when GBL was used instead of SLT; the lowest resolution was increased from 1.66 lp/cm to 1.9 lp/cm. A much smaller improvement was observed for helium ions, where GBL increased the lowest resolution from 3.12 lp/cm to 3.2 lp/cm.

The other graphs of figure 4.18 display summaries of the lowest resolution within the phantom as a function of different parameter values for the parameters beam energy, phantom clearance, detector material budget, detector distance and position resolution. For the initial beam energy, four plane set-ups performed better at low, but worse at high energies (figure 4.18b). Six planes with SLT outperformed four planes at energies beyond ≈312.5 MeV for protons and ≈237.5 MeV/u for helium ions. For protons, the GBL model already outperformed a four plane set-up at a lower energy of ≈250 MeV, whereas only a minor difference between GBL and SLT was observed for helium ions.

The parameters clearance (figure 4.18c) and material budget (figure 4.18d) were similar in that the minimum resolution was consistently worse for six plane set-ups than for four plane set-ups. Using GBL instead of SLT allowed to improve resolutions to slightly below the levels of a four plane set-up for protons only, while the achieved resolutions stayed closer to those of SLT when helium ions were used. One property that stood out for the clearance parameter was that the difference in resolution between four and six planes increased at 125 mm to 200 mm and decreased for higher values. For helium ions in particular a difference of 0.98 lp/cm was observed at 200 mm. A much smaller difference of 0.12 lp/cm was observed for GBL at 100 mm.

For the distance between detectors, a four plane set-up performed worse at lower distances below a distance of 100 mm (figure 4.18e). Almost no change in minimum

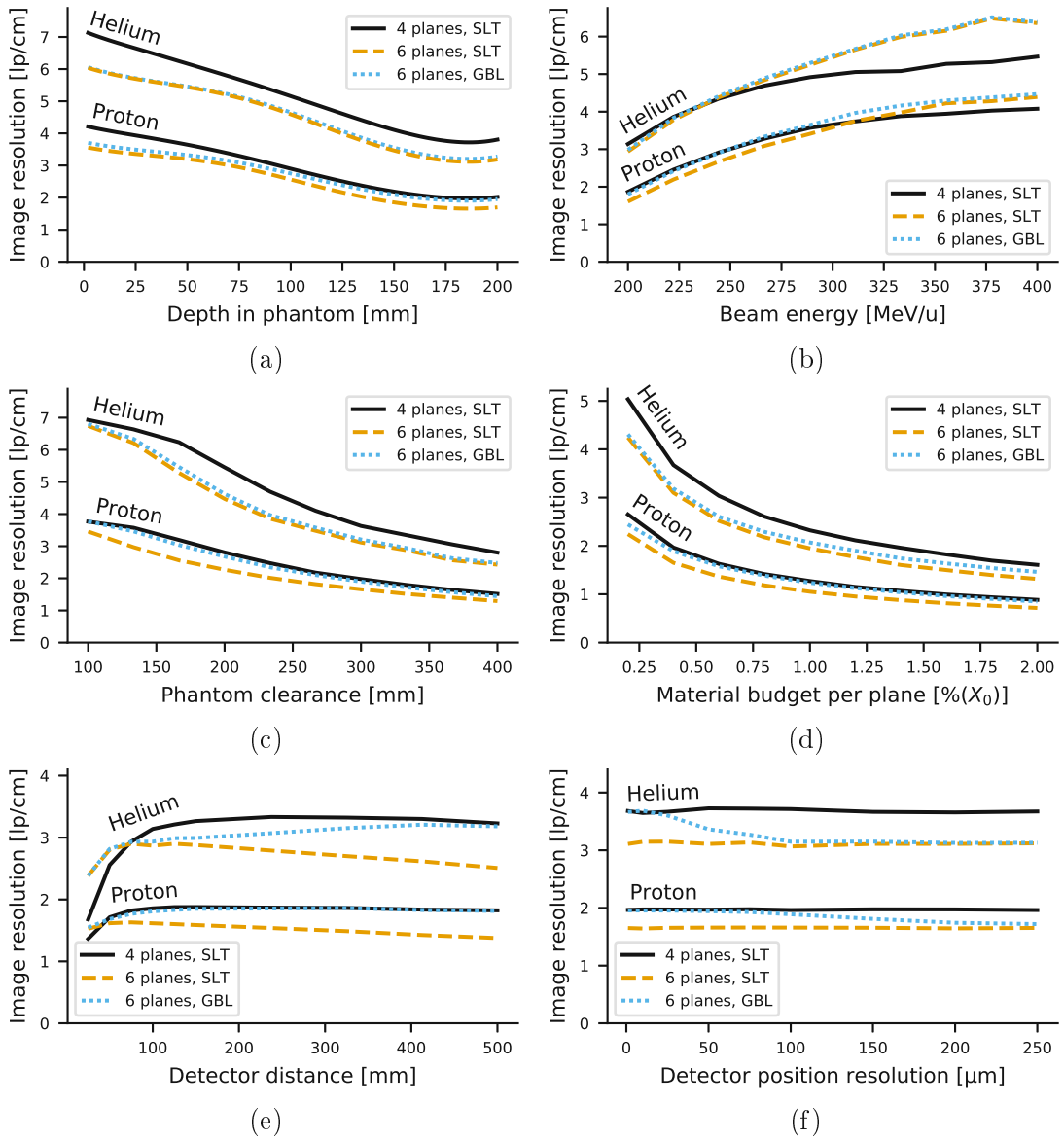

Figure 4.18: Comparison of (lateral) image resolutions in four- and six-detector set-ups. Depth-dependent image resolution (a), and minimum image resolutions in the phantom for different parameter values of energy (b), detector distance (e), phantom clearance (c), detector material budget (d) and position resolution (f). For four-detector set-ups, only the straight line track (SLT) model was used for track fitting, and both of SLT and general broken lines (GBL) were used with six planes.

resolution was observed for protons at increasing distances, whereas a maximum of 3.33 lp/cm was found at ≈240 mm for helium ions. Six plane set-ups using SLT performed worse at distances greater than 100 mm, with an increasing difference between set-ups with four and six planes. When GBL was used, the difference was mostly eliminated for protons and improved for helium ions, with a decreasing difference for larger distances.

The final parameter being considered was position resolution, which had a strong influence on the resolution improvement when GBL was used (figure 4.18f). Both of the four plane and six plane set-ups had a constant image resolution as function of the position resolution – all other parameters having default values – when SLT was used for tracking. Below a certain position resolution, the image resolution of a six plane set-up with GBL more closely matched the image resolution of a four plane set-up, whereas it converged towards the resolution of a six plane set-up with SLT for increasing position resolutions. Only a small difference between four planes and six planes with GBL was observed below a position resolution of 75 µm for protons or 25 µm for helium ions. Above 250 µm for protons and 100 µm for helium ions, the improvements realised by GBL diminished.

4.3.6 Image Resolution in a Small Aluminium Phantom

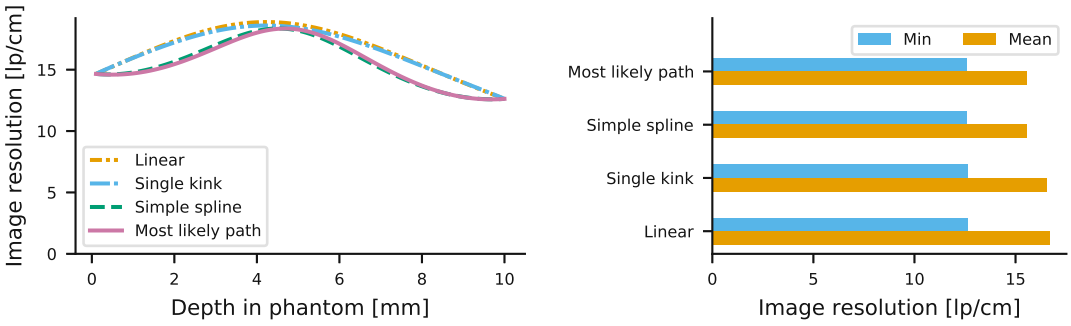

(a) (b)

Figure 4.19: (a) Lateral image resolution of a small Aluminium phantom as function of depth. (b) Minimum and mean resolution of each model.

Lateral image resolution within a 10 mm small phantom was comparable for all considered path models (figure 4.19). Surprisingly, the lowest resolutions occurred at the borders of the phantom and were similar for all models. This could originate from the small size of the phantom and the low uncertainty due to multiple scattering within it, when compared to the uncertainty due to outside effects. The

minima at the borders were mostly a result of outside uncertainties, such as scattering in air and the detectors, and nonzero position resolutions of the detectors. Overall, only a slight difference of $\approx$1 lp/cm was observed between the GBL and single kink models for the mean resolution. These small details would have been lost in the image reconstructions with measurement data, due to the use of coarse pixel grids of 500 µm $\times$ 500 µm and the limited amount of particles per pixel; a consequence of the event rate during data acquisitions. Additionally, only the thickest part of the stair phantoms was 10 mm deep, whereas other stairs were thinner (down to 2 mm).

5 Discussion

5.1 Measurements

An ion imaging demonstrator was set up at the MedAustron facility. The system consisted of up to six DSSDs, a range telescope and a shared triggering system to synchronise readouts. It could perform single particle tracking and measure the corresponding residual range of beam particles at a mean rate of 2 kHz. The demonstrator was used in beamtests to record imaging data sets of an aluminium phantom, suitable for image reconstruction based on multiple scattering and energy loss. Though the data also could support a reconstruction workflow based on attenuation, this was a coincidence: a dedicated scanner for ion imaging would need to move the triggers to the front of the telescope so that a larger amount of nuclear scatter events could be recorded. The three-dimensional reconstructions with this demonstrator could reproduce the original phantoms. However, it was evident that a new version of the scanner would be needed for ion imaging due to technical shortcomings, such as tracker size and resolution, residual range resolution and DAQ rate.

Although the sensors used for tracking were too small for a head-sized phantom, these could easily be replaced by larger sensors with the same technology. As an example, tracker modules made of four silicon strip tiles with small gaps between them were described in Johnson et al. [113], which reported a module detection efficiency of more than 99 % over a large area. These replacements could be produced with a slightly larger (worse) strip pitch without suffering major drawbacks, since it was demonstrated that better position resolutions than 50 µm faced diminishing returns in the achievable image resolution. Given that the tracking residuals were observed in the range of 5 µm to 31 µm (with uncertainty due to scattering included), a worse strip pitch above 100 µm would likely be justified.

Additionally, the APV25 chips used for the tracker readout recorded several samples per interacting particle, which reduced the maximum DAQ rate in favour of an accurate hit time and shape measurement. A faster rate could be accomplished with different readout electronics that consider a simple threshold to decide whether a strip was hit or not directly on the chip, significantly reducing the

amount of data to transfer. Although this requires a complete replacement of the readout hardware, such an update would be beneficial in an ion imaging context, since a reduction in the acquisition time of a scan is much more valuable than an accurate hit time reconstruction.

Another shortcoming was the residual energy resolution, which should have been better than 0.1 % in terms of $\Delta E/E$ for an accurate stopping power reconstruction in a clinical application such as a head scan [53]. This requirement was not met with the rather simplistic method of using the last scintillator layer with a signal above a threshold value as the residual range. Operating the detector like a sampling calorimeter also was not possible due to the low dynamic range of its SiPMs, which allowed to either measure in the Bragg peak region or the plateau, but not both.

5.2 Simulations

The achievable image resolution of single particle tracking systems was studied, to work out technical requirements for an upcoming replacement of the detector. Many simulations, using tracking planes placed around a subdivided water target, were performed to investigate the influence of system parameters on the MLP uncertainty within the target. An overview of achievable image resolutions within the parameter space was created to identify intervals of material budget and position resolution that could reach a worst image resolution of 2.5 lp/cm (corresponding to a pixel size of 2 mm).

In the worst-case scenario considered – which used a phantom size of 300 mm, a large clearance of 300 mm and a proton beam with 250 MeV initial energy – the 2.5 lp/cm resolution was achievable for material budgets below 0.15 % and a position resolution below 150 µm. Less strict requirements were observed in all other scenarios, such as at an increased beam energy or reduced clearance. Additionally, the contour density in the worst-case scenario was low, and only a slightly worse image resolution was observed for higher material budgets. For these reasons, a new detector with a material budget below 0.75 % would likely be suitable for ion imaging, especially if the beam energy can be increased accordingly for larger target thicknesses. The influence of position resolution was observed to be less relevant than material budget and diminishing returns were observed mostly below 50 µm. Though a better position resolution could improve the image resolution slightly, it would also increase the number of readout channels of the system. Detectors with a position resolution up to 100 µm were accurate enough to achieve the target image resolution of 2.5 lp/cm in the conducted simulations.

Since a better image resolution allows to distinguish smaller details in a scan it is beneficial to not just build a thin and accurate tracking system, but also operate it in optimal way. Simulation results have demonstrated that the distance between detectors of the two tracking stages has a small influence after exceeding a minimum of 50 mm to 100 mm. This was in line with previous research that came to similar conclusions. Clearance was one of the most significant parameters and should be kept as low as reasonably achievable to obtain the best image resolution. For a head-sized phantom (200 mm) the best results observed were just above 10 lp/cm, using helium ions. In contrast, the best result for a proton beam was 6.25 lp/cm for very thin detectors. Therefore, details in the order of magnitude of 0.5 mm to 0.8 mm should be resolvable with a suitable ion imaging scanner.

Another aim of the simulations in this work was to compare detector layouts using two and three tracking planes per stage in terms of their path uncertainty. It could be demonstrated that an additional plane significantly reduces the accuracy of the MLP model when SLT was used for tracking. When GBL was used instead of SLT, the detrimental effects of the additional planes were mostly removed for protons and a detector position resolution below 100 µm. For helium ions however, a much larger part of the parameter space remained worse with six planes even when GBL was used; though the additional uncertainty disappeared mostly below a position resolution of 25 µm or for detector distances in excess of 400 mm. These results suggest that an additional plane could potentially be used in a proton imaging context, with only a small reduction in terms of image resolution. Given non-zero inefficiencies of the detectors this could improve the overall detection efficiency of a system, and therefore reduce the necessary dose of a scan.

6 Conclusion

A demonstrator for an ion imaging system based on single particle tracking was set up at the MedAustron facility for ion therapy and research. It was used to gather position and energy loss measurements of beam particles that passed through small metallic phantoms, which were then used to reconstruct three dimensional tomographic images of the phantoms. The demonstrator will be replaced by a new system, capable for preclinical studies at the facility.

Monte Carlo simulations were used to study the technical requirements for tracking detectors, such as position resolution and material budget. An overview of the influence of each parameter on the achievable image resolution was produced with a simple representation of a single particle tracking system and a large amount of simulations with varying system parameters. For each simulated particle, the reconstructed MLP was compared to its actual path through the phantom to evaluate the uncertainty envelope of the MLP model. These envelopes were then converted to an image resolution per set of system parameters. Intervals in the parameter space that are suitable for ion imaging were obtained with this method, using contours of constant image resolution.

Based on these simulations, it was also demonstrated that systems with six tracking planes could potentially increase tracking efficiency with only a minor loss of image resolution. With a SLT model in the tracking planes, the scattering in the additional planes consistently reduced the image resolution. Depending on the system parameters, these resolution losses were mitigated for protons when the GBL model was used instead of SLT.

As a closing remark, it should be noted that the MLP uncertainty envelope analysis in this work can estimate the intrinsic image resolution of a hypothetical scanner. The method does, however, fail to consider additional uncertainty due to the image reconstruction algorithms employed in an ion imaging scan [55, 56]. It would therefore be sensible to perform a follow-up study with simulations of realistic scanners to acquire imaging data sets of a phantom, and to measure the image resolution of, for example line pair inserts or edges, in a tomogram [62, 74, 114]. Results of such an investigation could be used to challenge the conclusions about six detectors and the GBL model in subsequent studies.

Acronyms

COG	center of gravity
CSDA	continuous slowing down approximation
CT	computed tomography
DAQ	data acquisition
DSSD	double sided silicon strip detector
ESF	edge spread function
FADC	flash analog digital converter
GBL	general broken lines
LSF	line spread function
MLP	most likely path
MTF	modulation transfer function
PMT	photomultiplier
RMSD	root-mean-square deviation
RSP	relative stopping power
SART	simultaneous algebraic reconstruction technique
SiPM	silicon photomultiplier
SLT	straight line track
TLU	trigger logic unit

Bibliography

[1] A. M. Cormack. "Representation of a Function by Its Line Integrals, with Some Radiological Applications". In: *Journal of Applied Physics* 34.9 (Sept. 1963), pp. 2722–2727. DOI: 10.1063/1.1729798.

[2] A. M. Koehler. "Proton Radiography". In: *Science* 160.3825 (Apr. 1968), pp. 303–304. DOI: 10.1126/science.160.3825.303.

[3] V. W. Steward and A. M. Koehler. "Proton Beam Radiography in Tumor Detection". In: *Science* 179.4076 (Mar. 1973), pp. 913–914. DOI: 10.1126/science.179.4076.913.

[4] J. A. Cookson. "Radiography with Protons". In: *Die Naturwissenschaften* 61.5 (May 1974), pp. 184–191. DOI: 10.1007/bf00599915.

[5] D. R. Moffett et al. "Initial Test of a Proton Radiographic System". In: *IEEE Transactions on Nuclear Science* 22.3 (1975), pp. 1749–1751. DOI: 10.1109/tns.1975.4327982.

[6] M. Goitein. "Three-dimensional density reconstruction from a series of two-dimensional projections". In: *Nuclear Instruments and Methods* 101.3 (June 1972), pp. 509–518. DOI: 10.1016/0029-554x(72)90039-0.

[7] A. M. Cormack and A. M. Koehler. "Quantitative proton tomography: preliminary experiments". In: *Physics in Medicine and Biology* 21.4 (July 1976), pp. 560–569. DOI: 10.1088/0031-9155/21/4/007.

[8] K. M. Hanson. "Proton Computed Tomography". In: *IEEE Transactions on Nuclear Science* 26.1 (Feb. 1979), pp. 1635–1640. DOI: 10.1109/tns.1979.4330455.

[9] Y. Takada et al. "Proton computed tomography with a 250 MeV pulsed beam". In: *Nuclear Instruments and Methods in Physics Research Section A: Accelerators, Spectrometers, Detectors and Associated Equipment* 273.1 (Dec. 1988), pp. 410–422. DOI: 10.1016/0168-9002(88)90844-3.

[10] K. M. Crowe et al. "Axial Scanning with 900 MeV Alpha Particles". In: *IEEE Transactions on Nuclear Science* 22.3 (1975), pp. 1752–1754. DOI: 10.1109/tns.1975.4327983.

[11] E. V. Benton et al. *Radiography with heavy particles.* Tech. rep. LBL–2887. United States, 1975, p. 68. URL: http://inis.iaea.org/search/search.aspx?orig_q=RN:07229261.

[12] M. P. Capp et al. "Heavy Ion Radiography". In: *Recent and Future Developments in Medical Imaging I.* Ed. by Norman A. Baily. SPIE, Nov. 1978. DOI: 10.1117/12.938197.

[13] S. N. Penfold et al. "Geometrical optimization of a particle tracking system for proton computed tomography". In: *Radiation Measurements* 46.12 (2011). Proceedings of the 16th Solid State Dosimetry Conference, September 19-24, Sydney, Australia, pp. 2069–2072. ISSN: 1350-4487. DOI: 10.1016/j.radmeas.2011.04.032.

[14] H. F.-W. Sadrozinski et al. "Development of a head scanner for proton CT". In: *Nuclear Instruments and Methods in Physics Research Section A: Accelerators, Spectrometers, Detectors and Associated Equipment* 699 (2013). Proceedings of the 8th International "Hiroshima" Symposium on the Development and Application of Semiconductor Tracking Detectors, pp. 205–210. ISSN: 0168-9002. DOI: 10.1016/j.nima.2012.04.029.

[15] M. Scaringella et al. "A proton Computed Tomography based medical imaging system". In: *Journal of Instrumentation* 9.12 (2014), pp. C12009–C12009. DOI: 10.1088/1748-0221/9/12/c12009.

[16] S. A. Uzunyan et al. "A New Proton CT Scanner". In: *ArXiv e-prints* (2016). arXiv: 1409.0049.

[17] S. Mattiazzo et al. "iMPACT: An Innovative Tracker and Calorimeter for Proton Computed Tomography". In: *IEEE Transactions on Radiation and Plasma Medical Sciences* 2.4 (2018), pp. 345–352. DOI: 10.1109/TRPMS.2018.2825499.

[18] M. Esposito et al. "PRaVDA: The first solid-state system for proton computed tomography". In: *Physica Medica: European Journal of Medical Physics* 55 (Nov. 2018), pp. 149–154. ISSN: 1120-1797. DOI: 10.1016/j.ejmp.2018.10.020.

[19] H. E. S. Pettersen et al. "Design optimization of a pixel-based range telescope for proton computed tomography". In: *Physica Medica: European Journal of Medical Physics* 63 (July 2019), pp. 87–97. ISSN: 1120-1797. DOI: 10.1016/j.ejmp.2019.05.026.

[20] K. M. Hanson et al. "Computed tomography using proton energy loss". In: *Physics in Medicine and Biology* 26.6 (Nov. 1981), pp. 965–983. DOI: 10.1088/0031-9155/26/6/001.

[21] G. Molière. "Theorie der Streuung schneller geladener Teilchen I. Einzelstreuung am abgeschirmten Coulomb-Feld". In: *Zeitschrift für Naturforschung A* 2.3 (Mar. 1947), pp. 133–145. DOI: 10.1515/zna-1947-0302.

[22] G. Molière. "Theorie der Streuung schneller geladener Teilchen II Mehrfach-und Vielfachstreuung". In: *Zeitschrift für Naturforschung A* 3 (1948), pp. 78–97.

[23] U. Schneider et al. "The calibration of CT Hounsfield units for radiotherapy treatment planning". In: *Physics in Medicine and Biology* 41.1 (Jan. 1996), pp. 111–124. DOI: 10.1088/0031-9155/41/1/009.

[24] U. Schneider and E. Pedroni. "Proton radiography as a tool for quality control in proton therapy". In: *Medical Physics* 22.4 (Apr. 1995), pp. 353–363. DOI: 10.1118/1.597470.

[25] N. Matsufuji et al. "Relationship between CT number and electron density, scatter angle and nuclear reaction for hadron-therapy treatment planning". In: *Physics in Medicine and Biology* 43.11 (Nov. 1998), pp. 3261–3275. DOI: 10.1088/0031-9155/43/11/007.

[26] B. Schaffner and E. Pedroni. "The precision of proton range calculations in proton radiotherapy treatment planning: experimental verification of the relation between CT-HU and proton stopping power". In: *Physics in Medicine and Biology* 43.6 (June 1998), pp. 1579–1592. DOI: 10.1088/0031-9155/43/6/016.

[27] A. V. Chvetsov and S. L. Paige. "The influence of CT image noise on proton range calculation in radiotherapy planning". In: *Physics in Medicine and Biology* 55.6 (Feb. 2010), N141–N149. DOI: 10.1088/0031-9155/55/6/n01.

[28] M. Yang et al. "Comprehensive analysis of proton range uncertainties related to patient stopping-power-ratio estimation using the stoichiometric calibration". In: *Physics in Medicine and Biology* 57.13 (June 2012), pp. 4095–4115. DOI: 10.1088/0031-9155/57/13/4095.

[29] R. W. Schulte et al. "Density resolution of proton computed tomography". In: *Medical Physics* 32.4 (Mar. 2005), pp. 1035–1046. DOI: 10.1118/1.1884906.

[30] M. Benedikt and A. Wrulich. "MedAustron—Project overview and status". In: *The European Physical Journal Plus* 126.7 (July 2011). DOI: 10.1140/epjp/i2011-11069-9.

[31] D. Schardt et al. "Heavy-ion tumor therapy: Physical and radiobiological benefits". In: *Rev. Mod. Phys.* 82 (1 Feb. 2010), pp. 383–425. DOI: 10.1103/RevModPhys.82.383.

[32] W. D. Newhauser and R. Zhang. "The physics of proton therapy". In: *Physics in Medicine and Biology* 60.8 (Mar. 2015), R155–R209. DOI: 10.1088/0031-9155/60/8/r155.

[33] M. Tanabashi et al. "Review of Particle Physics". In: *Phys. Rev. D* 98 (3 Aug. 2018), p. 030001. DOI: 10.1103/PhysRevD.98.030001.

[34] M.J. Berger et al. *ESTAR, PSTAR, and ASTAR: Computer Programs for Calculating Stopping-Power and Range Tables for Electrons, Protons, and Helium Ions*. en. online, accessed: 2020-12-18. 2017. DOI: 10.18434/T4NC7P.

[35] H. Bethe. "Bremsformel für Elektronen relativistischer Geschwindigkeit". In: *Zeitschrift für Physik* 76.5-6 (1932), pp. 293–299. DOI: 10.1007/bf01342532.

[36] J. F. Ziegler. "Stopping of energetic light ions in elemental matter". In: *Journal of Applied Physics* 85.3 (Feb. 1999), pp. 1249–1272. DOI: 10.1063/1.369844.

[37] D. R. Grimes et al. "An approximate analytical solution of the Bethe equation for charged particles in the radiotherapeutic energy range". In: *Scientific Reports* 7.1 (Aug. 2017). DOI: 10.1038/s41598-017-10554-0.

[38] R. R. Wilson. "Radiological Use of Fast Protons". In: *Radiology* 47.5 (Nov. 1946), pp. 487–491. DOI: 10.1148/47.5.487.

[39] U. Fano. "Degradation and Range Straggling of High-Energy Radiations". In: *Physical Review* 92.2 (Oct. 1953), pp. 328–349. DOI: 10.1103/physrev.92.328.

[40] H. W. Lewis. "Range Straggling of a Nonrelativistic Charged Particle". In: *Physical Review* 85.1 (Jan. 1952), pp. 20–24. DOI: 10.1103/physrev.85.20.

[41] G. R. Lynch and O. I. Dahl. "Approximations to multiple Coulomb scattering". In: *Nuclear Instruments and Methods in Physics Research Section B: Beam Interactions with Materials and Atoms* 58.1 (1991), pp. 6–10. ISSN: 0168-583X. DOI: 10.1016/0168-583X(91)95671-Y.

[42] Y.-S. Tsai. "Pair Production and Bremsstrahlung of Charged Leptons". In: *Rev. Mod. Phys.* 46 (1974). [Erratum: Rev.Mod.Phys. 49, 421–423 (1977)], p. 815. DOI: 10.1103/RevModPhys.46.815.

[43] R. W. Schulte et al. "A maximum likelihood proton path formalism for application in proton computed tomography". In: *Medical Physics* 35.11 (2008), pp. 4849–4856. DOI: 10.1118/1.2986139.

[44] B. Gottschalk. "On the scattering power of radiotherapy protons". In: *Medical Physics* 37.1 (Dec. 2009), pp. 352–367. DOI: 10.1118/1.3264177.

[45] A. C. Kraan. "Range Verification Methods in Particle Therapy: Underlying Physics and Monte Carlo Modeling". In: *Frontiers in Oncology* 5 (July 2015). DOI: 10.3389/fonc.2015.00150.

[46] C. Bopp et al. "Proton computed tomography from multiple physics processes". In: *Physics in Medicine and Biology* 58.20 (Sept. 2013), pp. 7261–7276. DOI: 10.1088/0031-9155/58/20/7261.

[47] C. T. Quiñones et al. "Filtered back-projection reconstruction for attenuation proton CT along most likely paths". In: *Physics in Medicine and Biology* 61.9 (Apr. 2016), pp. 3258–3278. DOI: 10.1088/0031-9155/61/9/3258.

[48] G. Lutz. *Semiconductor Radiation Detectors*. Springer Berlin Heidelberg, 2007. DOI: 10.1007/978-3-540-71679-2.

[49] H. Kolanoski and N. Wermes. *Teilchendetektoren*. Springer Berlin Heidelberg, 2016. DOI: 10.1007/978-3-662-45350-6.

[50] J.B. Birks. *The Theory and Practice of Scintillation Counting*. Pergamon, 1964. ISBN: 978-0-08-010472-0.

[51] W. R. Leo. *Techniques for Nuclear and Particle Physics Experiments*. Springer Berlin Heidelberg, 1994. DOI: 10.1007/978-3-642-57920-2.

[52] B. Dolgoshein et al. "Status report on silicon photomultiplier development and its applications". In: *Nuclear Instruments and Methods in Physics Research Section A: Accelerators, Spectrometers, Detectors and Associated Equipment* 563.2 (2006), pp. 368–376. ISSN: 0168-9002. DOI: 10.1016/j.nima.2006.02.193.

[53] R. W. Schulte et al. "Conceptual design of a proton computed tomography system for applications in proton radiation therapy". In: *IEEE Transactions on Nuclear Science* 51.3 (2004), pp. 866–872. DOI: 10.1109/TNS.2004.829392.

[54] J. T. Taylor et al. "An experimental demonstration of a new type of proton computed tomography using a novel silicon tracking detector". In: *Medical Physics* 43.11 (Oct. 2016), pp. 6129–6136. DOI: 10.1118/1.4965809.

[55] N. Krah et al. "A comprehensive theoretical comparison of proton imaging set-ups in terms of spatial resolution". In: *Physics in Medicine & Biology* 63.13 (July 2018), p. 135013. DOI: 10.1088/1361-6560/aaca1f.

[56] J. R. Sølie et al. "Image quality of list-mode proton imaging without front trackers". In: *Physics in Medicine & Biology* 65.13 (July 2020), p. 135012. DOI: 10.1088/1361-6560/ab8ddb.

[57] V. A. Bashkirov et al. "Novel scintillation detector design and performance for proton radiography and computed tomography". In: *Medical Physics* 43.2 (Jan. 2016), pp. 664–674. DOI: 10.1118/1.4939255.

[58] M. Bucciantonio et al. "Development of a fast proton range radiography system for quality assurance in hadrontherapy". In: *Nuclear Instruments and Methods in Physics Research Section A: Accelerators, Spectrometers, Detectors and Associated Equipment* 732 (Dec. 2013), pp. 564–567. DOI: 10.1016/j.nima.2013.05.110.

[59] U. Schneider and E. Pedroni. "Multiple Coulomb scattering and spatial resolution in proton radiography". In: *Medical Physics* 21.11 (1994), pp. 1657–1663. DOI: 10.1118/1.597212.

[60] V. Blobel. "A new fast track-fit algorithm based on broken lines". In: *Nuclear Instruments and Methods in Physics Research Section A: Accelerators, Spectrometers, Detectors and Associated Equipment* 566.1 (2006), pp. 14–17. ISSN: 0168-9002. DOI: 10.1016/j.nima.2006.05.156.

[61] H. Jansen and P. Schütze. "Feasibility of track-based multiple scattering tomography". In: *Applied Physics Letters* 112.14 (2018), p. 144101. DOI: 10.1063/1.5005503.

[62] C.-A. Collins-Fekete et al. "Developing a phenomenological model of the proton trajectory within a heterogeneous medium required for proton imaging". In: *Physics in Medicine and Biology* 60.13 (2015), pp. 5071–5082. DOI: 10.1088/0031-9155/60/13/5071.

[63] D. C. Williams. "The most likely path of an energetic charged particle through a uniform medium". In: *Physics in Medicine and Biology* 49.13 (2004), pp. 2899–2911. DOI: 10.1088/0031-9155/49/13/010.

[64] T. Li et al. "Reconstruction for proton computed tomography by tracing proton trajectories: A Monte Carlo study". In: *Medical Physics* 33.3 (Feb. 2006), pp. 699–706. DOI: 10.1118/1.2171507.

[65] C.-A. Collins-Fekete et al. "A theoretical framework to predict the most likely ion path in particle imaging". In: *Physics in Medicine & Biology* 62.5 (Feb. 2017), pp. 1777–1790. DOI: 10.1088/1361-6560/aa58ce.

[66] C.-A. Collins-Fekete et al. "Extension of the Fermi–Eyges most-likely path in heterogeneous medium with prior knowledge information". In: *Physics in Medicine & Biology* 62.24 (2017), pp. 9207–9219. DOI: 10.1088/1361-6560/aa955d.

[67] A. Konstantinidis. "2.02 - Physical Parameters of Image Quality". In: *Comprehensive Biomedical Physics*. Ed. by Brahme A. Oxford: Elsevier, 2014, pp. 49–63. ISBN: 978-0-444-53633-4. DOI: 10.1016/B978-0-444-53632-7.00202-1.

[68] J. Seco et al. "Characterizing the modulation transfer function (MTF) of proton/carbon radiography using Monte Carlo simulations". In: *Medical Physics* 40.9 (Sept. 2013), p. 091717. DOI: 10.1118/1.4819816.

[69] D. C. Hansen et al. "Improved proton computed tomography by dual modality image reconstruction". In: *Medical Physics* 41.3 (Feb. 2014), p. 031904. DOI: 10.1118/1.4864239.

[70] L. Volz et al. "Theoretical considerations on the spatial resolution limit of single-event particle radiography". In: *Biomedical Physics & Engineering Express* 6.5 (July 2020), p. 055002. DOI: 10.1088/2057-1976/ab9c3f.

[71] C. Bopp et al. "Quantitative proton imaging from multiple physics processes: a proof of concept". In: *Physics in Medicine and Biology* 60.13 (June 2015), pp. 5325–5341. DOI: 10.1088/0031-9155/60/13/5325.

[72] C. T. Quiñones. "Proton computed tomography". PhD thesis. Institut National des Sciences Appliquées de Lyon, 2016.

[73] N. Krah et al. "Scattering proton CT". In: *Physics in Medicine & Biology* 65.22 (Nov. 2020), p. 225015. DOI: 10.1088/1361-6560/abbd18.

[74] S. Rit et al. "Filtered backprojection proton CT reconstruction along most likely paths". In: *Medical Physics* 40.3 (Feb. 2013), p. 031103. DOI: 10.1118/1.4789589.

[75] M. Stock et al. "The technological basis for adaptive ion beam therapy at MedAustron: Status and outlook". In: *Zeitschrift für Medizinische Physik* 28.3 (Aug. 2018), pp. 196–210. DOI: 10.1016/j.zemedi.2017.09.007.

[76] F. Ulrich-Pur et al. "Commissioning of low particle flux for proton beams at MedAustron". In: *Nuclear Instruments and Methods in Physics Research Section A: Accelerators, Spectrometers, Detectors and Associated Equipment* (June 2021), p. 165570. DOI: 10.1016/j.nima.2021.165570.

[77] S. Agostinelli et al. "Geant4—a simulation toolkit". In: *Nuclear Instruments and Methods in Physics Research Section A: Accelerators, Spectrometers, Detectors and Associated Equipment* 506.3 (July 2003), pp. 250–303. DOI: 10.1016/s0168-9002(03)01368-8.

[78] S. Jan et al. "GATE V6: a major enhancement of the GATE simulation platform enabling modelling of CT and radiotherapy". In: *Physics in Medicine and Biology* 56.4 (Jan. 2011), pp. 881–901. DOI: 10.1088/0031-9155/56/4/001.

[79] D. Dannheim et al. *Corryvreckan: A Modular 4D Track Reconstruction and Analysis Software for Test Beam Data*. 2020. arXiv: 2011.12730 [physics.ins-det].

[80] S. van der Walt et al. "scikit-image: image processing in Python". In: *PeerJ* 2 (June 2014), e453. DOI: 10.7717/peerj.453.

[81] B. R. Ramesh et al. "An Algorithm for Computing the Discrete Radon Transform With Some Applications". In: *TENCON '89, Fourth IEEE Region 10 International Conference: Information technologies for the 90's, E C: energy, electronics, computers, communications*. 1989.

[82] A. Andersen. "Simultaneous Algebraic Reconstruction Technique (SART): A superior implementation of the ART algorithm". In: *Ultrasonic Imaging* 6.1 (Jan. 1984), pp. 81–94. DOI: 10.1016/0161-7346(84)90008-7.

[83] P. Ramachandran and G. Varoquaux. "Mayavi: 3D Visualization of Scientific Data". In: *Computing in Science & Engineering* 13.2 (Mar. 2011), pp. 40–51. DOI: 10.1109/mcse.2011.35.

[84] M.J. French et al. "Design and results from the APV25, a deep sub-micron CMOS front-end chip for the CMS tracker". In: *Nuclear Instruments and Methods in Physics Research Section A: Accelerators, Spectrometers, Detectors and Associated Equipment* 466.2 (July 2001), pp. 359–365. DOI: 10.1016/s0168-9002(01)00589-7.

[85] M. Valentan et al. "Optimization of Strip Isolation for Silicon Sensors". In: *Physics Procedia* 37 (2012). Proceedings of the 2nd International Conference on Technology and Instrumentation in Particle Physics (TIPP 2011), pp. 891–898. ISSN: 1875-3892. DOI: 10.1016/j.phpro.2012.04.098.

[86] M. Friedl et al. "Readout and Data Processing Electronics for the Belle-II Silicon Vertex Detector". In: (2009). DOI: 10.5170/CERN-2009-006.417. URL: http://cds.cern.ch/record/1235848.

[87] F. Ulrich-Pur et al. "Imaging with protons at MedAustron". In: *Nuclear Instruments and Methods in Physics Research Section A: Accelerators, Spectrometers, Detectors and Associated Equipment* 978 (2020), p. 164407. ISSN: 0168-9002. DOI: 10.1016/j.nima.2020.164407.

[88] R. Thalmeier et al. "The Belle II SVD data readout system". In: *Nuclear Instruments and Methods in Physics Research Section A: Accelerators, Spectrometers, Detectors and Associated Equipment* 845 (Feb. 2017), pp. 633–638. DOI: 10.1016/j.nima.2016.05.104.

[89] C. Irmler et al. "Run and slow control system of the Belle II silicon vertex detector". In: *Nuclear Instruments and Methods in Physics Research Section A: Accelerators, Spectrometers, Detectors and Associated Equipment* 958 (Apr. 2020), p. 162706. DOI: 10.1016/j.nima.2019.162706.

[90] P. Baesso et al. "The AIDA-2020 TLU: a flexible trigger logic unit for test beam facilities". In: *Journal of Instrumentation* 14.09 (Sept. 2019), P09019–P09019. DOI: 10.1088/1748-0221/14/09/p09019.

[91] A. Burker et al. "Imaging with Ion Beams at MedAustron". In: *Nuclear Instruments and Methods in Physics Research Section A: Accelerators, Spectrometers, Detectors and Associated Equipment* 958 (Apr. 2020), p. 162246. DOI: 10.1016/j.nima.2019.05.087.

[92] J. Kröger et al. *User Manual for the Corryvreckan Test Beam Data Reconstruction Framework, Version 1.0*. 2019. arXiv: 1912.00856 [physics.ins-det].

[93] W. Kiesenhofer et al. *BEAM TEST RESULTS FOR FINE PITCHED MULTIGEOMETRY SILICON STRIP DETECTORS*. 2010, pp. 858–863. DOI: 10.1142/9789814307529_0137.

[94] R. Frühwirth et al. "Analysis of beam test data by global optimization methods". In: *Nuclear Instruments and Methods in Physics Research Section A: Accelerators, Spectrometers, Detectors and Associated Equipment* 732 (2013). Vienna Conference on Instrumentation 2013, pp. 79–82. ISSN: 0168-9002. DOI: 10.1016/j.nima.2013.05.038.

[95] T. Plautz et al. "200 MeV Proton Radiography Studies With a Hand Phantom Using a Prototype Proton CT Scanner". In: *IEEE Transactions on Medical Imaging* 33.4 (Apr. 2014), pp. 875–881. DOI: 10.1109/tmi.2013.2297278.

[96] F. Ulrich-Pur. Personal communication. Apr. 2021.

[97] B. Erdelyi. "A comprehensive study of the most likely path formalism for proton-computed tomography". In: *Physics in Medicine & Biology* 54.20 (Sept. 2009), pp. 6095–6122. DOI: 10.1088/0031-9155/54/20/005.

[98] N. Krah et al. "Polynomial modelling of proton trajectories in homogeneous media for fast most likely path estimation and trajectory simulation". In: *Physics in Medicine & Biology* 64.19 (Oct. 2019), p. 195014. DOI: 10.1088/1361-6560/ab3d0b.

[99] L. Volz et al. "Improving single-event proton CT by removing nuclear interaction events within the energy/range detector". In: *Physics in Medicine & Biology* 64.15 (Aug. 2019), 15NT01. DOI: 10.1088/1361-6560/ab2671.

[100] F. Khellaf et al. "Effects of transverse heterogeneities on the most likely path of protons". In: *Physics in Medicine & Biology* 64.6 (2019), p. 065003. DOI: 10.1088/1361-6560/ab02a8.

[101] M. D. Brooke and S. N. Penfold. "An inhomogeneous most likely path formalism for proton computed tomography". In: *Physica Medica: European Journal of Medical Physics* 70.1120-1797 (2020), pp. 184–195. DOI: 10.1016/j.ejmp.2020.01.025.

[102] C. Civinini et al. "Development of a Proton Computed Tomography system for pre-clinical tests". In: *2012 IEEE Nuclear Science Symposium and Medical Imaging Conference Record (NSS/MIC)*. 2012, pp. 1279–1283. DOI: 10.1109/NSSMIC.2012.6551313.

[103] U. Schneider et al. "Technical Note: Spatial resolution of proton tomography: Impact of air gap between patient and detector". In: *Medical Physics* 39.2 (2012), pp. 798–800. DOI: 10.1118/1.3676739.

[104] C. Bopp et al. "The impact of tracking system properties on the most likely path estimation in proton CT". In: *Physics in Medicine and Biology* 59.23 (2014), N197–N210. DOI: 10.1088/0031-9155/59/23/n197.

[105] S. Radonic et al. "Investigation of the effect of air gap size on the spatial resolution in proton- and helium radio- and tomography". In: *Zeitschrift für Medizinische Physik* (2020). ISSN: 0939-3889. DOI: 10.1016/j.zemedi.2020.03.002.

[106] A. Burker et al. *Single particle tracking uncertainties in ion imaging*. 2021. arXiv: 2008.08422 [physics.med-ph].

[107] G. Poludniowski et al. "Proton radiography and tomography with application to proton therapy". In: *The British Journal of Radiology* 88.1053 (2015). PMID: 26043157, p. 20150134. DOI: 10.1259/bjr.20150134.

[108] C. Civinini et al. "Proton Computed Tomography: iterative image reconstruction and dose evaluation". In: *Journal of Instrumentation* 12.01 (Jan. 2017), pp. C01034–C01034. DOI: 10.1088/1748-0221/12/01/c01034.

[109] T. Gehrke et al. "Theoretical and experimental comparison of proton and helium-beam radiography using silicon pixel detectors". In: *Physics in Medicine & Biology* 63.3 (2018), p. 035037. DOI: 10.1088/1361-6560/aaa60f.

[110] I. Rubinskiy. *EUTelescope. Offline track reconstruction and DUT analysis software*. Tech. rep. EUDET-Memo-2010-12. 2010.

[111] H. Jansen et al. "Performance of the EUDET-type beam telescopes". In: *EPJ Techniques and Instrumentation* 3.1 (Oct. 2016). DOI: 10.1140/epjti/s40485-016-0033-2.

[112] *Geant4 – Physics Reference Manual*. Version 10.5. Geant4 Collaboration. 2019.

[113] R. P. Johnson et al. "A Fast Experimental Scanner for Proton CT: Technical Performance and First Experience With Phantom Scans". In: *IEEE Transactions on Nuclear Science* 63.1 (Feb. 2016), pp. 52–60. DOI: 10.1109/tns.2015.2491918.

[114] C.-A. Collins-Fekete et al. "A maximum likelihood method for high resolution proton radiography/proton CT". In: *Physics in Medicine and Biology* 61.23 (Nov. 2016), pp. 8232–8248. DOI: 10.1088/0031-9155/61/23/8232.